

AD-A119 946

PHOTOMETRICS INC WOBURN MA

F/8 4/1

FURTHER EVALUATIONS OF INFRARED SIMULATION DATA.(U)

NOV 81 I L KOFSKY, C A TROUBRIDGE

DNA001-81-C-0003

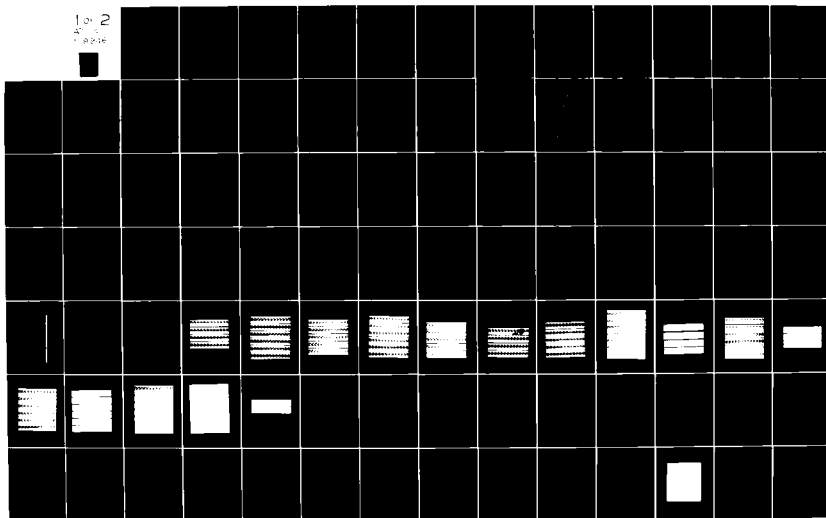
UNCLASSIFIED

PHM-07-81

DNA-TR-81-81

NL

1 of 2  
4  
- 0010



AD-E 301039

(12)

DNA TR-81-41

AD A119946

## FURTHER EVALUATIONS OF INFRARED SIMULATION DATA

PhotoMetrics, Inc.

4 Arrow Drive

Woburn, Massachusetts 01801

30 November 1981

Technical Report

CONTRACT No. DNA 001-81-C-0003

APPROVED FOR PUBLIC RELEASE;  
DISTRIBUTION UNLIMITED.

THIS WORK SPONSORED BY THE DEFENSE NUCLEAR AGENCY  
UNDER RDT&E RMSS CODE B322081466 I25AAXHX00010 H2590D.

DTIC FILE COPY

Prepared for

Director

DEFENSE NUCLEAR AGENCY

Washington, D. C. 20305

DTIC  
ELECTE  
OCT 0 6 1982

E

018

Destroy this report when it is no longer  
needed. Do not return to sender.

PLEASE NOTIFY THE DEFENSE NUCLEAR AGENCY,  
ATTN: STTI, WASHINGTON, D.C. 20305, IF  
YOUR ADDRESS IS INCORRECT, IF YOU WISH TO  
BE DELETED FROM THE DISTRIBUTION LIST, OR  
IF THE ADDRESSEE IS NO LONGER EMPLOYED BY  
YOUR ORGANIZATION.



UNCLASSIFIED

SECURITY CLASSIFICATION OF THIS PAGE (When Data Entered)

REPORT DOCUMENTATION PAGE		READ INSTRUCTIONS BEFORE COMPLETING FORM
1. REPORT NUMBER DNA-TR-81-41	2. GOVT ACCESSION NO. A3-146	3. RECIPIENT'S CATALOG NUMBER
4. TITLE (and Subtitle) FURTHER EVALUATIONS OF INFRARED SIMULATION DATA		5. TYPE OF REPORT & PERIOD COVERED Technical Report
7. AUTHOR(s) Irving L. Kofsky Christian A. Trowbridge Dennis P. Villanucci Malcolm T. Chamberlain		6. PERFORMING ORG. REPORT NUMBER PhM-07-81
9. PERFORMING ORGANIZATION NAME AND ADDRESS PhotoMetrics, Inc. 4 Arrow Drive Woburn, Massachusetts 01801		8. CONTRACT OR GRANT NUMBER(s) DNA 001-81-C-0003
11. CONTROLLING OFFICE NAME AND ADDRESS Director Defense Nuclear Agency Washington, D.C. 20305		10. PROGRAM ELEMENT, PROJECT, TASK AREA & WORK UNIT NUMBERS Subtask I25AAXHX000 10
14. MONITORING AGENCY NAME & ADDRESS (if different from Controlling Office)		12. REPORT DATE 30 November 1981
		13. NUMBER OF PAGES 128
		15. SECURITY CLASS (of this report) UNCLASSIFIED
		15a. DECLASSIFICATION DOWNGRADING SCHEDULE
16. DISTRIBUTION STATEMENT (of this Report)  Approved for public release; distribution unlimited.		
17. DISTRIBUTION STATEMENT (of the abstract entered in Block 20, if different from Report)		
18. SUPPLEMENTARY NOTES  This work was sponsored by the Defense Nuclear Agency under RDT&E RMSS Code B322081466 I25AAXHX00010 H2590D.		
19. KEY WORDS (Continue on reverse side if necessary and identify by block number) Nuclear-Effects Simulation Radiometry and Photometry Upper Atmosphere Atmospheric Irregularity Ionosphere Depletion Spaceborne Electron Accelerators Infrared Radiation Aurora		
20. ABSTRACT (Continue on reverse side if necessary and identify by block number) Infrared-optical atmospheric nuclear backgrounds simulation data from DNA/AFGL rockets EXCEDE: Spectral and PRECEDE (excita- tion of air by 3 keV electron beams) and NKC-135A aircraft (aurora and airglow radiations) are evaluated and interpreted. The output of 2.8 -3.1µm radiation from the auroral ionosphere, measured with a radiometer having footprint < 1 km square, is		

DD FORM 1 JAN 73 1473 EDITION OF 1 NOV 65 IS OBSOLETE

UNCLASSIFIED

SECURITY CLASSIFICATION OF THIS PAGE (When Data Entered)

UNCLASSIFIED

SECURITY CLASSIFICATION OF THIS PAGE (When Data Entered)

19. Key Words (continued)

Artificial Airglows

20. Abstract (continued)

correlated with particle energy input to within  $\leq 3$  sec, and the yield varies between 0.6% and 1.3%. No statistically significant correlation was found between this SWIR emission efficiency or delay and a series of auroral (and measurement) parameters, which included the fractional solar illumination of the radiating air volumes. The distributions of visible radiance from EXCEDE are found to differ from predictions of accepted models of electron transport and atmospheric excitation, both in individual photographic frames and as a function of charge-ejection altitude; principally, there is an excess of radiation from within a few rocket diameters, and the mean brightness changes much more slowly than the ambient air density between 85 and 123 km. Space- and time-dependences of the OI 6300 Å glow that resulted when ionosphere-recombining molecules were exhausted by HEAO-C's launch rocket (Eastern Test Range, 20 Sep 79) were derived from calibrated video images; its lateral growth rates indicate that the widespread F-region afterglow results principally from reactions of  $H_2$ . Some variability in the lower thermosphere's density structure is inferred from a statistical analysis of the solar photon-excited vacuum ultraviolet radiation intensities measured from the low earth orbiting satellite S3-4. Analysis of a calibrated ground photograph of the visible afterglows from PRECEDE's pulsed electron beam unexpectedly shows the energy yield to be at least comparable to that in prompt air fluorescence ( $\sim 3\%$ ).

UNCLASSIFIED

SECURITY CLASSIFICATION OF THIS PAGE (When Data Entered)

NTIS GRA&I		
DTIC TAB		
Unannounced		
Justification		
By _____		
Distribution/		
Availability Codes		
Dist	Avail and/or	
	Special	



# SUMMARY

The objective of the work reported here is to evaluate and interpret data taken from rockets and aircraft on the IR-optical radiations resulting from natural and artificial energy inputs that simulate input from atmospheric nuclear explosions. Data from the EXCEDE: Spectral and PRECEDE rockets, the 1979-1980 aurora and airglow missions of AFGL's optically-instrumented aircraft, and USAF satellite S3-4 are addressed. The field measurements, sponsored by the Defense Nuclear Agency and directed by Air Force Geophysics Laboratory, are described in earlier DNA reports (Ref's 1, 21, 22, 27, 30, and 41).

Measurements of auroral particle-associated 2.8 - 3.1 $\mu$ m enhancements with 6 millirad-field radiometers operated at aircraft altitude ( $\sim$ 12 km) show that 1) the SWIR output is correlated with column energy input to within  $\leq$  3 sec and 2) the mean energy efficiencies vary between 0.6 and 1.3% (a similar factor-2 variation, in a lower range, was observed in earlier aircraft-based measurements). No statistically significant correlation was found between SWIR yield or "lag" and auroral or measurement parameters such as fractional solar illumination of the emitting region, intensity of particle precipitation, type of auroral form, and instrument pointing direction (along or at angles up to 26° from the geomagnetic field lines). The aircraft data provide some indication of an increase in SWIR emission efficiency with energy deposition altitude.

The visible radiance distributions in air excited by EXCEDE: Spectral's 3 keV electron beam are found to differ from predictions of an independent particle transport model both within individual onboard-photographic frames (excess radiation close to the rocket) and as a function of injection altitude (anomalously narrow range of mean surface brightnesses). Spatial distributions of volume emission rate, unfolded from the isophote plots, can serve in determining the glow's excitation mechanisms -- discharge- or simple outgassing-related -- and thus in assessing the contribution of secondary electrons to the measured infrared excitation.

Low light level video image of the OI 6300 Å afterglow produced by ionosphere recombination reactions following release into the F region of H<sub>2</sub> and H<sub>2</sub>O vapor by the 20 Sep 79 HEAO-C launch rocket were converted to radiance contour plots, from which time- and space-dependences of emission intensity were derived. The lateral growth of the plasma-depletion glow suggests that it is caused principally by the more rapidly-diffusing H<sub>2</sub> molecules.

An analysis of the N<sub>2</sub> Lyman-Birge-Hopfield band intensities from the daytime thermosphere, measured by a nadir-pointing narrow-field photometer on polar-orbiting satellite S3-4, shows the data samples to have somewhat higher variance than would be expected from photon counting statistics alone. This finding indicates some variability over distances  $\geq$  25 km in density of the emitting layer (135 - 180 km) at latitudes near 70° N.

A groundbased photograph showing visible radiation persisting  $\sim$ 10's sec after excitation of the atmosphere by the 2½ keV electron pulses from PRECEDE was quantified. The time-integrated light yield was found to be comparable to or greater than the yield in prompt fluorescent radiations. The source of this long-lived radiation has not been identified.

## PREFACE

This is a report of the first year's work on Contract DNA001-81-C-0003, covering evaluation and interpretation of nuclear effects-simulating infrared-optical data taken by Air Force Geophysics laboratory under sponsorship of the Defense Nuclear Agency. The information comes from the following field experiments.

- EXCEDE: Spectral electron-injection rocket EX851.44-1  
(19 Oct 79)
- PRECEDE electron-injection rocket EX407.41-1 (17 Oct 74)
- USAF NKC-135A Aircraft 55-33120 auroral and airglow  
missions (in 1979-80).

Atmospheric radiance data from experiment CRL-726 on USAF satellite S3-4 (1978) were also considered. Preliminary assessments of the results from EXCEDE and the aircraft are reported in Ref's 1 and 22.

The work was done under the direction of J.L. Kofsky. Mrs. C.C. Rice typed the manuscript. Critical information about the field measurements was provided by E.R. Huppi and R.R. O'Neil of AFGL's Optical Physics (OPR) Branch, and the authors benefited from discussions with D.N. Anderson and R.E. Huffman of AFGL and M. Mendillo and J. Baumgardner of Boston University. The encouragement of A.T. Stair Jr of AFGL, and Capt. P. Lunn, Lt. Col. W. McKechney, and Dr. H.C. Fitz Jr of the Defense Nuclear Agency is gratefully acknowledged.



# TABLE OF CONTENTS

<u>Section</u>	<u>Page</u>
SUMMARY -----	1
PREFACE -----	3
LIST OF ILLUSTRATIONS -----	5
LIST OF TABLES -----	7
1 SPATIAL DISTRIBUTION OF THE HEAO-C DEPLETION AIRGLOW -----	9
INTRODUCTION -----	9
BACKGROUND -----	10
THEORETICAL BACKGROUND AND DATA BASE -----	14
EXCITATION OF AND RADIATION FROM O D ATOMS -----	20
DATA ACCESS PROCEDURE -----	24
LATERAL GROWTH AND TIME DEPENDENCE -----	34
2 ATMOSPHERIC SWIR STRUCTURE MEASURED FROM AIRCRAFT	
ALTITUDE -----	44
INTRODUCTION -----	44
BACKGROUND -----	45
APPROACH -----	46
ALTITUDE PROFILE DETERMINATIONS -----	48
DATA REDUCTION -----	50
DATA ANALYSIS -----	72
CORRELATION WITH AURORAL AND MEASUREMENT PARAMETERS----	77
SUMMARY AND RECOMMENDATIONS -----	86
3 DELAYED VISIBLE EMISSION EXCITED BY PRECEDE -----	89
INTRODUCTION -----	89
DATA REDUCTION -----	89
DISCUSSION -----	93
4 EXCEDE: SPECTRAL ENERGY-DEPOSITION DISTRIBUTIONS -----	95
INTRODUCTION -----	95
BACKGROUND -----	96
DATA -----	97
DISCUSSION -----	99
5 RADIANCE STRUCTURE OF THE LOWER THERMOSPHERE -----	107
BACKGROUND -----	107
DATA BASE -----	108
DATA ANALYSIS -----	111
SUMMARY -----	116
REFERENCES -----	119

# LIST OF ILLUSTRATIONS

<u>Figure</u>	<u>Page</u>
1. Zenith radiance at the aircraft near onset of the enhancement of the OI forbidden lines, HEAO-C molecule exhaust -----	12
2. Side view of the HEAO-C launch trajectory with positions of the reduced video frames and ambient species densities -----	17
3. Mercator projection of the HEAO-C launcher and NKC-135A aircraft tracks -----	18
4a-i. Contour plots of the HEAO-C 6300 Å-line afterglow radiance distribution -----	25-31
5a-d. 6300 Å local-zenith brightness along lines perpendicular to the direction of the launcher's trajectory -----	36-39
6a-c. Time variation of 6300 Å zenith brightness at 100 and 200 km from the exhaust track's center -----	40-42
7. Auroral flight data segment 14, running average of 11 0.01-sec SWIR and 3914 Å samples -----	51
8a-n. All-sky photograph montages for aircraft data segments 1-15-----	54-69
9. Cross-plots of SWIR and 3914 Å-band auroral radiance intensities at three solar depression angles -----	73
10. Cross-plots of SWIR chemiluminescent yield against auroral intensity, fractional solar illumination, OH fundamental/overtone ratio, Kp, and altitudes of energy deposition -----	78-79
11. Cross-plots of visually-determined SWIR emission delay against fractional auroral illumination, peak altitude of energy deposition -----	81
12. Cross-plot of instantaneous photon ratio against altitude of peak energy deposition, auroral flight segment 13 -----	84
13. Ground photograph of the persisting afterglows resulting from PRECEDE energy deposition -----	90

# LIST OF ILLUSTRATIONS (Concluded)

<u>Figure</u>		<u>Page</u>
14.	Peak radiance and radiance integrated over area in the PRECEDE afterglow -----	92
15.	3800 - 4600 Å (FWHM) EXCEDE: Spectral glow radiance distributions at downleg altitudes 98 and 85 km -----	98
16.	3800 - 4600 Å EXCEDE: Spectral radiances along the injected electron beam's axis projected to the onboard camera -----	100
17.	Model secondary electron flux spectra and cross-sections---	102
18.	Excitation cross-sections of N <sub>2</sub> and flux distributions of thermal electrons at temperatures 0.87 - 17.5 eV -----	103
19.	Number of 1550 Å photometer counts per 0.01-sec sampling interval in a daytime section of satellite S3-4's nadir radiance measurements -----	110

# LIST OF TABLES

<u>Tables</u>	<u>Page</u>
1. All-sky video camera specifications -----	11
2. MSIS II model atmosphere for HEAO-C launch -----	14
3. Times of image radiance contour plots -----	
4. Auroral and observation parameters during SWIR enhancements -----	
5. Fractional illumination of the altitude profiles of energy deposition -----	71
6. Chemiluminous yields and apparent SWIR delays -----	76
7. Correlation of SWIR delay with auroral and measurement parameters -----	82
8. Characteristics of "corona" and beam-plasma discharge -----	105
9. High and low-pass filtering of the S3-4 VUV data -----	114
10. Results of t-test of the VUV data -----	115
11. Chi-square test of VUV data -----	117

## SECTION 1

### SPATIAL DISTRIBUTION OF THE HEAO-C DEPLETION AIRGLOW

#### INTRODUCTION

PhotoMetrics, Inc., working under AFGL direction, made a series of measurements from AFGL/DNA NKC-135A aircraft 55-3120 on the airglows that resulted from explosive release of  $H_2$  and  $H_2O$  vapor into the F region by the Atlas-Centaur rocket that launched NASA's High Energy Astrophysical Observatory-C satellite in the early morning of 20 September 1979. A preliminary report of our results along with an outline of the ionosphere-diagnostics program is presented in Ref 1, and data from other participating groups are reported in Ref 2. The spatial distribution of radiance in the  $OI$  6300 Å (forbidden red) line, which we recorded with a low light level all-sky video camera, is an observable of particular usefulness in verifying theoretical models of the plasma density depletions that are produced by such injections of reactive molecules, several more of which are to be performed in the near future. In this Section, we reduce these calibrated images to "maps" of this recombination radiation and derive glow growth parameters from these plots, for the purpose of validating and determining input parameters for computer calculations of ionosphere modification phenomenology.

No evidence of irregularities in electron density of spatial scales that would cause phase and amplitude scintillation in UHF-VHF satellite communication signals has been derived from the optical and electromagnetic wave propagation data on the HEAO-C ionospheric "hole," which is a factor-~5-depletion region surrounding the launcher's ~2000 km long trajectory. Theory (Ref 3) indicates that fluid instabilities will develop when the energy source perpendicular to the ion-confining geomagnetic field (neutral wind for gradient-drift, ionospheric currents for

current-convective, and gravity for gravitational Rayleigh-Taylor instability) is sufficient to overcome the quenching effect of free-electron recombination by the polyatomic ions that result from release of reactive molecules. In consequence the Air Force Geophysics Laboratory will shortly attempt to produce artificial equatorial spread-F irregularity with two explosive releases of  $H_2O$  and  $CO_2$  vapor from Natal (the Brazil Ionospheric Modification Experiments, currently planned for September 1982). Additionally, during the Spacelab 2 mission (Fall 1984) Shuttle Orbiter is scheduled to inject reactive gases over five ionospheric-observation sites, by firing its Orbital Maneuvering System engines. Reaction-rate and atmosphere-dynamics parameters are needed for predictive models of these ionosphere modifications.

#### BACKGROUND

For orientation, we review our optical data and the other experiment information on the transport of plasma-recombining molecules from HEAO-C's launch rocket.

The aircraft flew parallel to and approximately 40 km N of the "midpoint" of the rocket exhaust track in the first  $\sim \frac{1}{2}$  hr after launch (see Fig 33 of Ref 1). Its monochromatic video camera (Table 1 and Ref 4) recorded moderately high signal/noise 6300 Å images from  $\sim \frac{1}{2}$  min after initiation of second-stage fuel burn (at 212 km altitude) until at least one hr after the vapor had been injected. The red-line afterglow expanded to fill the all-sky field (practically speaking,  $\sim 1000$  km horizontally in each direction), developing a shallow minimum roughly centered on the trajectory. A  $2^\circ$  circular field wavelength-cycling photometer pointed to the zenith measured maximum enhancements of 8.5 kilorayleighs in the OI forbidden red line  $90 \pm 10$  sec after the rocket passed  $\sim 35$  km from its field of view and 0.95 kR in the green (5577 Å) line  $50 \pm 12$  sec after; both radiance pulses had duration halfwidths near 2 min. Fig 1 shows the radiances in the aircraft's zenith at the onset of the recombination glows; the data for the full flight are in Fig 37 of Ref 1, at a more compressed time scale.

Table 1. All-sky video camera specifications

Type:	Cohu (San Diego, CA) 2856B ISIT, 16 mm target (RCA 4849 A).
Dynamic Range:	Automatic gain control in camera, automatic brightness control in intensifier combine to factor $10^6$ .
Spectral Response:	S-20 photocathode preceded by narrow band interference filter at telecentric stop of the camera lens. Center sensitivity wavelength 6300 Å, bandwidth $\sim 20$ Å.
Sensitivity:	0.1 kR-sec with 5 lp/mm at photocathode (see Ref 4).
Optics:	F/1.5 (T1.8 at 6300 Å) Pacific Optical fish-eye objective, 3.45 mm fl, FOV 165°. Relay lens as in Ref 4.
Geometric Distortion:	Maximum 4% within a circle whose diameter does not exceed the picture height.
Recording:	Standard analog video, 1 inch tape.

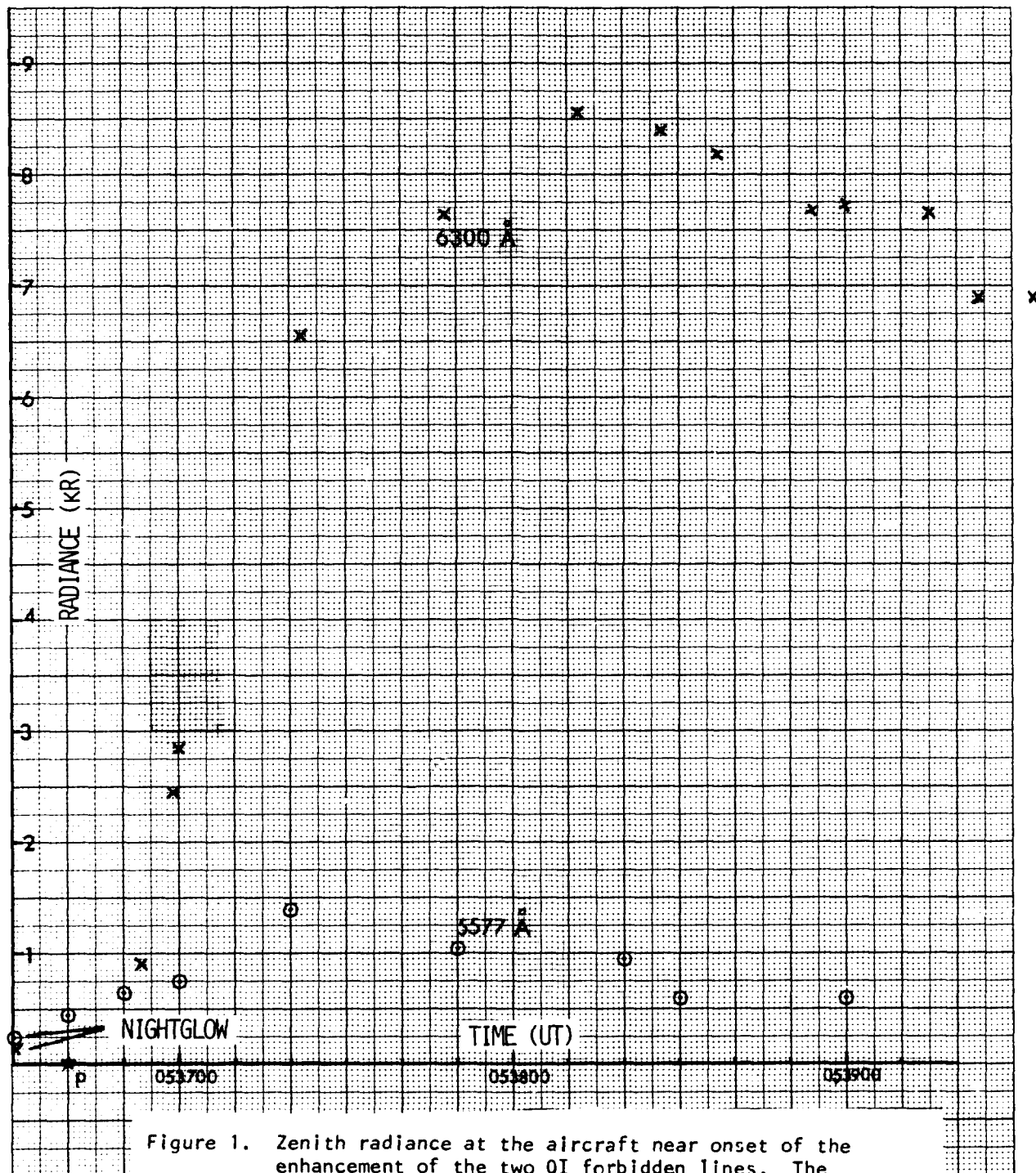


Figure 1. Zenith radiance at the aircraft near onset of the enhancement of the two OI forbidden lines. The rocket passed about 30 km S of the photometer's field of view at the time marked p.



The aircraft photometer and near-infrared radiometer data so far show convincing evidence of sky background enhancement in only one other wavelength band, 2.832 - 3.14  $\mu\text{m}$  (FWHM). Several other airglow features monitored --  $\text{O}_2^1\Delta$  (infrared atmospheric fundamental),  $\text{NO} + \text{O}$  continuum,  $\text{OH}$   $\Delta v = 4$  and 5 sequences,  $\text{NaI}$  resonance doublet,  $\text{N}^2\text{D} - ^4\text{S}$  F-region doublet, and in particular the (10,4) hydroxyl band near 6700  $\text{\AA}$  reported (Ref 5) as excited by the "Lagopedo" (1977) release of water vapor into the ionosphere -- were not detectably increased (as far as can be determined from the present stage of data reduction). We interpreted the  $\sim 20$  kR 2.832-3.14  $\mu\text{m}$  increase (Ref 1), which was measured by a cryocooled radiometer with 0.4° field pointed 13° forward of the aircraft's zenith, as  $\Delta v = 1$  hydroxyl vibrational emission following electronic excitation and radiative relaxation of the  $\text{OH A}(^2\Sigma^+)$  state. This initial electronic excitation presumably results from the  $\text{e} + \text{H}_2\text{O}^+$  dissociative recombination reaction. As explained in Ref 1, it would provide a selective population of the upper states of the infrared (1,0) and (2,1) vibrational bands, to which the radiometer is sensitive. Our interpretation of the emission process can be verified by spectrophotometry of the A-X bands of OH, some of which lie at wavelengths just above the atmospheric ozone cutoff near 3100  $\text{\AA}$ , following injection of  $\text{H}_2\text{O}$  vapor or  $\text{H}_2$  into the F region. (This infrared-backgrounds issue is not further pursued in this Report.)

The most extensive measurements of the HEAO-C plasma depletion were made with a network of polarimeters, which monitor by Faraday rotation of radiowave polarization the changes in total free electron column-content along lines of sight to beacons on geosynchronous satellites. These projections of the volume electron densities to spatially-dispersed stations compose low resolution, essentially one-dimensional "images" of a limited section of the ionosphere depletion region. Similarly, polarimetry data taken using earth-orbiting satellite beacons provide 1-D scans of total electron content over the limited time span of the satellite's traverse. (Additionally, some plasma depletions near the F-region peak were measured directly by a distant

incoherent-scatter radar.) The monochromatic all-sky camera views of the airglow from below the deposition track represent, on the other hand, high spatial resolution, 2-D projections of the column concentrations of  $O^1D$ , which are a by-product and indicator of the removal of ionospheric plasma by the rocket engine exhaust.

#### THEORETICAL BACKGROUND AND DATA BASE

Numerical models for simulating the propagation of high-density chemically-reactive gases injected into the ionosphere are presented in Ref's 6,7 and 8, and 9. These (other than that of Ref 9, which was found to fit the data poorly) have not yet been applied to HEAO-C's initial conditions, which result from what is in effect a continuous explosion along the boost vehicle's trajectory. In later stages of the fuel burn the net exhaust velocity of the thruster gas may be in the rocket's direction; and some major (but unknown) fraction of the ejected  $H_2O$  vapor condenses into droplets. Some  $3 \times 10^{23}$  molecules were injected per meter of flight path.

This amount of material makes the foreign species densities comparable to natural ambient in the  $\sim 10^5$  km radius volume to which the fast-moving gases expand before they collisionally thermalize. (Refer to Figure 2 for atmosphere densities at trajectory altitudes.) A transition to diffusive expansion, which is more readily described by transport models, takes place when their number density falls significantly below ambient. Ref 10 gives the theory of this latter growth phase for the simplified conditions of negligible depletion of the atmospheric reactants and diffusion lengths less than the neutral-particle scale height, and applies it to radiometric photographs of TMA/A80 vertical trail releases; this reference provides an introduction to both the physics of chemically-reacting, cylindrically-symmetric contaminant clouds and the data access and reduction procedures applied here.

The  $H_2$  and  $H_2O$  molecules destroy both themselves and the iono-

sphere's (predominant)  $O^+$  ions. ( $H_2$  is also removed in a neutral-particle reaction, with  $O$  atoms (Ref 11).) At the same time the  $O^+$  concentrations in the "hole" are partially replenished by diffusion, and the plasma density distribution in the affected volume is modified by F-region ion and neutral winds (Ref's 8,12).

Fig 36 of Ref 1 presents sample all-sky images of the 6300 Å-line glow that results from electron recombination of oxygen-containing molecular ions. The geometry of these video photographs is illustrated in the side and plan views of the rocket and aircraft trajectories, Figures 2 and 3. The images are as usual two-dimensional projections to the camera lens of volume emission rates in columns extending through the three-dimensional radiating cloud. (The glow volume is definitely optically thin to its own radiation.) Scene radiances tend to increase with zenith angle from the aircraft because of the increasing sight path through the glow.

Simple van Rhijn corrections of the type used on natural air-glow (Ref 13) can be applied to assess the vertical-column radiances, such as would be measured from, say, a distant satellite in the glow's zenith. The release trajectory is tilted upward rather than being concentric with the earth's surface, and is such that the the amount of material being exhausted per horizontal km is decreasing along the trajectory; the cosines of the track's inclination angle are shown in Fig 2. Zenith (or nadir) radiances can be found directly by multiplying the projected radiances by the cosine of the zenith angle, which is the angle between the line to the camera and the local vertical; when radiances from release segments at different altitudes are intercompared, the aforementioned correction for the nonuniform horizontal exhaust rate must be applied. The glow radiances can thus be straightforwardly converted to plan view values from the equi-brightness plots presented here, or alternatively, volume emission rates calculated from the ionosphere modification models can be projected to the camera to simulate the actual measurement conditions.

(The camera was diverted for  $\sim 10$  -sec periods to image the glow in 5577 Å radiation at early times, and to image at 6300 Å with a  $23^\circ \times 17^\circ$  field at later times. These brief data segments are not considered here.)

Horizontal-transport information has been extracted from the video images for the four representative exhaust altitudes 257, 334, 400, and 450 km. These positions along the launcher's track are labeled I-IV on Figures 2 and 3. We have not addressed lower trajectory altitudes because the photogrammetric accuracy of the all-sky camera is decreasing rapidly near the edge of the camera's field of view; as Fig 2 shows, the start of rocket-burn at 212 km altitude lies somewhat outside the  $\sim 80^\circ$  circular field. (Furthermore the 6300 Å radiation intensity at the lower altitudes tends to be weak because  $O^1D$  is both strongly collisionally quenched and unfavored in the depletion reactions, as we show in the following subsection.) Near exhaust cutoff the transport geometry loses its "cylindrical symmetry," complicating model calculations. The highest point we considered, 450 km, is 950 km horizontally from but only 8/10 of an atmospheric density scale height below the end of the rocket fuel burn at 501 km altitude. The actual mean altitudes to which the transport results refer are higher than those of the exhaust, as there is net upward transport of reactive gas toward lower ambient densities.

The four ejection altitudes span an atmospheric density range of a factor 31 (MSIS 11 atmospheric model, Ref 14) and an ionospheric [ $O^+$ ] range of a factor 25 (Millstone Hill incoherent-scatter radar data, Ref 2).  $N_2$ , total particle (principally,  $O$  atoms), and  $O^+$  densities are shown at each data-reduction location, and scale heights of  $N_2$  and  $H_2O$  (which figure in the diffusion theory) are also indicated on Fig 2. We calculated the atmospheric profile at the time and latitude of rocket launch using MSIS 11; results are listed in Table 2. The  $N_2$  molecule concentrations were used in calculating the probability of 6300 Å radiative relaxation of the  $O^1D$  atoms at each  $H_2-H_2O$  exhaust altitude; since the centroid of the glow is above these altitudes, there is actually somewhat less collisional quenching than the  $[N_2]$ 's indicate.

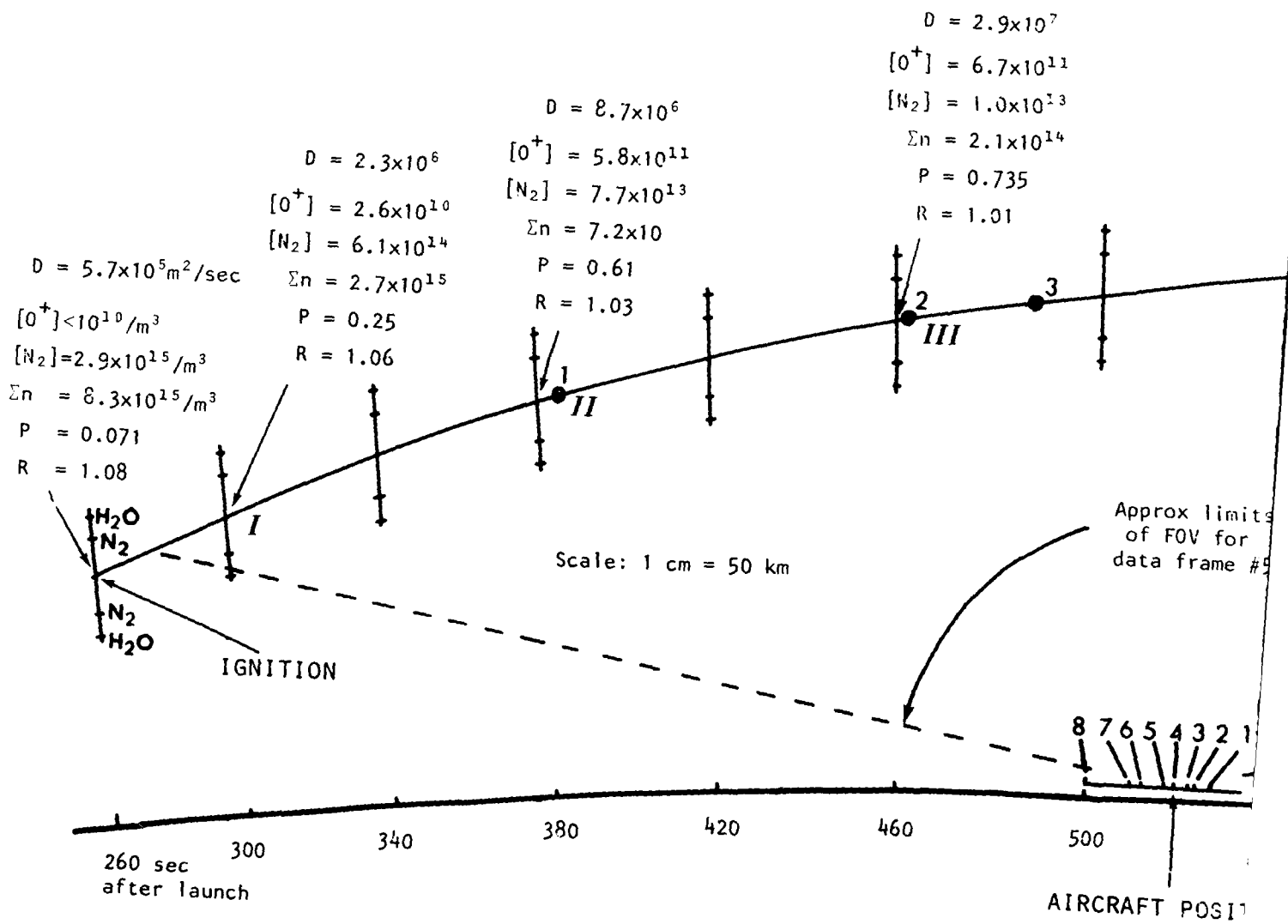
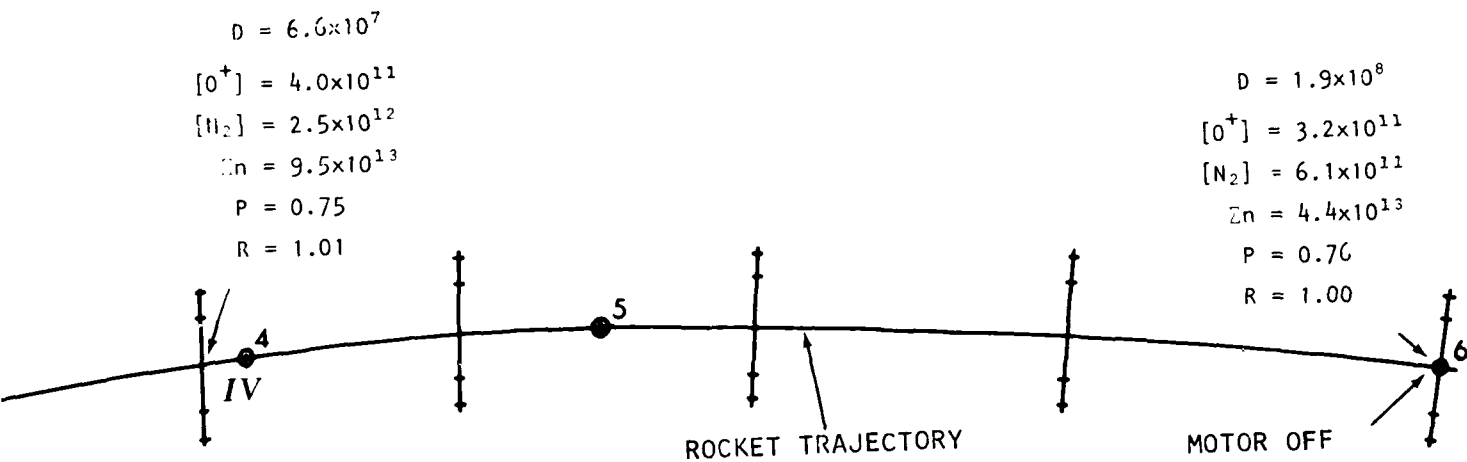
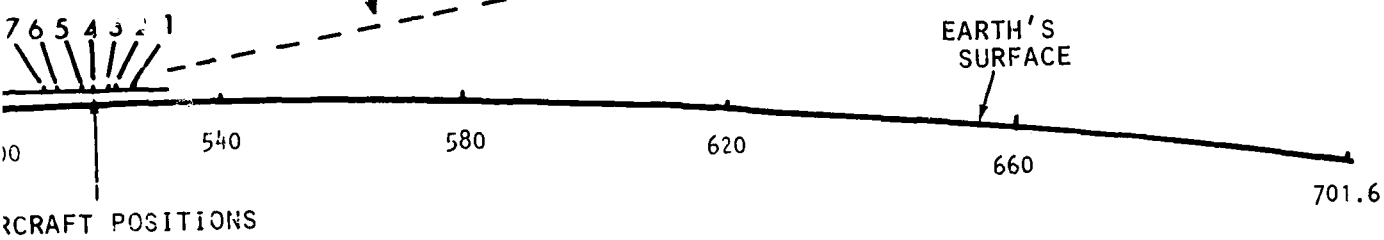


Figure 2. Side view of HEAO-C launch trajectory (looking N) during the  $H_2 - H_2O$  exhaust. The plot gives  $H_2$  diffusion coefficients (labeled  $D$ );  $O^+$ ,  $N_2$ , and total number densities, and scale heights of  $N_2$  and  $H_2O$ ; probability of 6300 Å radiation from  $O^+$  atoms ( $P$ ); and the ratio of horizontal to along-path exhaust deposition ( $R$ ), at the four altitudes I - IV at which the lateral growth of radiation intensity was investigated. The positions of the launcher when the aircraft was at positions 1 - 6 are also indicated.



Approx limits  
of FOV for  
data frame #5



st. The plot  
ities, and  
(P); and the  
udes I - IV  
ositions of

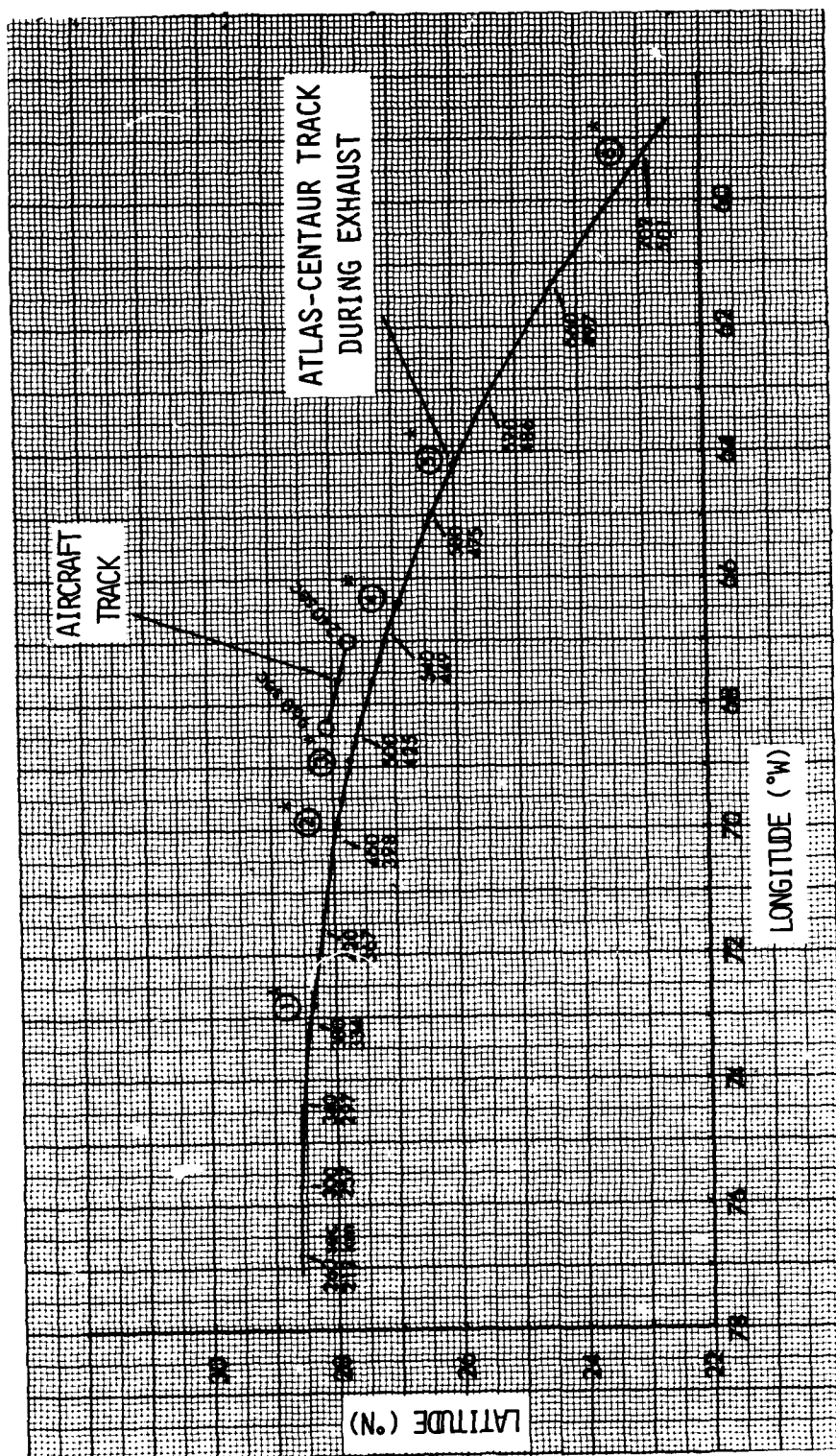


Figure 3. Mercator projection of the launcher and aircraft tracks. The positions of the rocket at the times for which the video frames are reduced are indicated with asterisks.

# MSIS MODEL ATMOSPHERE

YDAY = 79263

LST = 1.20

SEC = 20400.

GLAT = 28.00

GLONG = -67.00

F107A = 175.

F107 = 216.

AP = 6.

Table 2. MSIS II model atmosphere for HEAO-C launch.  
(Refer to Fig 2 for 0<sup>+</sup> concentrations)

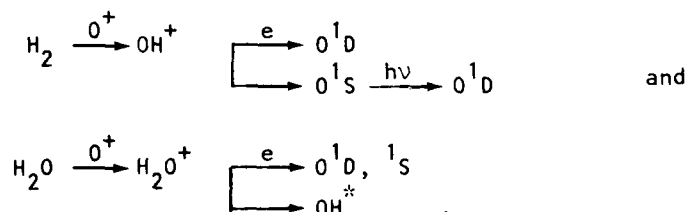
ALT	T-EX	TEMP	N2	O2	0	AR	HE	H	TOTAL	KG-M-3
200.0	1024.8	971.0	4.063E+15	2.333E+14	6.368E+15	3.465E+12	9.840E+12	4.210E+04	1.068E+16	3.704E-16
210.0	1024.8	985.1	2.917E+15	1.601E+14	5.224E+15	2.177E+12	9.346E+12	4.124E+04	8.313E+15	2.830E-16
220.0	1024.8	995.5	2.113E+15	1.109E+14	4.316E+15	1.377E+12	8.895E+12	4.055E+04	6.551E+15	2.189E-16
230.0	1024.8	1003.1	1.541E+15	7.738E+13	3.586E+15	8.796E+11	8.480E+12	3.992E+04	5.213E+15	1.711E-16
240.0	1024.8	1008.8	1.129E+15	5.428E+13	2.991E+15	5.655E+11	8.095E+12	3.936E+04	4.183E+15	1.349E-16
250.0	1024.8	1012.9	8.306E+14	3.824E+13	2.502E+15	3.454E+11	7.734E+12	3.884E+04	3.379E+15	1.072E-16
260.0	1024.8	1016.0	6.129E+14	2.703E+13	2.099E+15	2.370E+11	7.398E+12	3.835E+04	2.746E+15	8.572E-17
270.0	1024.8	1018.3	4.534E+14	1.916E+13	1.763E+15	1.542E+11	7.080E+12	3.790E+04	2.243E+15	6.898E-17
280.0	1024.8	1019.9	3.361E+14	1.361E+13	1.484E+15	1.006E+11	6.779E+12	3.746E+04	1.841E+15	5.581E-17
290.0	1024.8	1021.2	2.496E+14	9.488E+12	1.251E+15	6.580E+10	6.493E+12	3.704E+04	1.517E+15	4.538E-17
300.0	1024.8	1022.1	1.856E+14	6.907E+12	1.055E+15	4.312E+10	6.222E+12	3.663E+04	1.254E+15	3.704E-17
310.0	1024.8	1022.8	1.382E+14	4.932E+12	8.910E+14	2.831E+10	5.946E+12	3.623E+04	1.040E+15	3.039E-17
320.0	1024.8	1023.3	1.031E+14	3.527E+12	7.530E+14	1.861E+10	5.717E+12	3.584E+04	8.654E+14	2.502E-17
330.0	1024.8	1023.7	7.692E+13	2.525E+12	6.369E+14	1.226E+10	5.483E+12	3.546E+04	7.219E+14	2.066E-17
340.0	1024.8	1023.9	5.748E+13	1.810E+12	5.391E+14	8.087E+09	5.258E+12	3.509E+04	6.037E+14	1.712E-17
350.0	1024.8	1024.1	4.299E+13	1.299E+12	4.565E+14	5.341E+09	5.044E+12	3.473E+04	5.059E+14	1.423E-17
360.0	1024.8	1024.3	3.219E+13	9.330E+11	3.869E+14	3.533E+09	4.840E+12	3.437E+04	4.249E+14	1.185E-17
370.0	1024.8	1024.4	2.412E+13	6.710E+11	3.280E+14	2.340E+09	4.644E+12	3.401E+04	3.575E+14	9.901E-18
380.0	1024.8	1024.5	1.809E+13	4.831E+11	2.783E+14	1.552E+09	4.457E+12	3.366E+04	3.014E+14	8.288E-18
390.0	1024.8	1024.6	1.359E+13	3.481E+11	2.342E+14	1.030E+09	4.278E+12	3.332E+04	2.545E+14	6.953E-18
400.0	1024.8	1024.6	1.021E+13	2.511E+11	2.006E+14	6.850E+08	4.107E+12	3.298E+04	2.152E+14	5.844E-18
410.0	1024.8	1024.7	7.677E+12	1.813E+11	1.705E+14	4.559E+08	3.943E+12	3.264E+04	1.823E+14	4.920E-18
420.0	1024.8	1024.7	5.779E+12	1.311E+11	1.449E+14	3.039E+08	3.786E+12	3.231E+04	1.546E+14	4.150E-18
430.0	1024.8	1024.7	4.354E+12	9.483E+10	1.233E+14	2.028E+08	3.636E+12	3.199E+04	1.314E+14	3.505E-18
440.0	1024.8	1024.7	3.283E+12	6.868E+10	1.049E+14	1.355E+08	3.492E+12	3.167E+04	1.118E+14	2.965E-18
450.0	1024.8	1024.7	2.477E+12	4.978E+10	8.930E+13	9.060E+07	3.355E+12	3.135E+04	9.522E+13	2.512E-18
460.0	1024.8	1024.7	1.871E+12	3.612E+10	7.607E+13	6.067E+07	3.223E+12	3.104E+04	8.123E+13	2.131E-18
470.0	1024.8	1024.7	1.414E+12	2.623E+10	6.483E+13	4.068E+07	3.096E+12	3.073E+04	6.939E+13	1.809E-18
480.0	1024.8	1024.7	1.070E+12	1.907E+10	5.527E+13	2.731E+07	2.975E+12	3.042E+04	5.936E+13	1.539E-18
490.0	1024.8	1024.8	8.101E+11	1.388E+10	4.715E+13	1.835E+07	2.859E+12	3.012E+04	5.084E+13	1.310E-18
500.0	1024.8	1024.8	6.138E+11	1.011E+10	4.023E+13	1.235E+07	2.748E+12	2.983E+04	4.364E+13	1.116E-18
510.0	1024.8	1024.8	4.655E+11	7.367E+09	3.435E+13	8.316E+06	2.642E+12	2.953E+04	3.750E+13	9.520E-19
520.0	1024.8	1024.8	3.533E+11	5.375E+09	2.934E+13	5.608E+06	2.540E+12	2.924E+04	3.227E+13	8.130E-19



Also shown in Fig 2 are the radial diffusion coefficients of  $H_2O$  molecules in an oxygen-atom atmosphere, as given in Ref 12 for 1000 K exospheric temperature (we derived 1025 K from MSIS). The calculated diffusion coefficients of  $H_2$  are closely 6 times those listed for  $H_2O$ . Although classical minority diffusion through a uniform atmosphere does not properly describe the transport of the injected gas (see, for example, Ref 15), and both growth while it is initially overdense (Ref 17) and depletion of the critical reactant  $O^+$  must be considered, the diffusion coefficients at least provide some orientation to the order of magnitude of the projected glow dimensions. For example at 10 min after exhaust a characteristic spread of hydrogen at 334 km ( $4 \times \text{diffusion coefficient} \times \text{time}$ )<sup>1/2</sup> would be about 200 km, which is in fact close to that calculated for thermalized  $H_2$  (see Fig 7 of Ref 8). (The cloud's halfwidth in the minority-diffusion phase can be estimated by adding in quadrature its halfwidth at the end of the self-diffusion phase and the halfwidth during the duration of minority diffusion.)

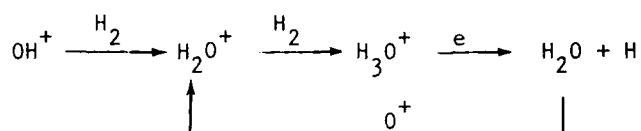
#### EXCITATION OF AND RADIATION FROM $O^1D$ ATOMS

As some fraction of the final-step reactions in the chains that remove the dominant F-region ion species  $O^+$  results in production of  $O^1D$ -state oxygen atoms, the rates of excitation are a measure of the rates of ionospheric plasma depletion (refer to the discussion in Ref 1). Schematically, considering only reactions of the injected molecules and intermediate species with ambient charged species



Considering also reactions in that volume close to the trajectory in which  $[H_2] K_h > [e] K_d$ , where the K's are rate coefficients for hydro-

generation and electron dissociative recombination of molecular ions  
( $K_h/K_d \approx 10^{-2}$ , Ref 7),



Under these conditions --  $10^{-2} [\text{H}_2] \approx [\text{e}]$  -- excitation of  $\text{O}^1\text{D}$  is not favored. We note that  $10^{23}$   $\text{H}_2$  molecules are exhausted per cm of trajectory; when these expand out to 50 km,  $10^{-2} [\text{H}_2] \approx 10^{11}/\text{m}^3$ . Comparing this figure to the initial ambient electron densities ( $= [\text{O}^+]$ ) in Fig 2, we find that radiationless plasma depletion becomes important within a few 10's km of the release trajectory, particularly at the lower altitudes and after the electron density has been reduced. The aforementioned fraction ( $\text{O}^1\text{D}$  atom excited per ion removed) thus increases away from the trajectory, and depends on the F-region's electron density profile.

The branching ratios for excitation of O's two metastable ground-configuration states in the electron dissociative recombination steps are not known. Pre-HEAO-C theoretical arguments based on photodissociation data and channel statistical weights (Ref 16) indicated that ~10-15% of these reactions excite  $\text{O}^1\text{D}$ ; however the actual radiances in the red line were considerably higher than predicted (in Ref 9). Note that the ground state of the transition that produces the OI green line emission is the upper state of the red line; but since the enhancement intensity of the green line from HEAO-C was a factor 10 less than that of the red line (in the aircraft's zenith, Fig 1), this cascade contribution is expected to be small. The partial rate coefficients, and the impact of "close-in" hydration, can be estimated by fitting parameters in the model of the ionosphere depletion to achieve agreement with the  $\text{O}^1\text{D}$  surface radiance distributions presented here.

The factor-six difference in diffusion coefficients of the two injected species might suggest that radiance traces transverse to the launcher trajectory would show a narrow peak superposed on a broader base, which would provide a more or less direct measure of the relative  $O^1D$  excitation probabilities from the two species' reaction chains. On the other hand the explosive nature of the injection, the complicating effects of the higher-than-ambient exhaust gas densities (which include the aforementioned successive hydrogen reactions leading to  $H_3O^+$ ), and the rapid reduction of  $[O^+]$  among other factors) may wash out this structure; indeed, no such distribution is found in a qualitative examination of the video images.

The metastable oxygen atoms produced in the molecular-ion dissociation reactions radiate at 6300.3 Å ( $O^1D_2 - {}^3P_2$  transition) or 6363.8 Å ( $O^1D_2 - {}^3P_1$ ), or undergo collisional quenching by  $N_2$  molecules. (Deactivation by  $O_2$  can be neglected.) Calculated transition probabilities for the two red-line radiations are 0.0069 and 0.0022  $\text{sec}^{-1}$  respectively (Ref 18), and the "aeronomic" rate coefficient for quenching of  $O^1D$  by  $N_2$  is  $3 \pm 1 \times 10^{-11} \text{ cm}^2/\text{sec}$  (Ref 19; the uncertainty is probably larger than that quoted, as the several measurements vary over a range of a factor  $> 4$ ). The probability that  $O^1D$  atoms radiate in the video camera's sensitivity band is then

$$\frac{0.0069}{0.0069 + 0.0022 + 3 \times 10^{-11} [N_2]}$$

where  $[N_2]$  is the ambient concentration of  $N_2$  molecules.

The calculated 6300 Å radiation probabilities at injection altitudes are listed in Figure 2. Note that at the lowest altitude, 212 km, only 7% of the excited atoms radiate in the camera's sensitivity band; at 257 km, our lowest data analysis altitude,  $\frac{1}{4}$  radiate; and above ~350 km, which includes the final two altitudes considered, the fraction is experimentally indistinguishable from the unquenched figure  $69/(69 + 22) = 0.76$ . Qualitatively speaking, collisional quenching of  $O^1D$  reduces the glow's radiance only at zenith angles  $> 60^\circ$  in the direction of the start of the burn, and (since the transport of injected molecules

is largely upward and horizontal rather than downward toward increasing ambient densities) has a small effect on intensities over most of the image field.

The column-concentration of  $O^1D$  atoms is given by  $(4\pi/0.0069)$  times the 6300 Å-line radiance in the direction of the column expressed in photons/sec  $cm^2$  sterad. The radiances directly indicate production rate of the end-product species at the (late) times that the fractional rates of change of  $[O^1D]$  due to both excitation-and-decay and mechanical transport are small compared to 1 in the characteristic radiation time, 100 sec. (The lifetimes of  $OH^+$  and  $H_2O^+$  turn out to be of the same order when the plasma concentration  $[e]$  is near its ambient value of  $10^5/cm^3$ .) Change of concentration of  $O^1D$  can be expressed as

$$\begin{aligned} \frac{d[O^1D]}{dt} = & - (0.0091 + 3 \times 10^{-11} [N_2]) [O^1D] \\ & + (k_1[OH^+] + k_2[H_2O^+]) [e] \\ & + \nabla \cdot \vec{v} [O^1D] , \end{aligned}$$

where  $k_1$  and  $k_2$  are the partial rate coefficients for excitation of the state in dissociative recombinations (including the effect of cascading from  $O^1S$ ) and the last term takes into account the net transport into or out of the volume considered due to divergence of  $O^1D$ 's flow velocity  $\vec{v}$  (see, for example, Ref 7). The O-atoms' characteristic diffusion length in 100 sec is of the order of 50 km  $(2 \times 10^7 m^2 sec^{-1} \times 100 sec)^{1/2}$ . Therefore the fractional change in  $O^1D$  concentration must be  $\ll 1$  over this horizontal distance if the excitation rate is to be measured directly by the radiative decay rate (that is, when excitation and decay are proceeding at the same column rate). In any case, the metastable state's long lifetime indicates that the ionosphere depletion models must take into account transport of  $O^1D$  as well as of  $H_2$ ,  $H_2O$ , and intermediate ion species in fitting to the 6300 Å radiance data distributions.

#### DATA ACCESS PROCEDURE

Contour plots of the afterglow's radiance viewed from the aircraft serve as the starting point for analysis of the 6300 Å-line emission data. Figure 4 is a set of nine equi-radiance plots spanning the time period from the first evidence of a glow in the video images (125 sec after second-stage ignition, 385 sec after launch, rocket then at 339 km) to 1060 sec after ignition (780 sec after the last trajectory altitude from which data were further reduced). Table 3 lists the times of these plots after exhaust injection at each of the four altitudes considered. Note that the aircraft reverses flight direction only before the last point in the data set; its otherwise straight track reduces the effort to correct for the changing view perspective. (Between 660 and 750 sec it executed a 25° roll to starboard, to scan the zenith-pointing radiometer transverse to the rocket's trajectory; only one image from this period is considered.)

We initially concentrate on these early times after vapor injection because of the high signal/noise in the images and the fact that virtually all of the glow remains within the all-sky (160° circular) camera field. The later-time frames also have useful information about the ionosphere depletion, particularly because the production and decay of  $O^1D$  are in near-equilibrium and the aerochemistry is not complicated by hydrogenation reactions ( $[H_2]$  having been reduced by diffusion and reactions).

The brightness maps have been radiometrically corrected as described here. "Dimensions" of the soft-edged glow and effective cross-track diffusion coefficients can be derived from cuts across the 2-D plots, with the radiances corrected to a zenith projection to remove the effect of variable pathlength in the images. (Attention is directed to the aforementioned caveats about interpreting the afterglow's width terms of species transport and ionosphere depletion.) Further descriptors of the space and time dependence of the recombination glow can of course be taken from the brightness contour plots in Fig 4.

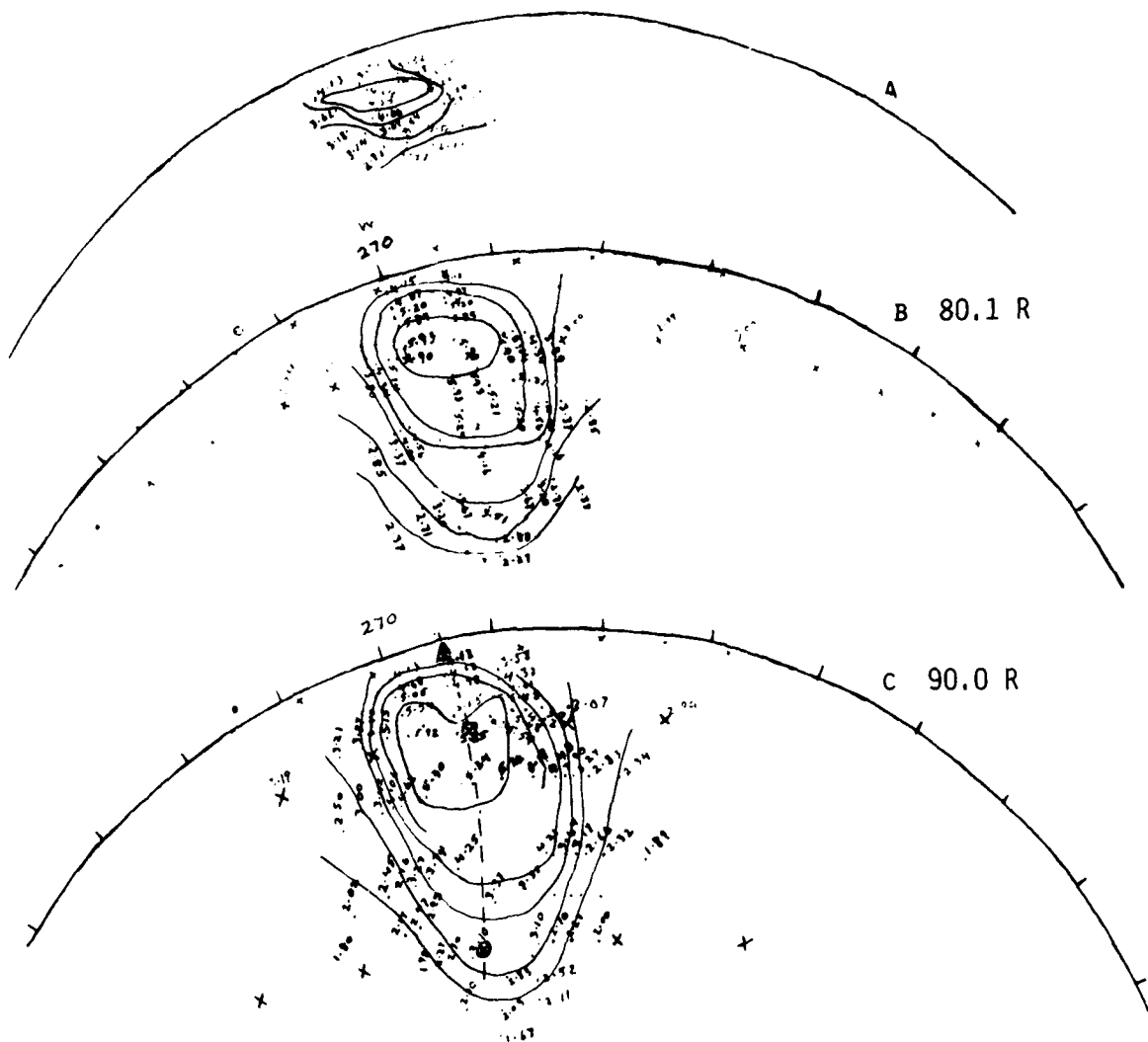
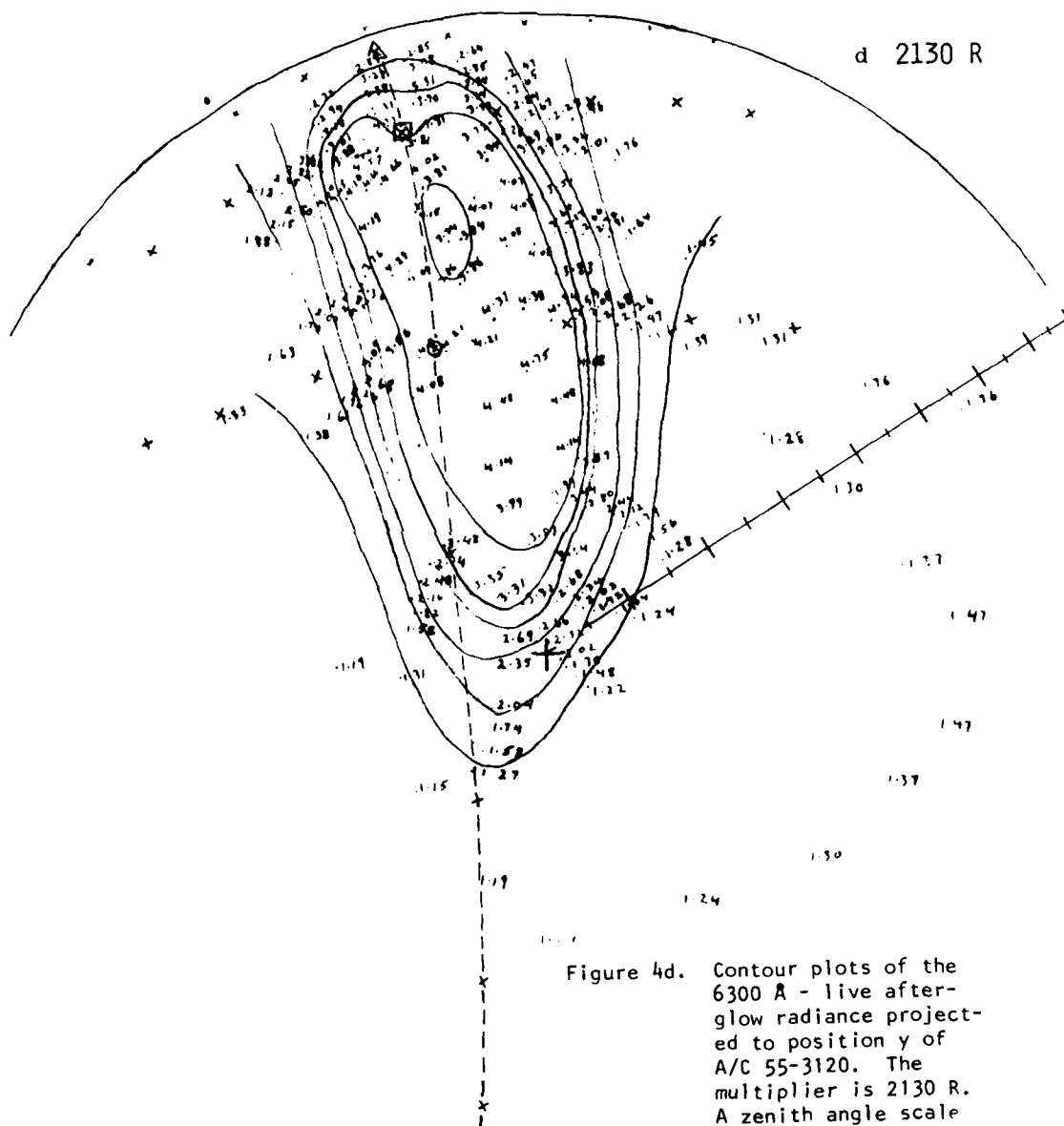


Figure 4a-c. Contour plots of the 6300 Å-line afterglow radiance resulting from HEAO-C's launcher's exhaust of  $H_2$  and  $H_2O$  into the ionosphere, projected to positions 1-3 of USAF A7C55-3120. 4a projects to 1 on Fig 2, 4b to 2, 4c to 3. The radiances are corrected for non-uniform response over the field of view (refer to text). Absolute radiances are the product of the number on the contour lines and the calibration factor given at upper right of each plot. The nightglow background of 130 - 350 R (depending on zenith angle) has not been subtracted. X's indicate the straight (horizontal) lines perpendicular to the launcher's trajectory. Refer to Fig 4d for a zenith angle scale.



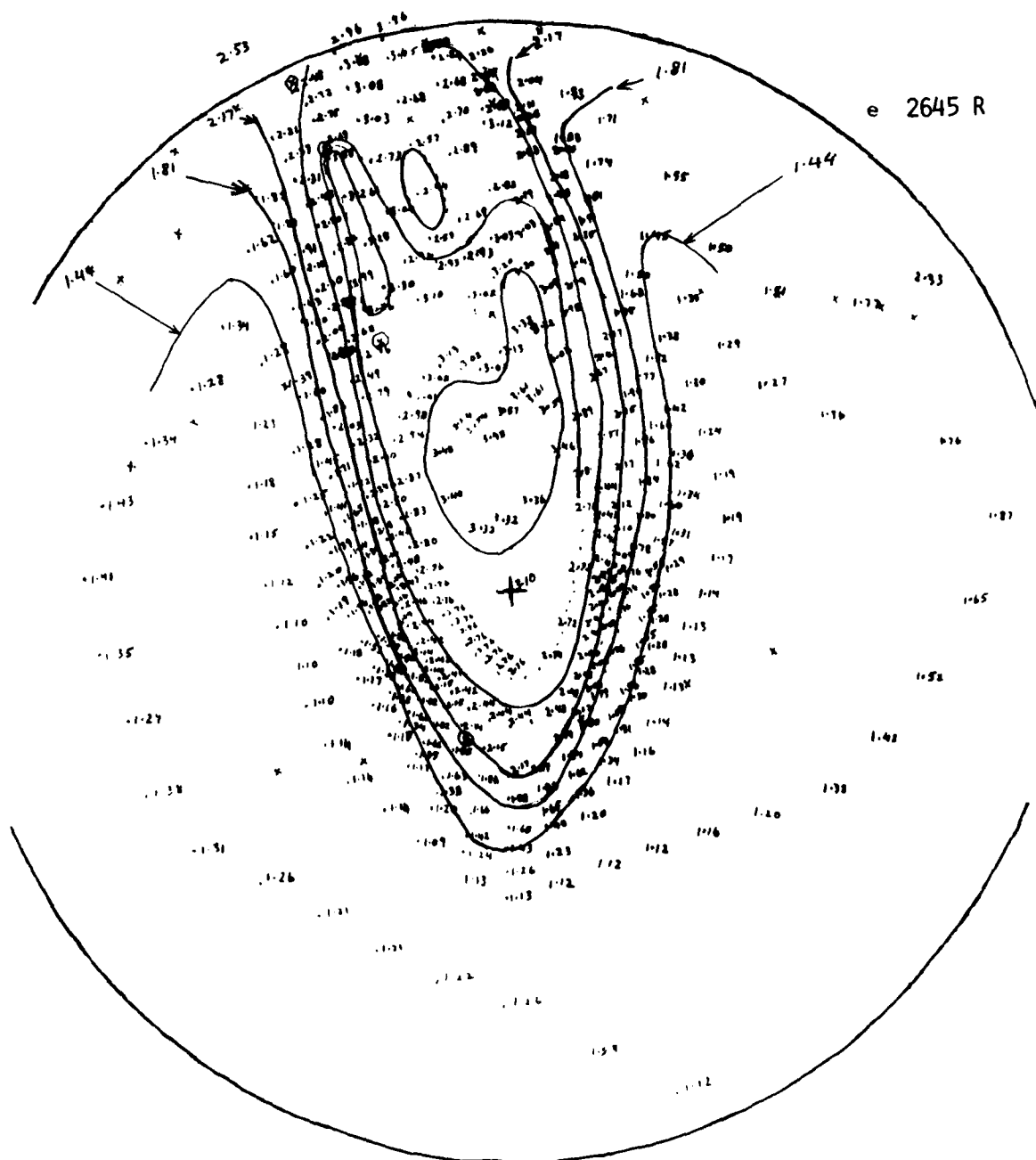


Figure 4e. Contours of the 6300 Å-line afterglow radiance projected to position 5 of A/C 55-3120. The multiplier is 2645R.



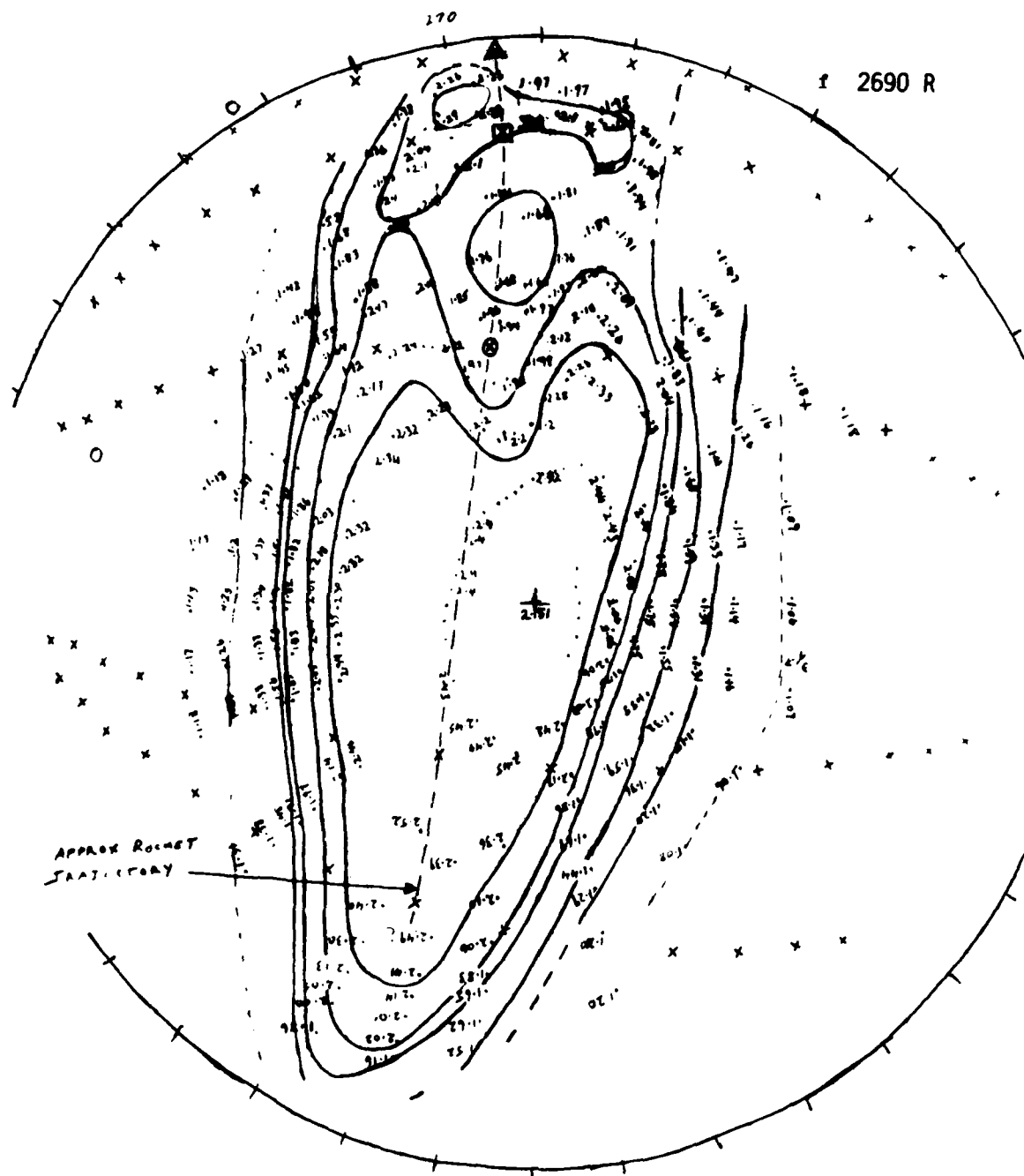


Figure 4f. Contour plots of the 6300 Å-line afterglow radiance projected to position 6 of A/C 55-3120. The multiplier is 2690 R.

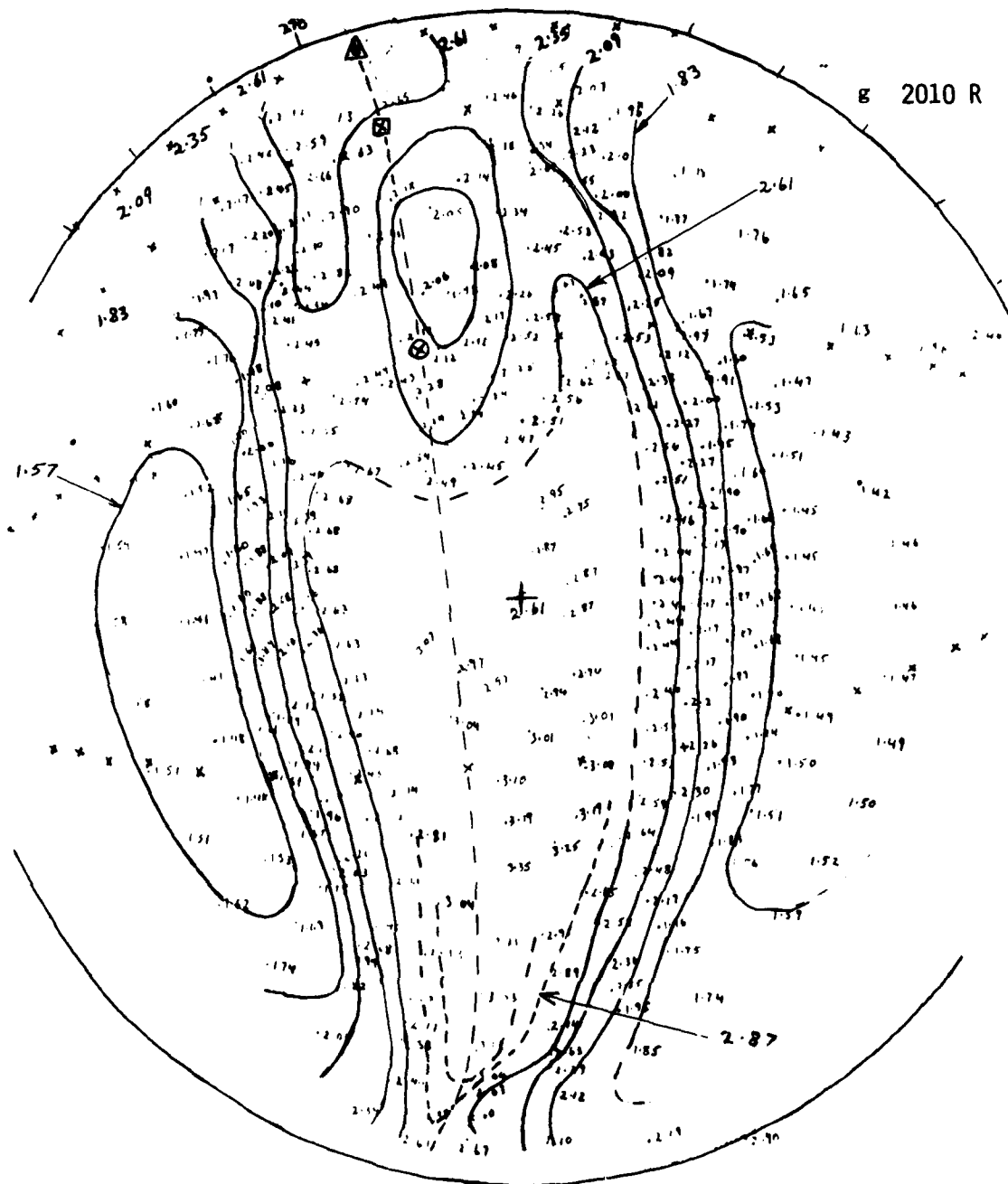


Figure 4g. Contour plots of the 6300 Å-afterglow radiance projected to position 7 of A/C 55-3120. The multiplier is 2010 R.

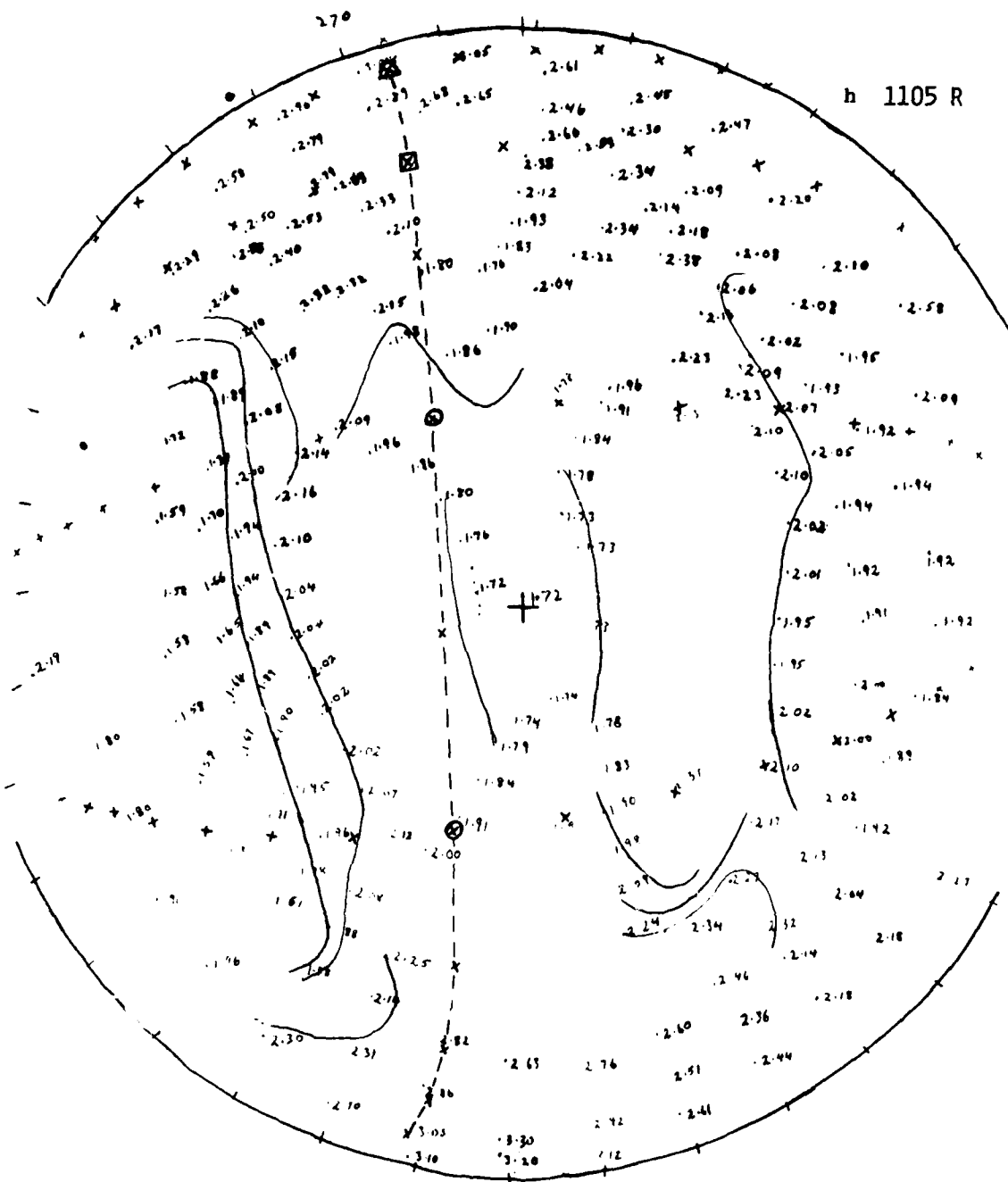


Figure 4h. Contour plots of the 6300 Å-line afterglow radiance projected to position 8 of A/C 55-3120. The multiplier is 1105 R.

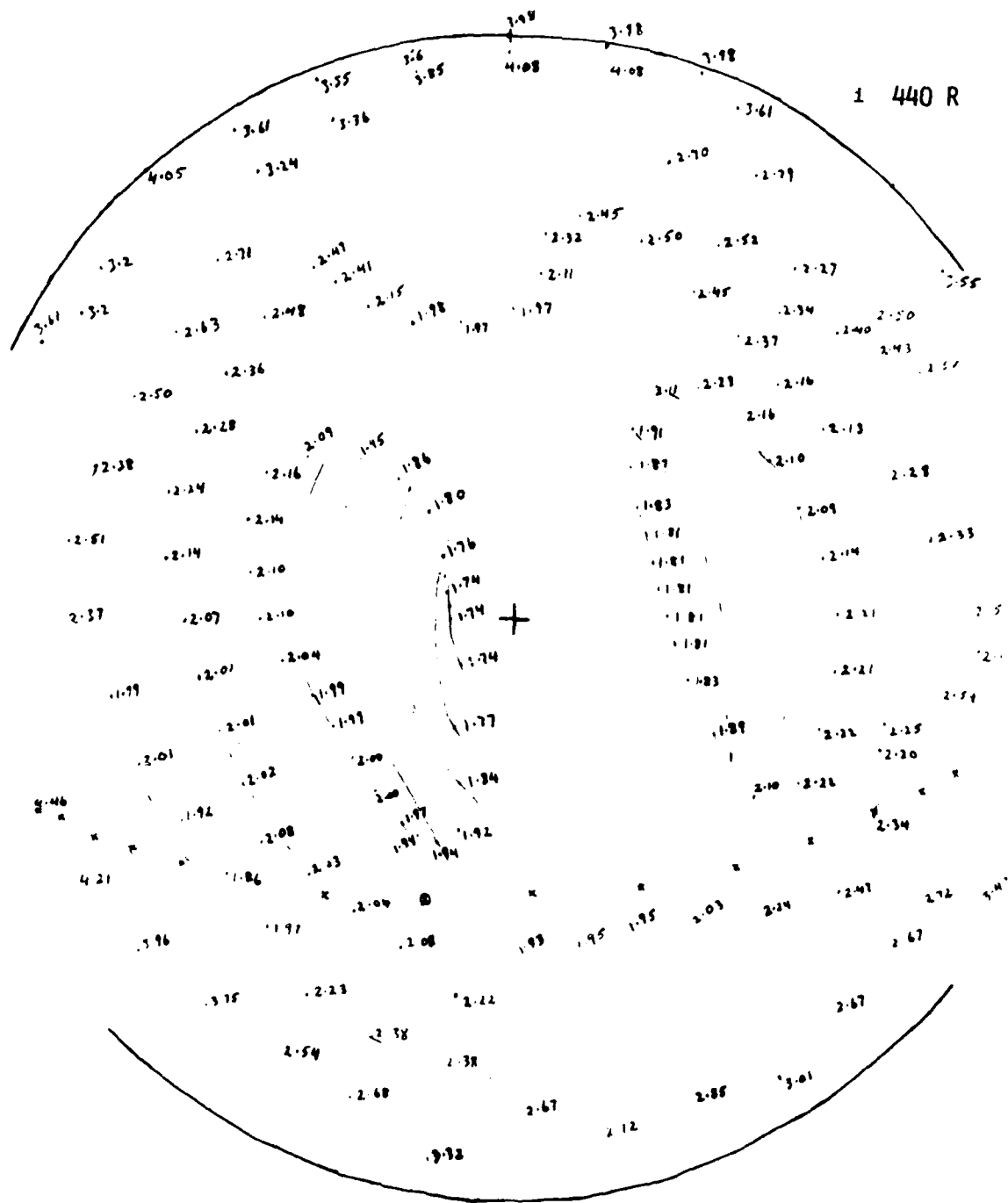


Figure 4i. Contour plot of the 6300 Å-line afterglow radiance projected to position 9 of A/C 55-3120. The multiplier is 440 R.

Table 3. Times of image radiance contour plots (sec)

	<u>Image</u>	<u>T after L</u>	<u>T after I</u>	<u>II</u>	<u>III</u>	<u>IV</u>
1	(339 -- 27° 50.5', 67° 17.7'*)	385	85	5	-	-
2	(400 -- 27° 51.1', 67° 19.8')	463	163	83	3	-
3	(437 -- 27° 53.7', 67° 29.6')	488	188	108	28	-
4	(484 -- 27° 55.6', 67° 36.4')	548	248	168	88	8
5	(480 -- 27° 57.2', 67° 42.4')	600	300	220	140	60
6	(501 -- 28° 00.3', 67° 50.0')	700	400	320	240	160
7	( 28° 01.9', 67° 59.7')	750	450	370	290	210
8	( 28° 09.6', 68° 28.6')	1005	705	625	545	465
[Aircraft Turns 180°]						
9	( 28° 19.6', 68° 05.5')	1320	1020	940	860	780

\* Altitude of Atlas-Centaur rocket in km -- latitude N, longitude W of the aircraft measurement platform.

The views of the exhaust trajectory in Figs. 2 and 3 indicate these data-reduction intercepts. Horizontal straight lines perpendicular to the track are curved in the all-sky projection. Zenith angles for Fig 4a-i are shown in Fig. 4a.

This first reduction of the video camera data was done by photographic photometry from a display monitor, principally because this procedure permitted more smoothing of the "grainy" scene brightnesses by summing frames. The initial analog record of the afterglow has also been copied onto digital tape for processing using AFGL/OPR's video image analysis system, whose integration-storage capacity is at present only 4 full frames at 5-bit radiometric precision; unless image data are stored offline through AFGL's central computer (which requires further programming), this analyzer does not provide sufficient smoothing over a useful dynamic range. In practice, 30 full video frames were summed by photographing the screen for 1.0 sec.

The data tape was played back on a 7½" x 10" (Tektronix Model 632) monitor, with display gain held in the low to mid-range to maintain linearity of the screen's radiance with input signal voltage (Ref 20). The screen was photographed from 2.3 m with a long focus (200-mm) lens so as to minimize radial distortion in the new images. A fine-grain, high-contrast 35 mm film was used (EK Pan-X). Following the usual calibration procedure, we placed a step wedge on the film (also at 1.0 sec exposure, although in fact this precaution against error due to reciprocity failure turns out not to be necessary), which we hand-developed for uniformity in a small reel tank. The density distribution on the 35 mm images were accessed with our two-dimensional scanning microdensitometer, and the resulting equidensity plots were then converted to distributions of exposure in the film-plane using this step wedge calibration (the procedure is the same as that for the EXCEDE: Spectral (Section 4) and earlier radiometrically-calibrated photographs).

Film-plane irradiances are proportional to radiances at the video monitor, which to the extent that the taping and playback systems respond linearly are proportional to the initial irradiances at the video camera's photocathode. These irradiances, when corrected for non-uniformity of response across the field of the wide-angle lens and taking video camera (and also the display monitor), are in turn proportional to the radiances in the glow cloud -- the physically-important quantity. We made this correction (which is expected to be same in all frames, that is, time-stationary) by adjusting the measured natural-background 6300 Å sky radiance distribution to its (van Rhijn, Ref 13) dependence on zenith angle. The specific vignetting-correction procedure is as follows. In an early video frame (at 0535:48 UT, from which Fig 4b was derived, the artificial airglow is limited to a small (~10° x 15°) region at the western edge of the image; the remaining exposure is due to the natural 6300 Å nightglow. The measured apparent irradiances  $E'$  are related to the irradiance  $C'$  at the frame center by

$$\frac{E'}{C'} = V_i V_R ,$$

where  $V_i$  is the system vignetting or overall instrumental response ( $V_i \leq 1$ ) and  $V_R$  is the van Rhijn path-length factor through the nightglow ( $V_R \geq 1$ ), and we have assumed that the airglow intensity changes little over the field of view other than by pathlength. The  $E_i$ 's were read point by point from the exposure contours in the test frame, and the van Rhijn factors  $V_R$  were taken from Ref 13 for a 350 km 6300 Å emission altitude ( $V_R$  varies very little between 300 and 400 km, the expected limits of the airglow profile's peak). The exposures at each elevation-azimuth position in the data frames were then manually corrected by the factor  $E_i/V_R (= V_i C')$ . The maximum value of  $V_i$  reaches about 3, near some 80° zenith angles. Note that this correction takes into account the two-dimensional nonuniformity of response by the imaging and reproduction systems.

This procedure gives relative radiances within individual video frames, with an estimated mean accuracy of + 60%, - 40%. As the camera's automatic gain controls were used to allow it to respond to the necessarily wide dynamic range of scene brightnesses, an absolute calibration for each frame was taken from the zenith radiances measured by the 2°-field 6300 Å photometer (shown in Fig 1 and Fig 37 of Ref 1). The contours in Fig 4 are presented as successive 10 percent decreases in scene radiance from the radiance at the aircraft's zenith when the maximum radiance was near the center of the frame (i.e., when the glow comes overhead), and 10 percent decrements from the glow's peak in earlier frames.

#### LATERAL GROWTH AND TIME DEPENDENCE OF GLOW RADIANCE AT FIXED POSITIONS

The isophote plots show the expected decrease in brightness near the launcher's trajectory at the lower exhaust altitudes, presumably due largely to depletion of the ionosphere's  $O^+$  ions. They also indicate a northward drift of the "axis" of the afterglow, which we had initially ascribed to F-region wind (Ref 1). Inconsistencies in the direction of the "centerline" of the glow region within individual frames, however, lead us to the conclusion that this apparent motion could be caused by

errors in the heading and other attitude angles of the aircraft. Its positions were taken from the navigator's log, and attitude cannot be checked from star fields as few stars are imaged through the narrow wavelength-band filter.

Positions along the one-dimensional traces (Fig 5) have been corrected for the aircraft's motion; the isophote plots in Fig 4, from which the traces were compiled, are projections to the individual aircraft positions. The correction of elevation and azimuth angles was made with an adaptation of a navigation program designed to be run on a small digital computer. The radiances in Fig 5 are also corrected to the local zenith, that is, the variation due to the change of sight path length with zenith angle has been removed (as discussed earlier). The horizontal distance scale on the abscissa was assigned with the assumption that the "centroid" of the glow in the vertical direction remains at the initial exhaust altitude (as also noted, a net upward transport is expected).

The minimum at the lower exhaust altitudes, and the apparently-related flattening of the traces at higher altitudes, effectively precludes direct assignment of meaningful halfwidths to the radiance traces. (Because of the low accuracy at 257 km exhaust altitude, which is due to both compression of the zenith angle scale and uncertainty in the vignetting correction near the edge of the all-sky frame, we have not attempted to derive transport data from these lowest-altitude radiances.) We used instead the separation between the points of maximum slope in Fig 5 to compute effective diffusion coefficients. (In a Gaussian with halfwidth to 1/e maximum  $\sqrt{2}\sigma$  -- i.e., described by  $\exp(-(x^2/2\sigma^2))$  -- the slope is a maximum at  $x = \sigma$ .) The slope of the plot of the square of half this distance (i.e., the half-width) against the time after the exhaust molecules are deposited can be interpreted as 4 x the effective diffusion coefficient, as described in Ref 10. The figure derived for each of the three highest exhaust altitudes is about  $2\frac{1}{2} \times 10^7 \text{ m}^2/\text{sec}$ , which is close to the expected diffusion coefficient of  $\text{H}_2$  near 400 km (see Fig 2). This finding suggests strongly that the wide spread of the glow is due principally to reactions of the ejected  $\text{H}_2$  molecules rather than to the  $\text{H}_2\text{O}$ .



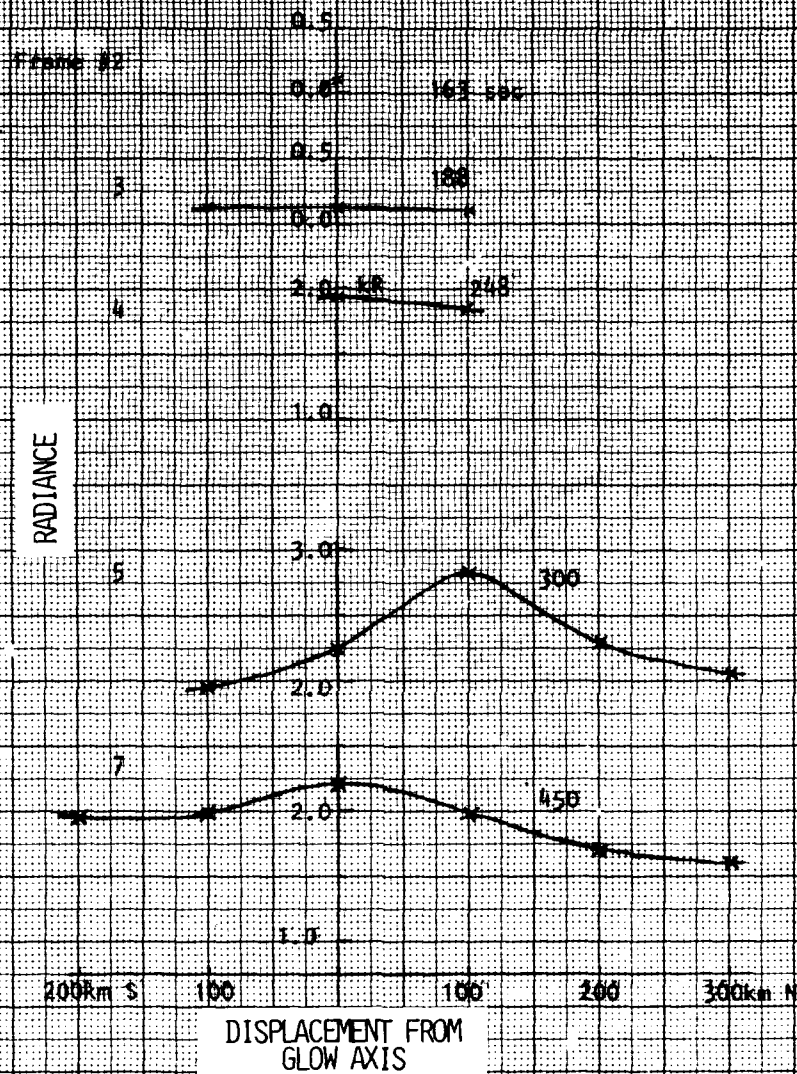


Figure 5a. 6300 Å local-zenith brightness along lines perpendicular to the direction of the launcher's trajectory at 257 Km.

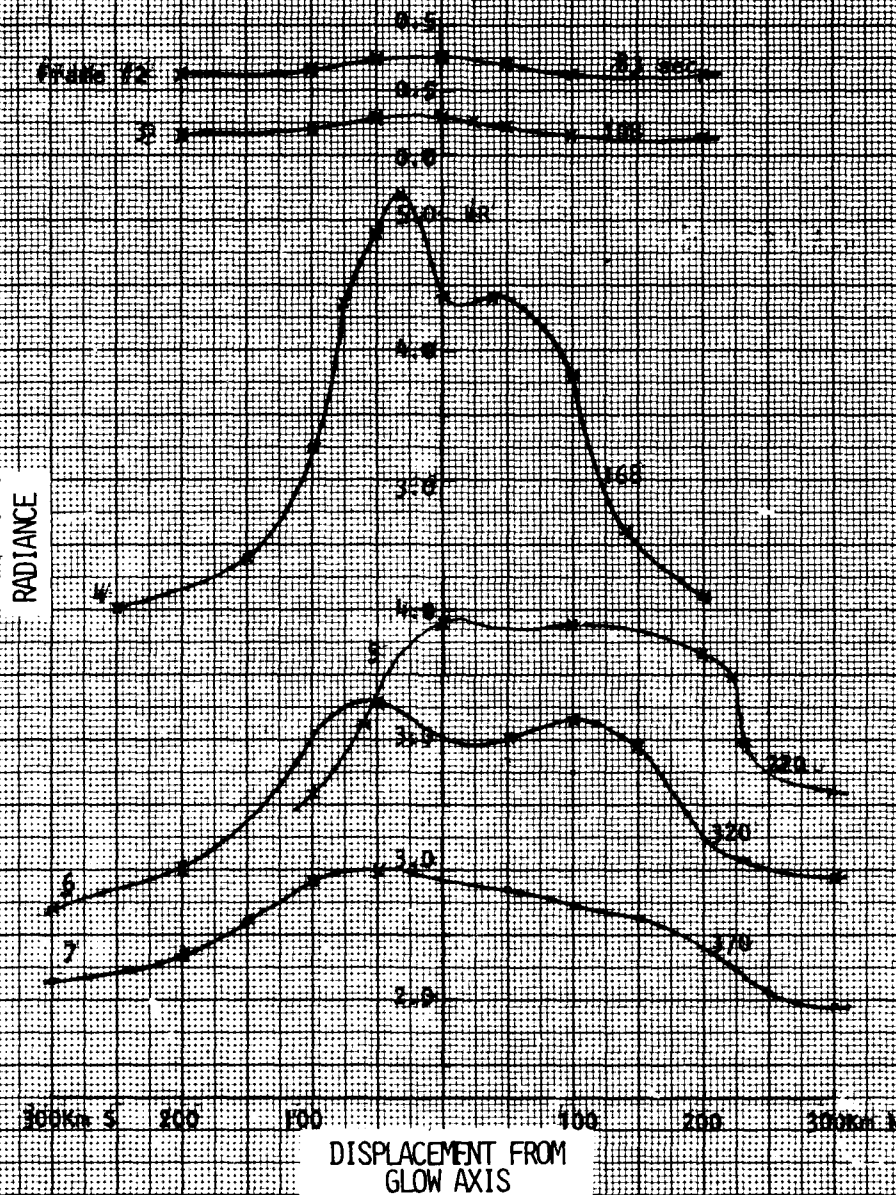


Figure 5b. 6300 Å local-zenith brightness along lines perpendicular to the direction of the launcher's trajectory at 334 Km.

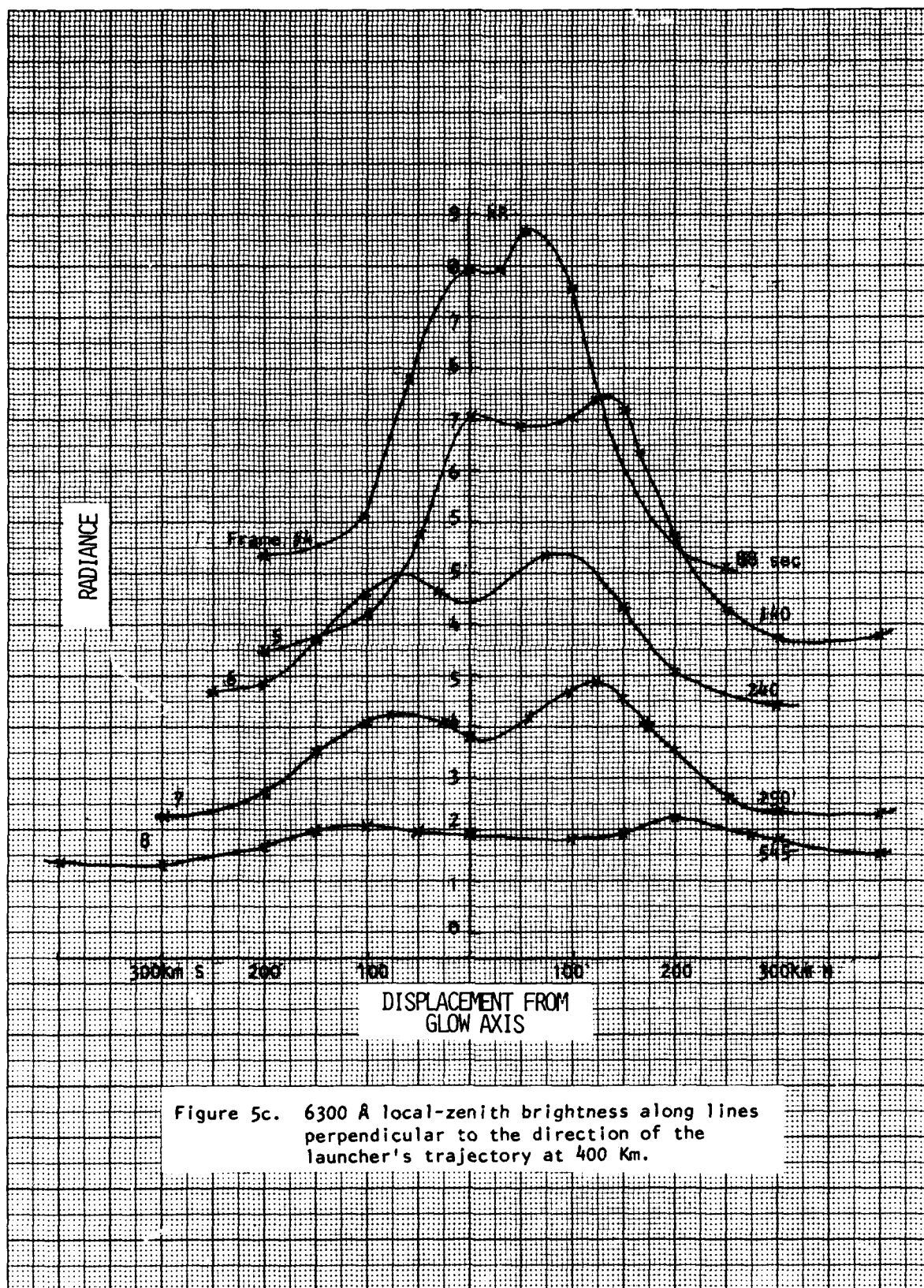


Figure 5c. 6300 Å local-zenith brightness along lines perpendicular to the direction of the launcher's trajectory at 400 Km.

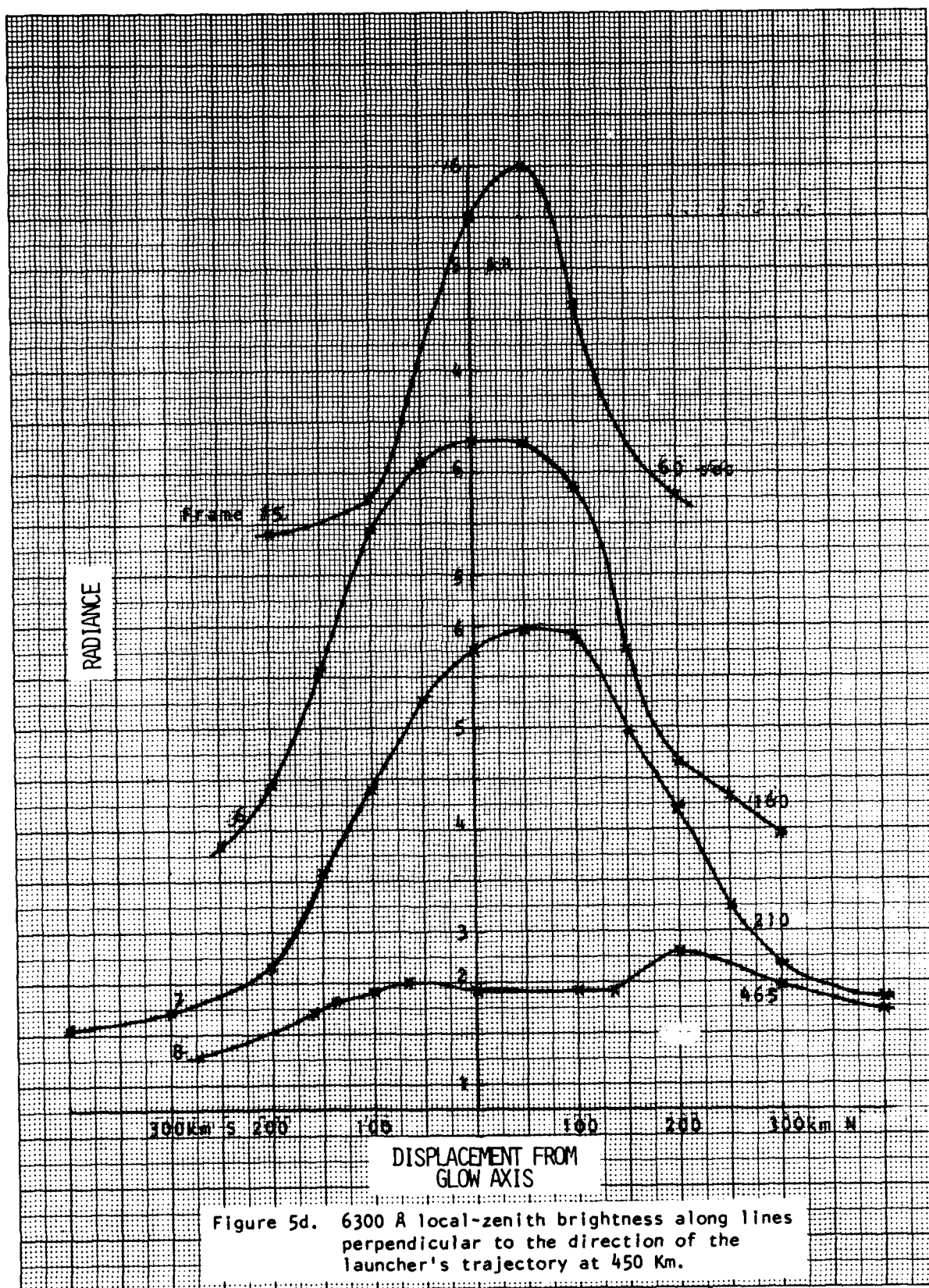


Figure 5d. 6300 Å local-zenith brightness along lines perpendicular to the direction of the launcher's trajectory at 450 Km.



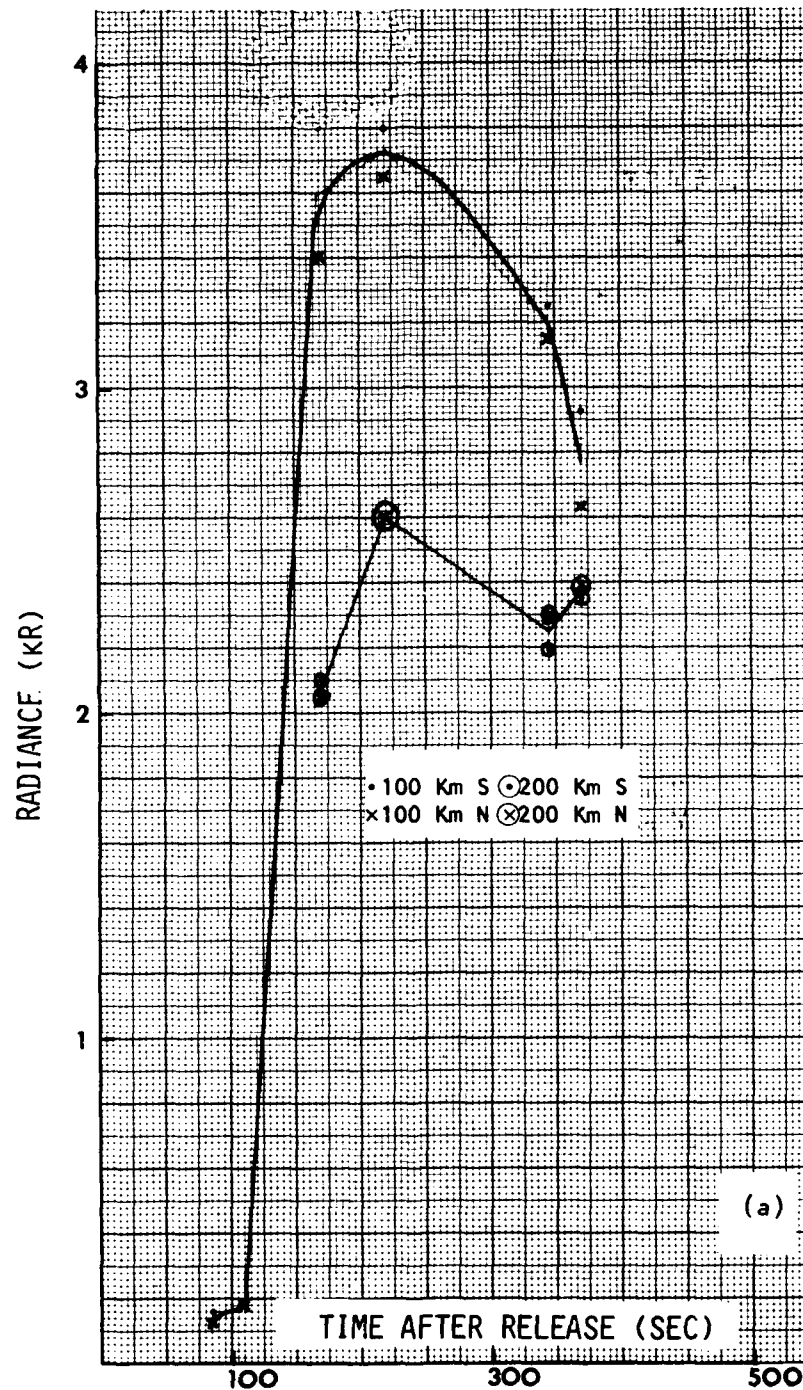


Figure 6a

Time variation of the 6300 Å local-zenith brightness at 100 and 200 km from the exhaust track's center, at 334 km altitude.

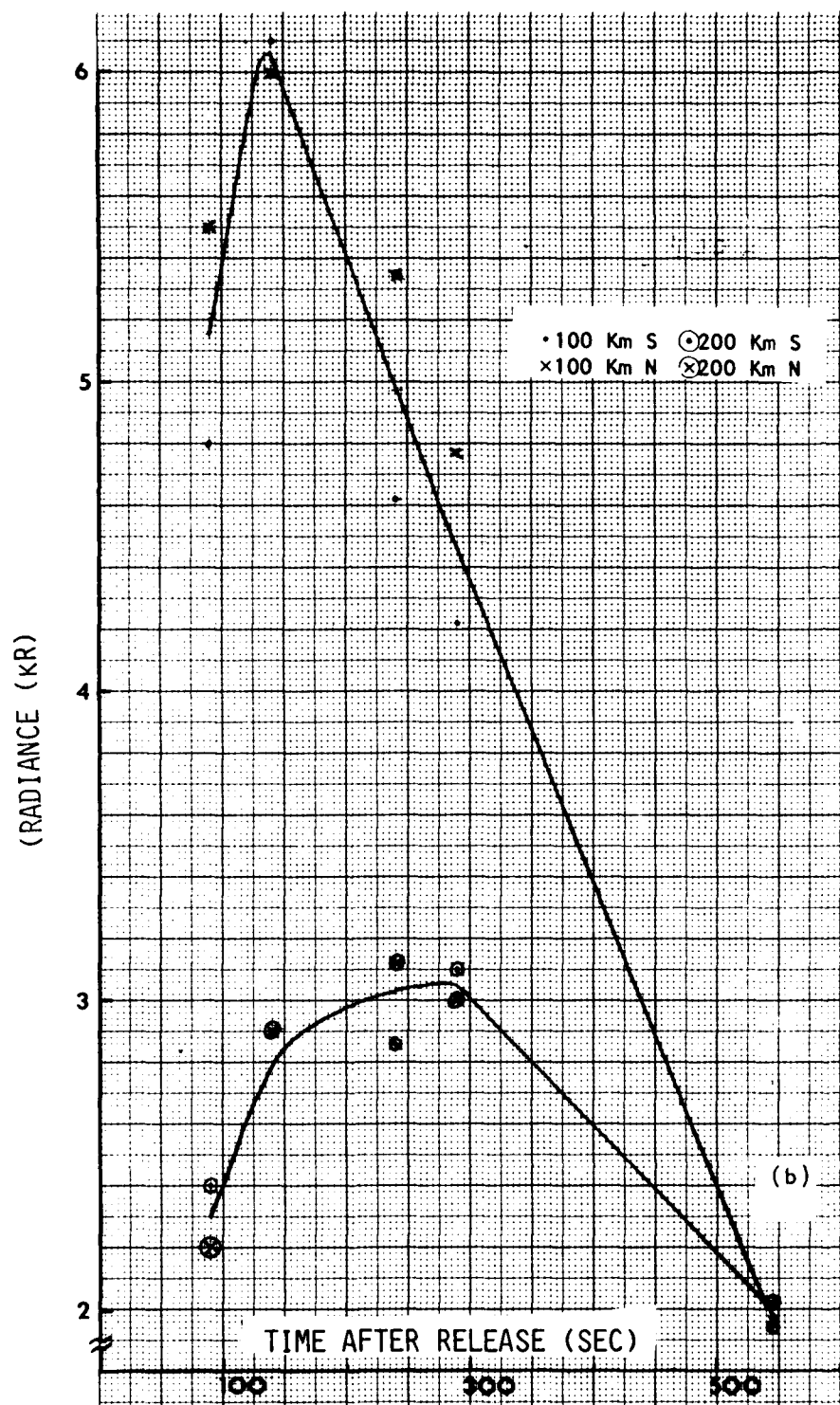


Figure 6b. Time variation of the 6300 Å local-zenith brightness at 100 and 200 km from the exhaust track's center, at 400 km.

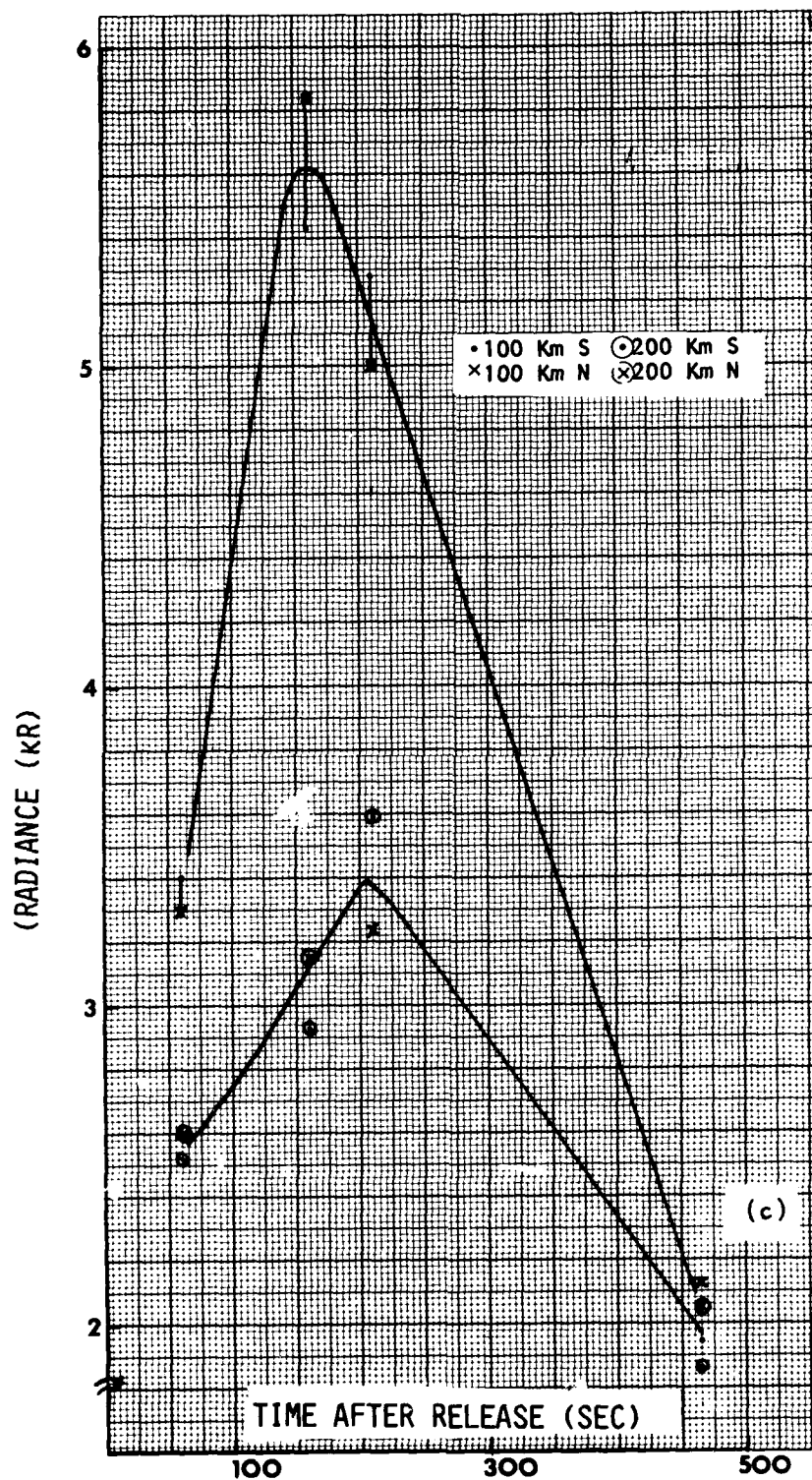


Figure 6c. Time variation of the 6300 Å local-zenith brightness at 100 and 200 km from the exhaust track's center, at 450 km.

Figure 6 shows the time dependence of local-zenith 6300 Å radiance 100 and 200 km horizontally from the exhaust trajectory. The time constants for decay of the glow are longer than the lifetime of the  $O^1D$  state, which indicates (as expected) that excitation is continuing along these sight columns during the data period.

Further information on the spatial and temporal dependence of the  $O^1D$  afterglow in the first ~15 min after exhaust of  $H_2$  and  $H_2O$  in the F region can of course be derived from Fig 4, which in effect presents all the radiance information present in the sampling of low light level video frames recorded from the aircraft.



## SECTION 2

### ATMOSPHERIC SWIR RADIANCE STRUCTURE MEASURED FROM AIRCRAFT ALTITUDE

#### INTRODUCTION

During April and September 1979, and August 1980, the Defense Nuclear Agency conducted a series of aircraft-based measurements of the space-time structure and solar illumination dependence of yield of short-wavelength infrared radiation from the auroral particle-excited ionosphere. The data were taken from AFGL's Optical Flying Laboratory (USAF NKC-135A S/N 55-3120) at auroral latitudes near 70° W longitude (1979, flights from Pease AFB, NH) and 147° W longitude (1980, from Eielson AFB, AK), with a cryocooled radiometer having a 0.36° (6 millirad) square field of view pointed near the magnetic zenith. The principal goal was to establish the spatial and temporal correlations of 2.8 - 3.1  $\mu$ m-band emission with the deposition of ionizing-particle energy in the dark and sunlit atmosphere, at a 1 Km footprint.

A detailed Test Plan for the aircraft missions, describing the radiometer with its coaligned energy input-referencing air fluorescence photometer and supporting instruments, and outlining a procedure for analyzing the sky radiance distribution data, is in Appendix 1 of Ref 21. Measurements of the atmosphere's Rayleigh-scatter background when particle-deposition altitudes are sunlit are presented in Section 5 of Ref 1, which also discusses briefly and qualitatively the 1979 flight data. A preliminary review of the data set was given in Ref 22, along with background information on calibration of the photometer.

Summarized results from earlier flights of a 160-millirad-field SWIR radiometer and photometer (footprint 17 km at emission altitudes) are given in Ref 21. In this Section we evaluate the higher signal/noise data segments from the narrow-field instruments, focusing on the

dependence of the output-input correlation and infrared chemiluminous yields on auroral, solar-illumination, and measurement parameters.

#### BACKGROUND

The source simulating excitation by radiations from nuclear bursts is the energetic ( $\sim 5$  keV) electrons from the magnetosphere that precipitate into the high-latitude upper atmosphere to produce the optical and infrared aurora. The input fluxes and peak altitudes of energy deposition are measured from the air fluorescence these particles excite at visible wavelengths. Radiance in the  $N_2^+$  First negative (0,0) 3914 Å band, which is known to be closely proportional to the total column energy deposition, is monitored by a photometer whose field of view coincides with that of the 2.832 - 3.125  $\mu m$  (FWHM)-sensitive radiometer. Spatial distributions of input in the vicinity of the radiometer-photometer fields (and auroral type) are determined each 1/30 sec by a low-light-level video camera, backed up by a photographic all-sky camera. A second radiometer monitors intensity in the hydroxyl vibrational (Meinel) bands, whose fundamental presents a very slowly-varying background in the SWIR radiometer signal, which is believed (Ref 21) to be due to nitric oxide overtone emission. A filter photometer measures ratios of emission intensity from which altitude profiles of energy deposition can be determined (Appendix II of Ref 23); and in some of the missions (in 1980) altitude profiles of ionospheric electron density, from which instantaneous energy-input profiles can also be estimated, were measured along the aircraft's track by the incoherent-scatter radar at Chatanika, AK.

The atmospheric species ionized, dissociated, and raised to excited states by direct primary electron impact and various secondary processes react with ambient molecules and atoms, producing further excited species that radiate at infrared wavelengths. Chemiluminous yields ("efficiencies") in emission features, and the times for grow-in and decay of the infrared radiations, serve (with emission spectra) in identifying the radiating species and the excitation/de-excitation processes (a further goal of the aircraft program). This information

is needed both to permit scaling of simulation data to the altitude profiles of energy deposition that result from atmospheric nuclear explosions and to determine the overlap of the emission spectrums on wavelength regions to which surveillance systems are designed to respond.

Resolution of the radiance measurements discussed here ( $\lesssim 1$  km at energy deposition altitudes, and 1 sec temporal) is intended to allow SWIR output and "clutter" to be correlated with energy input at the scale of interest to spaceborne sensors. Quantification of the visible-SWIR, input-output correlation would also permit use of the existing extensive photographic data base on visible skyglows resulting from past atmospheric nuclear tests to characterize sky background variations in the 2.8 - 3.1 $\mu$ m band.

#### APPROACH

The atmosphere above the subsonic jet aircraft's operating altitude of  $\sim 35$  kft is essentially transparent to downward-directed radiation between 2.8 and 3.1 $\mu$ m; this band encompasses about half of the emission in the NO molecule's overtone ( $\Delta v = 2$ ) sequence as excited in chemiluminous reactions following hard particle irradiation of air (see, for example, Fig 2 of Ref 1; the fractional response of the radiometer to the sequence is derived in Ref 21). Initially, the atmospheric emission at these wavelengths was measured from the NKC-135A aircraft using a radiometer and coaligned photometer having 1/6-radian fields of view pointing toward the zenith, with an effective signal integration time of 30 sec (Ref 1).

Results of these earlier data flights (Ref 1), which refer to air between  $\sim 100$  and 150 km altitude in which  $\sim 10^{5-6}$  ion pairs/(cm<sup>3</sup> sec) are being produced, can be summarized as follows.

1. SWIR output follows particle-energy input in time and space to within the instrument's resolution;

2. The output of SWIR photons increases linearly with input at auroral dosing rates;
3. Lumped-parameter efficiency for emission of what is interpreted as the vibrational overtone of NO shows statistically-significant differences among both long (1/2 hr) and short (1 min) segments of data, with yields ranging from 0.4% to 0.7%.

These results from the wide-field instrument flights are by and large consistent with those from rocketborne radiometers pointed toward aurora (Ref's 1, 23), and (with the exception of the as yet-unexplained variability) with rate-coefficient data from laboratory investigations of vibrational excitation of the nitric oxide molecule.

These earlier flights also showed that measurements of both the SWIR emission and its referencing visible air fluorescence have adequate signal/noise when the altitudes at which precipitating particles deposit their energy are sunlit (as reviewed in Section 5 of Ref 1 ). Operating near the equinoxes and navigating to compensate for wind drift, the aircraft is able to hold the solar depression within the requisite  $\sim 7-10^\circ$  range for 2-3 hours while staying inside the (average,  $Q = 3$ ) auroral oval and permitted airspace. We note that identification of day-night differences in SWIR dynamics and yield would indicate a deficiency in current understanding of the processes that lead to vibrationally excited NO in particle-irradiated air, as current DoD code models of the sky background do not include any effects of excitation by solar photons. (Additionally, no difference from night to twilight (or day) in the concentrations of ambient species that affect the  $\text{NO}^+$ -producing reaction chain can be identified.) To assess the behavior of SWIR emission during "sunlit" aurora, several of the flights of the narrow-field instruments were made at the twilight transition, with auroral energy-deposition altitudes partially or totally sunlit.

The narrow-field instruments are installed tilted  $15^\circ$  forward of the static airframe's vertical, so that at auroral latitudes they point in the direction of the geomagnetic field when the fuselage (which is normally pitched  $2^\circ$  nose-up in flight) is moving southward along a magnetic meridian. In this pointing mode the precipitating auroral electrons within the fields of view have unique initial energy spectrums and thus produce a defined altitude profile of atmospheric excitation. The fields are precisely coaligned ( $< 0.03^\circ$  estimated error) by means of a specially-designed optical bench, construction of which is documented in Ref 24. An independent multi-channel photometer with a somewhat wider field ( $2^\circ$  full angle) is installed 43 feet to the rear of, and approximately aligned with, the prime instruments; its major function is determination of energy deposition altitudes from the column intensity ratios of the  $O^1D$  6300 Å and  $N_2^+$  4278 Å auroral features (as described in Appendix II of Ref 23). (Calculations of the collisional quenching of  $NO^+$  by O (Ref 25) in fact predict a minimum of SWIR yield near 100 km, which may be present in some of the rocket radiometry data (Ref 1)).

#### ALTITUDE PROFILE DETERMINATIONS

The two color method (Ref 23 and earlier references therein) quantifies the self-evident principle that the altitude profiles of emission of individual molecular bands and atomic lines are functions of the atmosphere's composition profile, and so reflect the penetration profile and thus the energy distribution of the primary precipitating auroral particles. Major assumptions in the theory are 1) uniqueness of this energy spectrum within the photometer's field of view, 2) validity of its assumed shape (Maxwellian), and 3) steady state excitation/depopulation of the upper state of the  $O^1D - ^3P$  6300 Å transition. The first condition is satisfied during segments of flights in which the aircraft fuselage's heading is near  $180^\circ$  (magnetic); but in others, particularly the twilight-transition missions where the trajectory is chosen to maintain constant solar depression, the angle between the geomagnetic zenith and the instrument's field can be as high as  $26^\circ$  ( $13^\circ + 13^\circ$ ;  $\sim 100$  km horizontal

separation between the  $N_2^+$  and OI red line emission altitudes). Thus the confidence placed on altitudes derived by this method depends on both aircraft heading and the scale length of uniformity of the aurora-producing "beam." The time to reach steady-state conditions in OI 6300 Å is at least one lifetime of the upper state against radiative and collisional depopulation, which is about 30 sec; thus the method provides more reliable altitudes of auroral forms that are spatially and temporally constant at this scale.

Additionally, deviations from the assumed shape of the particle energy spectrum may be a potential source of error in the deposition altitude profile. In consequence the 1980 flights were coordinated with Chatanika radar scans which determined altitude profiles of ionospheric electron densities, from which input rates can be derived with the assumption of constant deposition rate over the previous ~10 sec (refer to Ref's 1 and 23 for a review of the measurement concept). A total of some 15 hr of coordinated measurements in 5 data missions was made, with the aircraft flown back and forth along (or near) the radar's magnetic meridian. An attempt was made to synchronize the tracking radar's elevation scan with the aircraft's trajectory so that the radio-meter and photometer fields would overlap the 10 millirad radar field at 100 km altitude. Flight profiles that would obtain an adequate sampling of both sunlit and nighttime aurora were designed for each mission, with the aircraft entering the data taking track when the solar depression reached 7° at evening twilight.

The instruments' 100-km intercept was flown 1° 02' 43" N and S along the meridian through Chatanika (between 64° 03' 31" and 66° 08' 53"), which is a total distance of 266 km when the 29° magnetic declination is considered. At the extremes of this track the radar beam's zenith angle is 49.4°, and its angular speed is 0.056 degrees/sec (it is 0.13 deg/sec when the aircraft is in the zenith). The signal integration time is a factor 3-6 greater than in a previous aircraft-radar coordination (Ref 1). The number of two-way meridian passes varies between 3 and 6 in the 1980 flights.

Since operational considerations required that the radar facility be given a preprogrammed tracking routine, no provision could be made in advance for the effect of winds on the aircraft's position. Therefore some offsets developed between the two fields. (Further, crosswinds frequently result in "crabbing" of the airframe, which offsets the instrument fields from the predetermined flight track.) To mitigate this problem a series of checkpoints at which the aircraft would arrive was set up. The aircraft was not permitted to deviate from its course along the predetermined track to "chase" auroral forms, which of course lessened the probability of its encountering intense particle bombardment.

Electron densities along the scanning beam have been received from the radar group; these have not yet been converted to the contour plots (of the type shown in Fig's 20 and 21 of Ref 1) needed to determine the energy input rates within the aircraft instruments' field of view. We note that the inherent ambiguity (time-space mix) of the energy input rate profiles derived from elevation scans from a single instrument location limits the application of the radar-backscatter data in interpreting the SWIR radiation data, as the spatial distribution of input flux can change before the radar beam completes its traverse across the column defined by the instrument field (refer to the comments in the report on the earlier coordination, Ref 1). Pending reduction of these aircraft data and an assessment of effective offset of fields, the peak energy deposition altitudes presented here have been derived using the spectroscopic-ratios method.

#### DATA REDUCTION

A total of 15 high signal/noise data segments from 10 flights, which included ~70 min of measurements, was selected from the data base for the initial analysis. Auroral precipitation intensity ("input") was typically  $> 1 \text{BCII+}$ , and the segments were selected to include totally sunlit, partially sunlit, and totally-dark periods. A typical set of calibrated radiance traces, showing the 3914 Å band fluorescence, 2.8 - 3.1  $\mu\text{m}$ , and  $\Delta v = 2$  hydroxyl is in Fig 7 (OI 5577 Å intensities

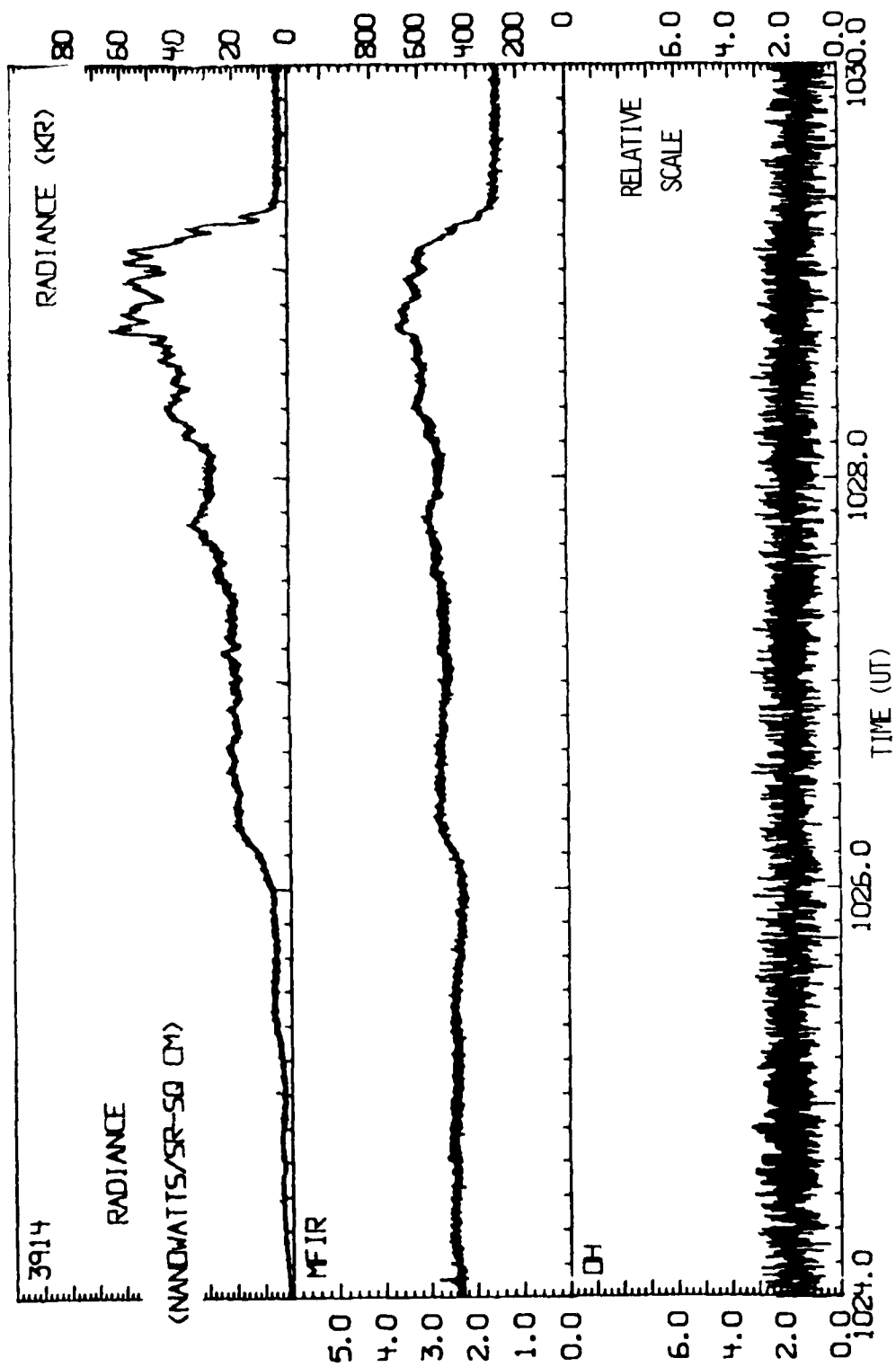


Figure 7. Data Segment 14, Flight 027, 19 Aug 80 (see Table 4). The trace is a running average of 11 consecutive samples spaced 0.01 sec apart, plotted each 0.2 sec (i.e., half the original radiance data points are included).



measured by the narrow-angle photometer are not shown). The wider-field OH overtone ( $1.66 - 1.74\mu\text{m}$  FWHM) airglow monitor's optic axis pointed to the zenith in 1979 and was nominally coaligned with the prime instruments in some of the 1980 flights. The ratio of in-band OH fundamental to measured overtone emission intensity has been calculated to be about 2.5 : 1; in practice, variations in OH background over the short data segments are so small that they do not affect the analysis.

The fluorescence photometer installed in 1980 was a new design whose initial calibration is only indirectly applicable to the measurements made in 1979. A final calibration for 1979 data was made by cross-correlating the raw output voltage readings from the instrument with the absolute intensities that were measured by the aircraft's 12-channel filter photometer (Ref 1), as described in Section 4 of Ref 22. No instrument performance irregularities were encountered in the 1980 missions.

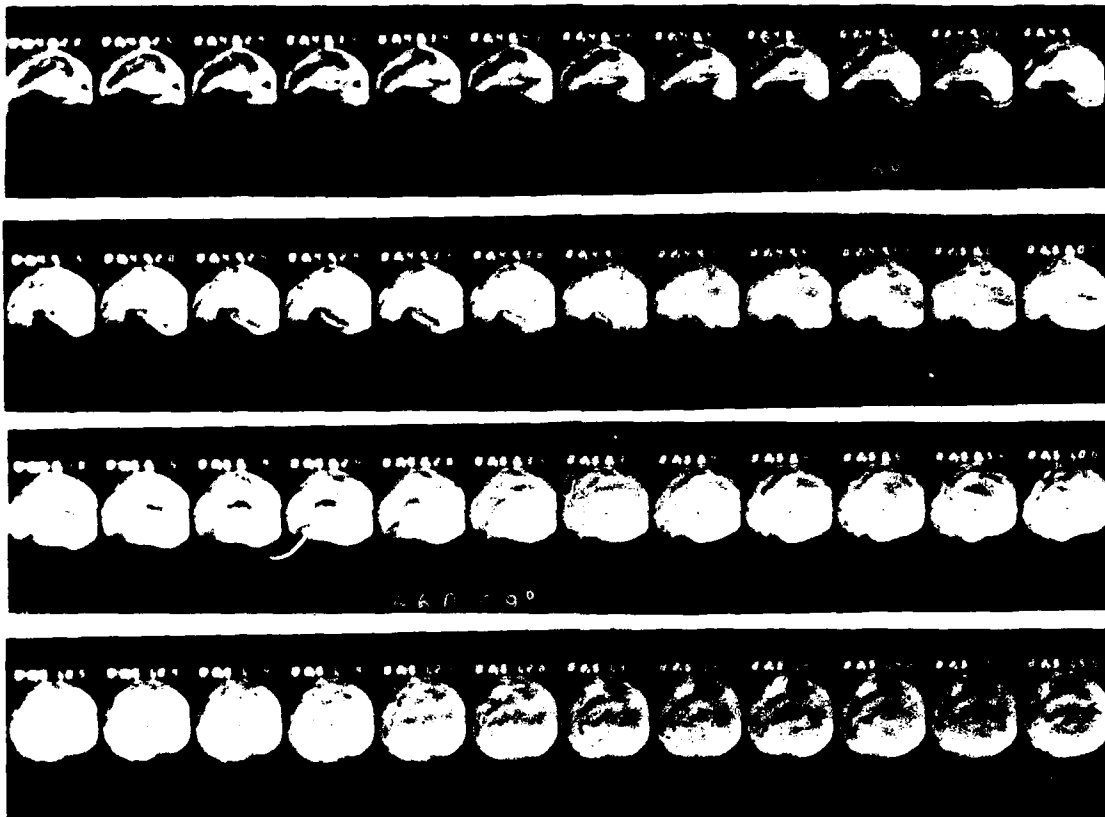
Measurement and geophysical conditions for the 15 traces selected are shown in Table 4, and montages of all-sky photographs ( $165^\circ$  circular field,  $4\frac{1}{2}$  sec on EK2475 at  $f/2$ ) of the auroral input distribution are in Fig 8. The negatives for each segment have all been printed with the same exposure to indicate relative scene brightnesses. Segment 10 has been omitted from Fig 8 because the signal/noise ratio in its radiance traces was found to be below that acceptable for analysis.

The entries in Table 4 are as follows. The first column lists the identifying numbers assigned to each data segment. Next is flight date and time of meridian passage at the midpoint of the data segment (which is needed to determine solar elevation), whose duration is in the third column. The next three columns give aircraft position, fuselage heading, and direction of the flight trajectory; the latter two azimuths typically differ by a few degrees because of crosswinds. (When the fuselage is oriented at  $180^\circ$  magnetic, the coaligned input- and output-measuring instruments point directly up the field lines; yaw of the airframe by azimuth angle  $\phi$  results in a misalignment of only  $\phi \sin 13^\circ = 0.225\phi$ .)

Table 4. Auroral and observation parameters during SWIR enhancements

CASE	FLIGHT/DATE No. idian Passage	TIME (Z)	AFC POSITION Lat Long	HEADING True Req	TRANSITORY AZIMUTH (degrees)	SOLAR ANGLE (net 13 deg corrected)	SOLAR ANGLE (13 deg corrected)	ILLUMINATED HEIGHT (m4, 100 ft)	INTD (6300/4278) (507/3714) photons/photon	PEAK ALTIMETER INDEX K K P
①	907/230477 1158 170	0200 0201:20 0201:25	52.49 67.44 52.99 66.95 52.51:25 < A/C turning	017 029 017 029	012 012	-21.67 0 -21.74 0	-21.50 -21.35	453.0 455.1	6.5/16.5 <100/47.8	139.5 4 5
②	909/230477 1158	0227 0200	61.36 71.30 61.63 71.76	321 340 321 340	331 331	-10.98 0 -10.82 0	-10.75 -10.59	113.3 109.9	11.1/14.9 84.8/43.2	133.7 3 3
③		0213 0216	58.96 68.67 59.22 68.53	325 340 325 340	338 338	-12.14 0 -12.02 0	-11.91 -11.79	139.0 136.2	7.4/18.3 9/53.1	119.5 3 3
④		0220 0224	59.54 69.20 60.07 69.67	325 340 325 340	338 338	-11.89 0 -11.66 0	-11.73 -11.43	134.8 128.0	9.6/24.3 96.8/78.6	119.8 3 3
⑤		0226 0229	61.76 69.61 61.95 69.28	144 180 144 180	155 155	-12.08 0 -12.58 0	-12.31 -12.80	148.5 160.6	5.1/6.4 29.1/18.6	127.7 3 3
⑥	908/230477 1158	0637 0640	47.09 67.51 47.36 67.66	340 340 340 340	344 344	-23.42 0 -22.89 0	-23.28 -22.75	531.1 507.2	4.9/11.9 76.7/34.5	126.0 7 8
⑦	920/1804 1151	0816 0819	58.36 73.57 58.20 74.12	281 316 269 300	279 289	-9.40 0 -9.55 0	-9.18 -9.34	82.6 85.5	11.0/10.9 73.8/31.6	139.5 4 6
⑧	926/2304 1152	0816 0822	58.04 77.67 57.32 78.02	(264 292 171 168	265)* 198	-18.05 0 -10.84 0	-9.83 -10.94	94.7 117.3	6.4/8.2 65.1/23.8	127.2 3 4
⑨	927/2304 1151	0829 0823	54.77 68.83 55.05 69.13	327 336 338 340	327 3* 338 (turn)	-36.47 0 -36.62 0	-36.47 -36.40	989.9 985.7	2.5/1.3 13.7/3.6	145.1 3 3
⑩	928/2304 1151	0819 0823	57.18 76.59 56.76 77.27	238 248 238 248	238 238	-28.21 0 -28.53 0	-28.13 -28.45	397.1 409.8	4.5/11.87 (58.4/34.1)*	118.1? 3 4
⑪	923/070400 1204	0654 0704	62.99 122.02* 63.34 124.75	284 232 284 232	286 286	-9.12 0 -8.75 0	-8.99 -8.62	79.2 72.8	2.6/9.0 47.9/26.1	116.0 3 2
⑫	926/1804 1204	1125 1126	65.04 147.09* 65.16 147.36	029 340 029 340	030 030	-10.18 1 -9.95 1	-10.18 1 -9.95 1	100.8 97.0	4.1/36.6 <100/160	188.8 2 5
⑬		1159 1203	64.36 148.43* 63.93 148.95	209 177 209 177	207 207	-9.31 1 -9.61 1	-9.31 1 -9.61 1	94.9 90.5	4.4/12.49 <50/300	118.8 2 5
⑭	927/1804 1204	1024 1028	64.38 148.42* 64.93 147.45	026 338 026 338	029 029	-12.89 1 -12.13 1	-12.89 1 -12.13 1	162.8 144.2	2.6/21.2 111.8/61.5	188.8 6 5
⑮		1025 1109	65.05 147.46* 63.88 149.02	212 179 212 179	208 209	-11.45 1 -12.54 1	-11.45 1 -12.54 1	128.5 149.2	4.7/11.87 <50/370	119.5 6 5

\* After flight 023, refers to latitude/longitude of intercept at 120 km of the 15°-tilted instruments  
 \*\* 15-channel photometer readings at median auroral column brightness; in south in 1100s 999/980.8 997  
 ††† It's refer to Dallas, TX meter  
 \* Aircraft is turning to S 0015138 - 001755  
 †††† values are from narrow-field photometer



# SEGMENT 1

Figure 8a. All-sky montages of the auroral energy input distribution before and during data.

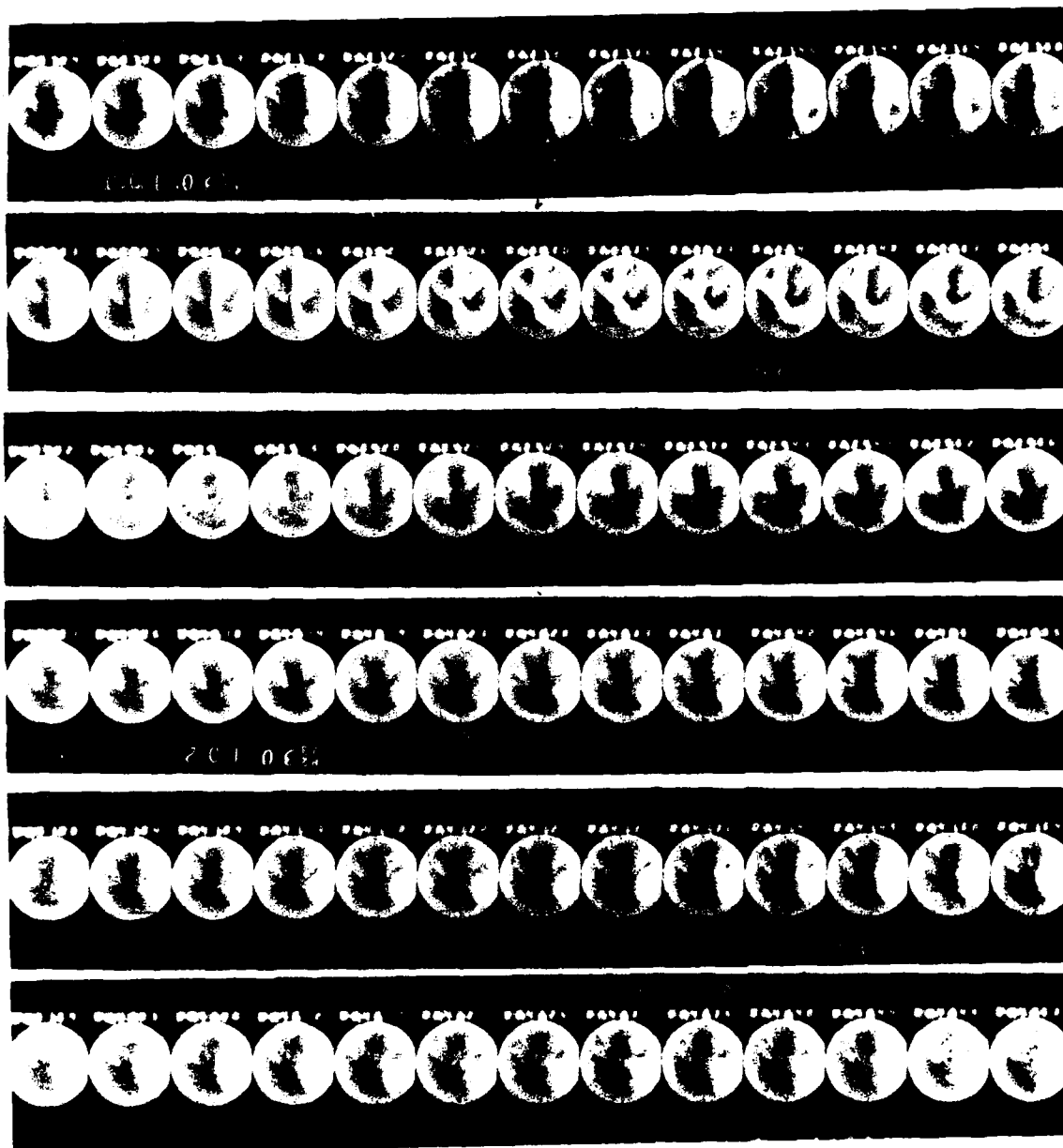


Figure 8b. All-sky montages of the auroral energy input distribution before and during data segment 2.

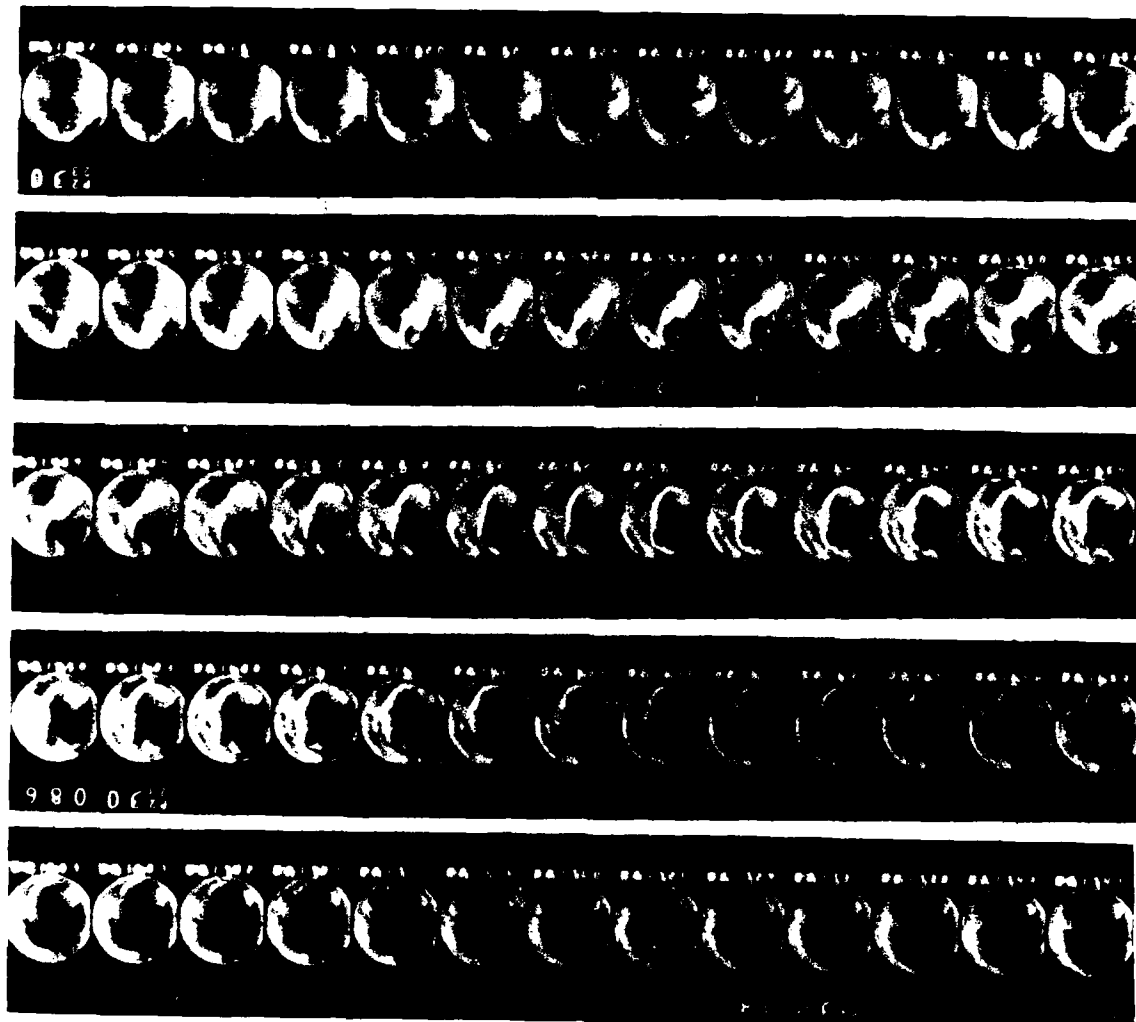


Figure 8c. All-sky montages of the auroral energy input distribution before and during data segment 3.

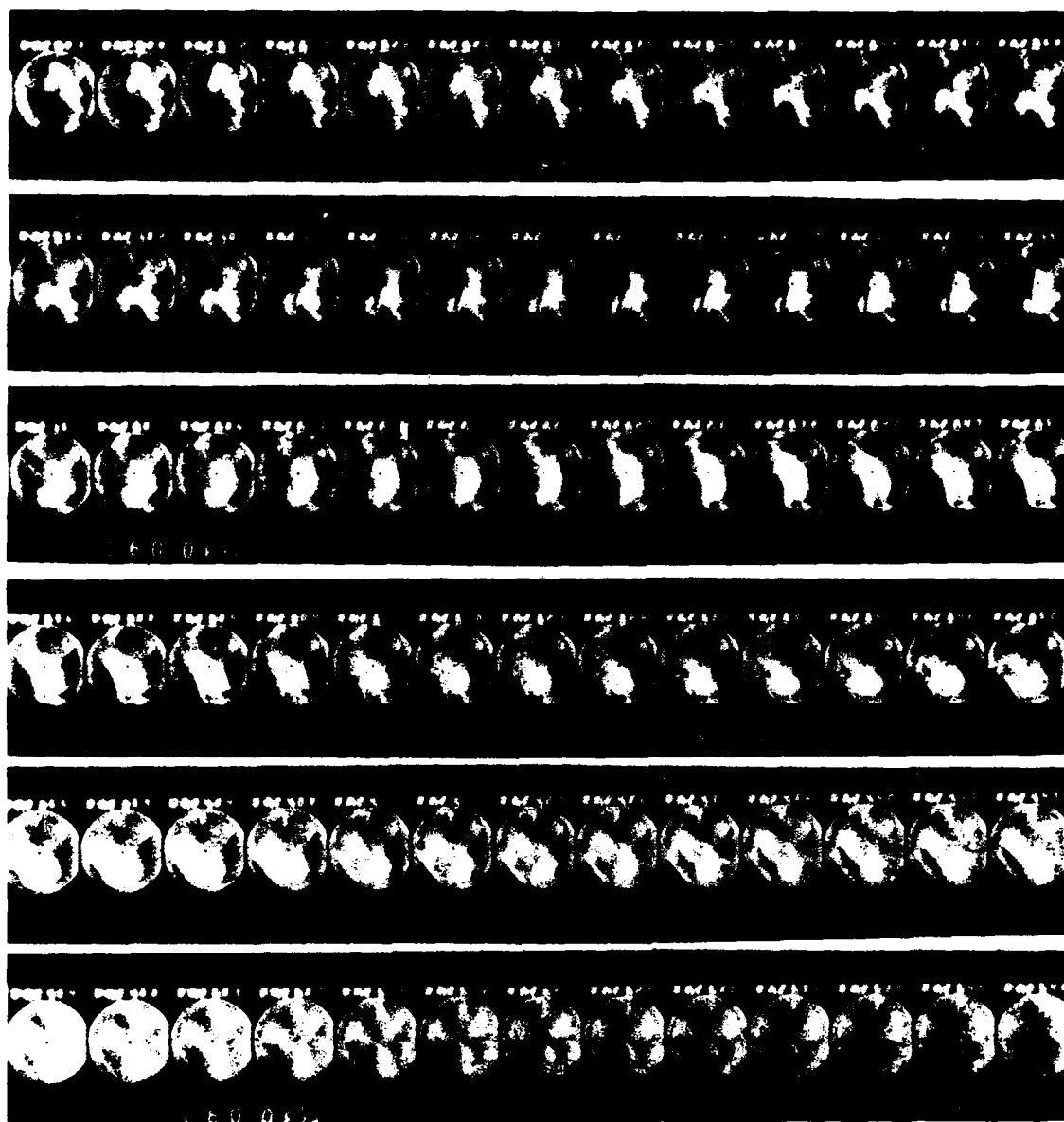


Figure 8d. All-sky montages of the auroral energy input distribution before and during data segment 4.

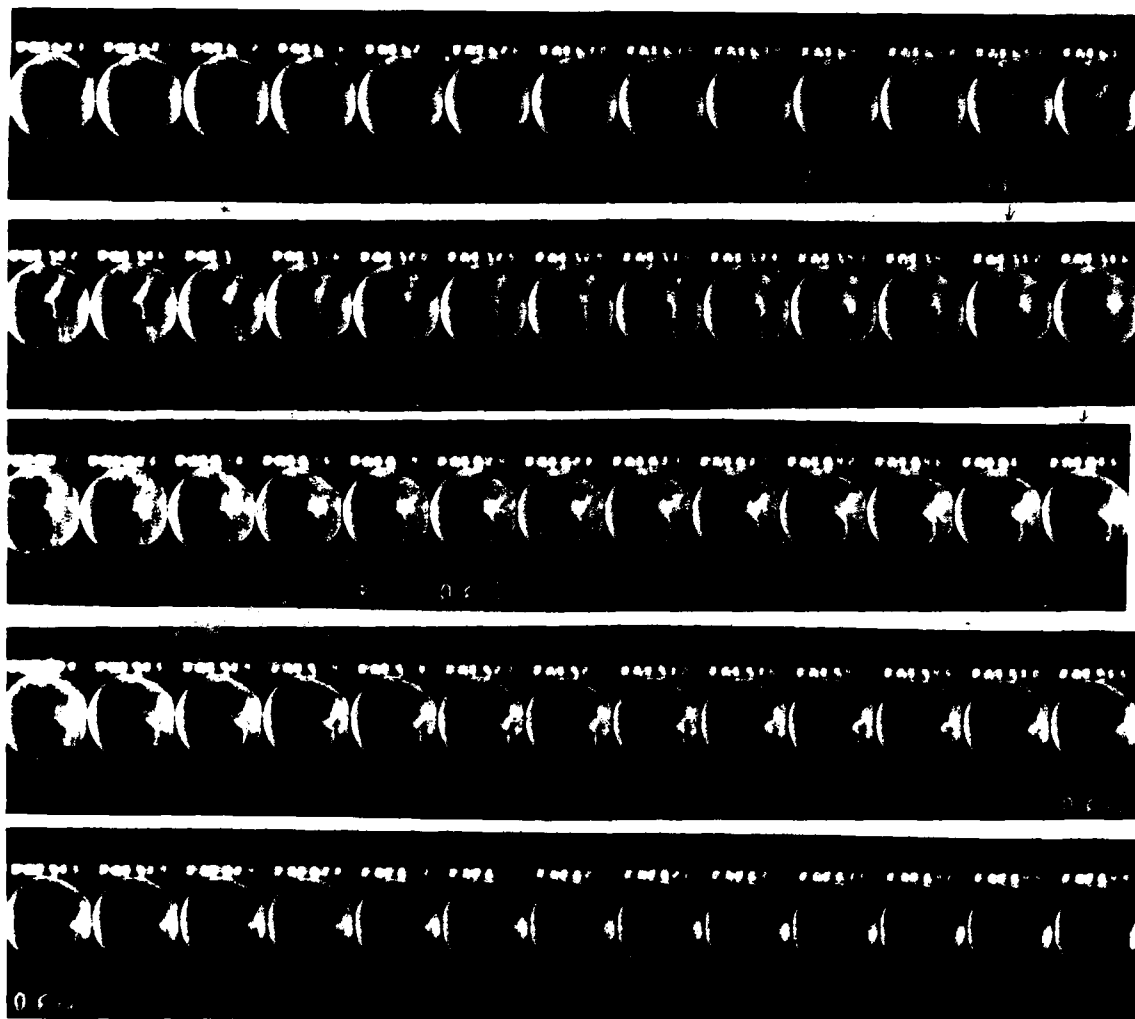


Figure 8e. All-sky montages of the auroral energy input distribution before and during data segment 5.

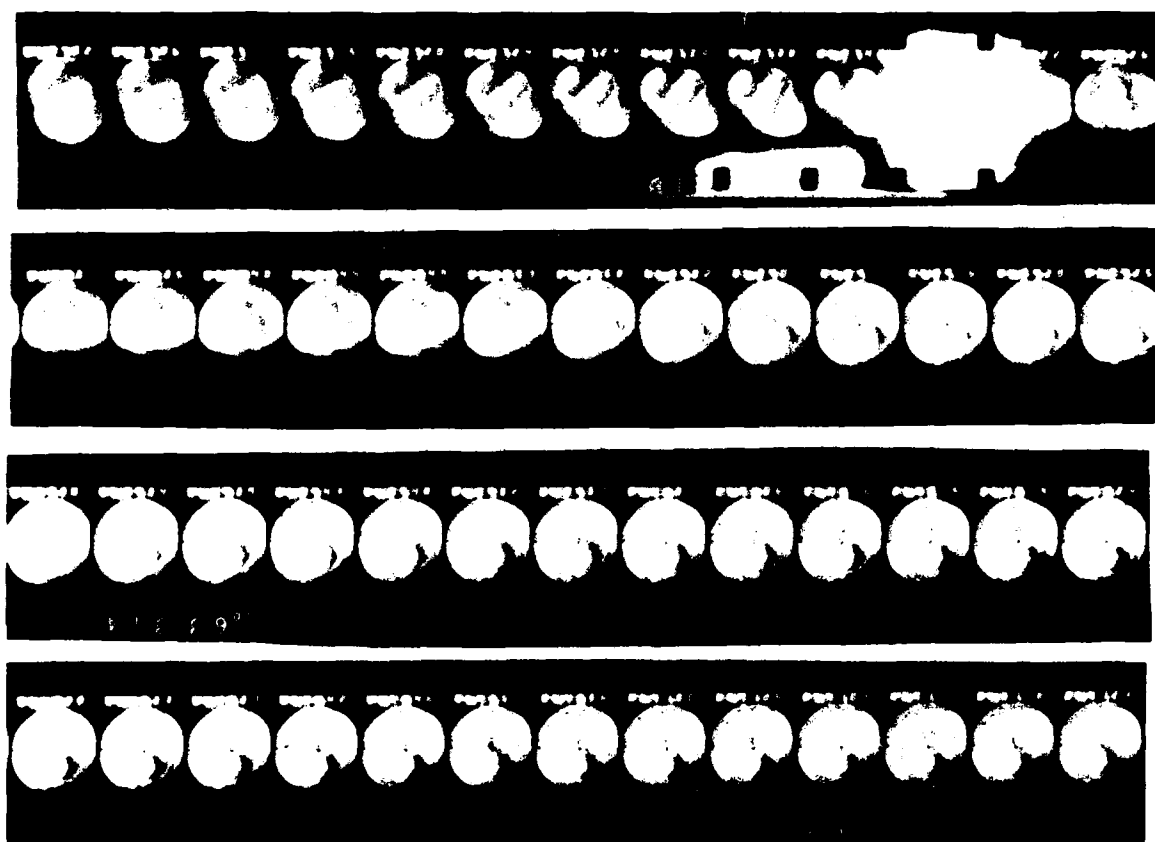


Figure 8f. All-sky montages of the auroral energy input distribution before and during data segment 6.



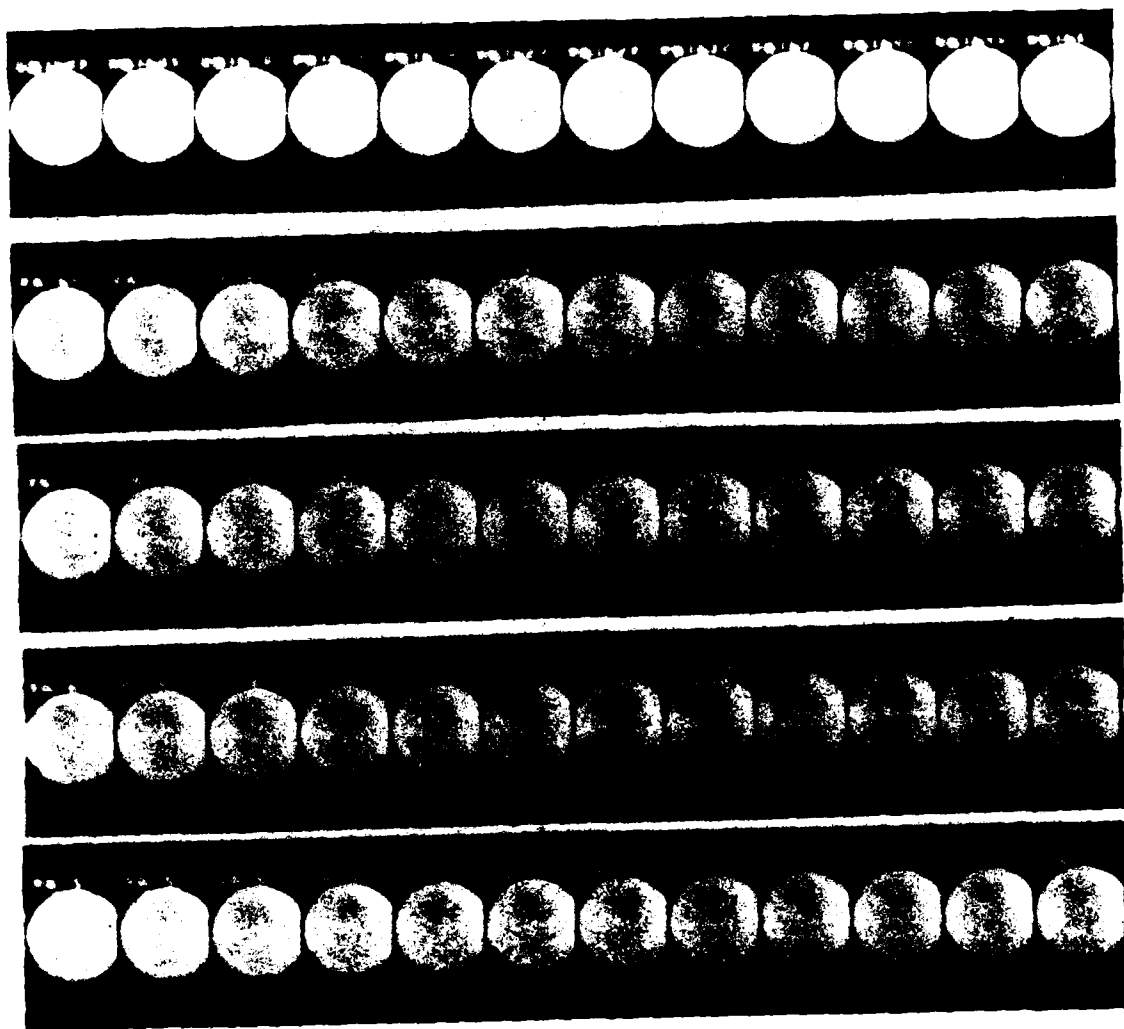


Figure 8g. All-sky montages of the auroral energy input distribution before and during data segment 7.

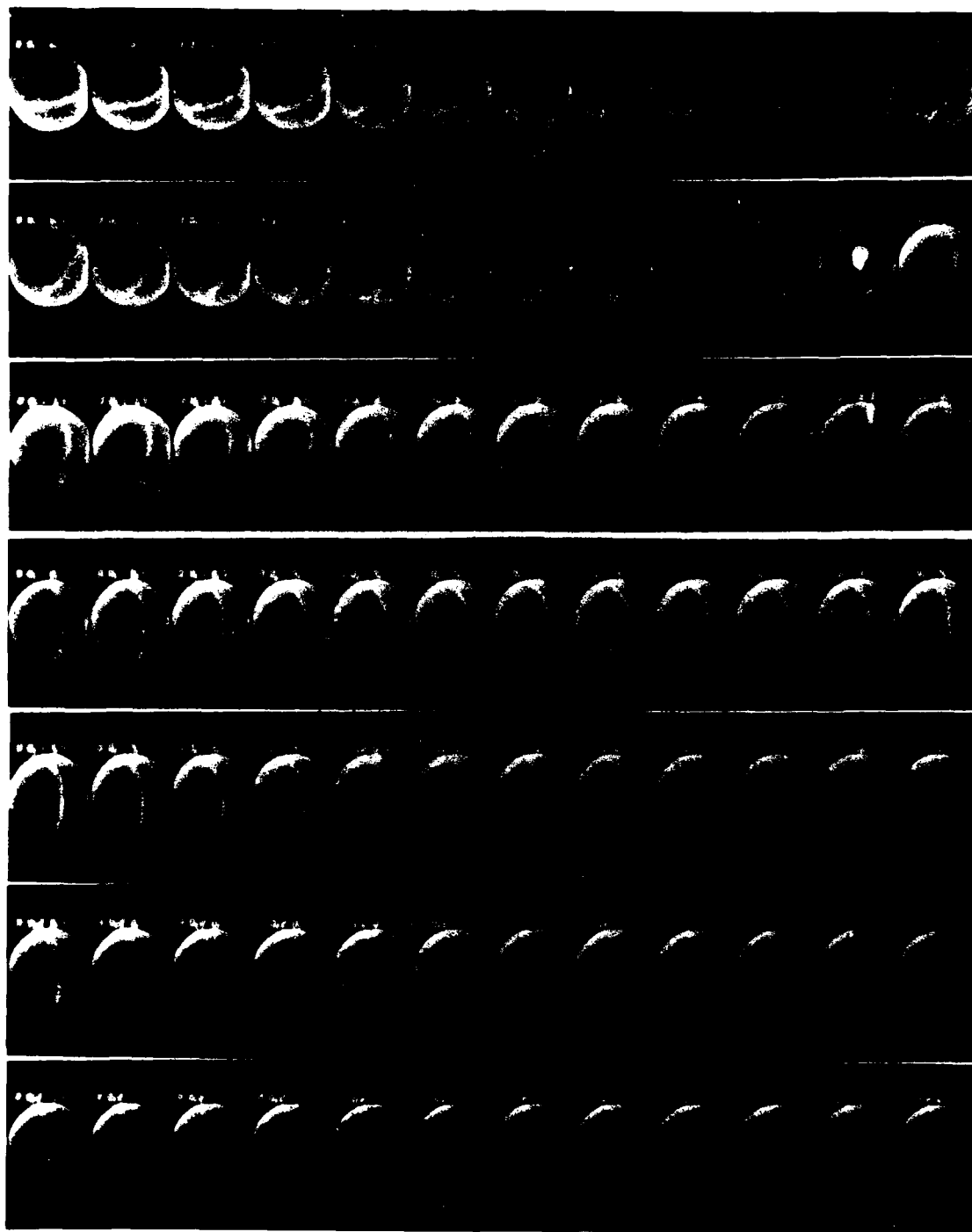


Figure 8h. All-sky montages of the auroral energy input distribution before and during data segment 8.

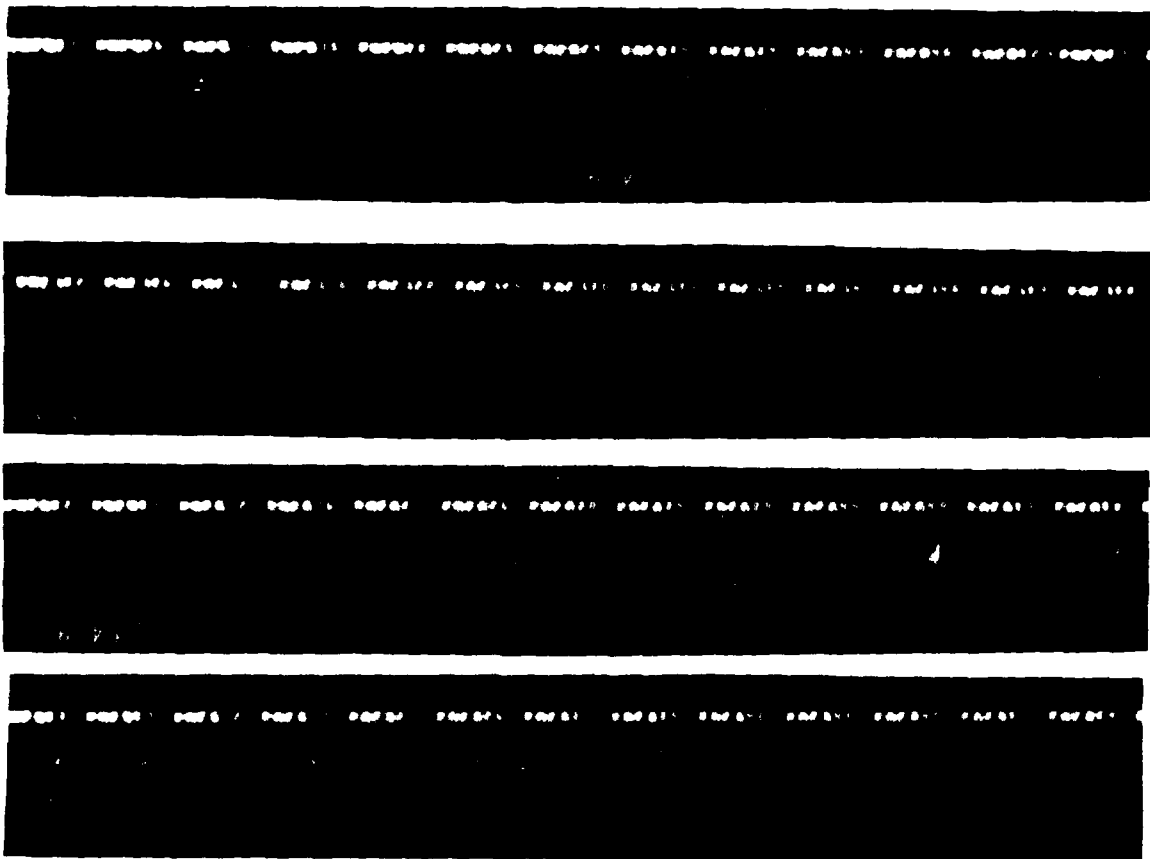


Figure 8j. All-sky montages of the auroral energy input distribution before and during data segment 9.

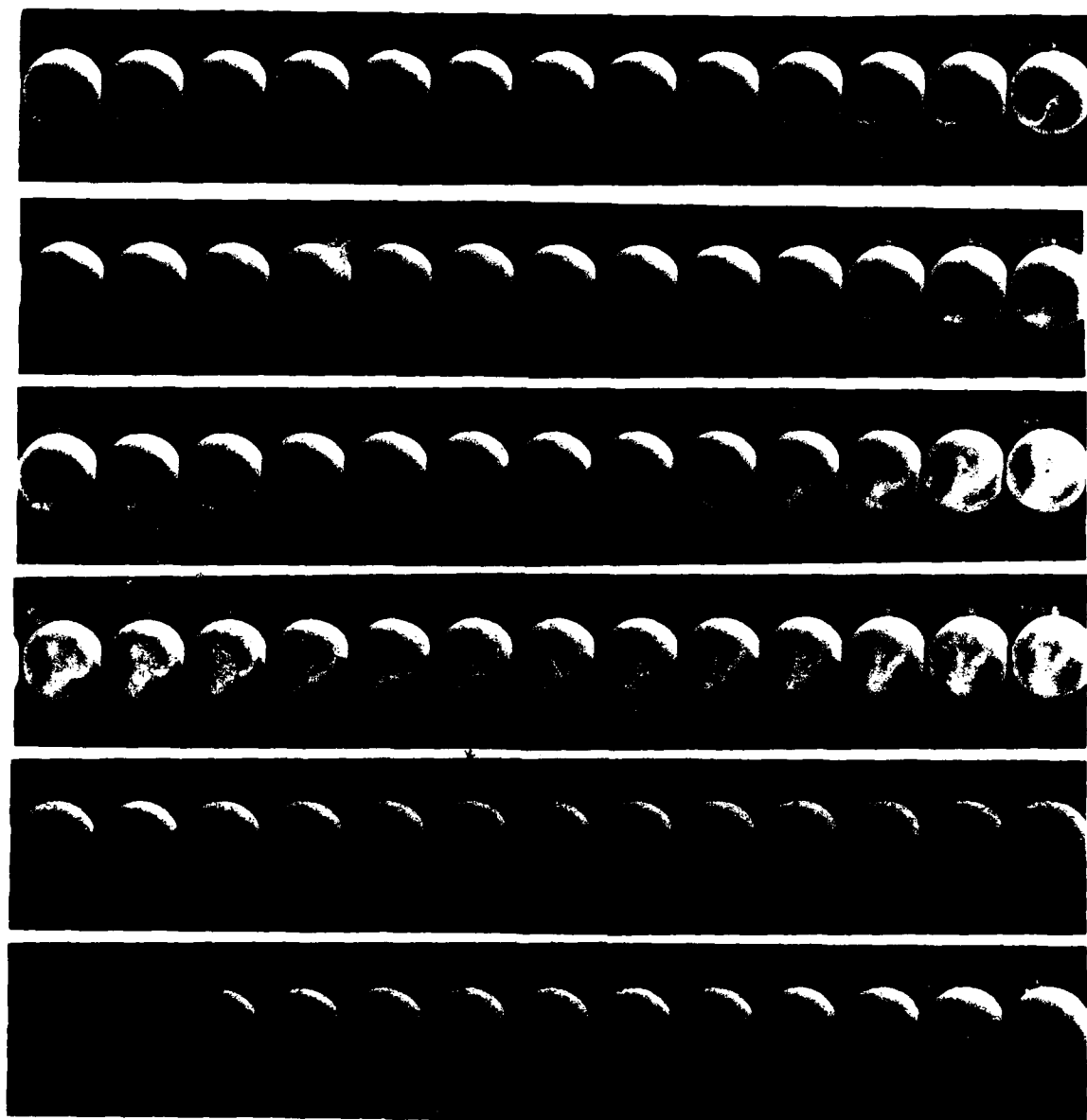


Figure 8j. All-sky montages of the auroral energy input distribution before and during data segment 11.

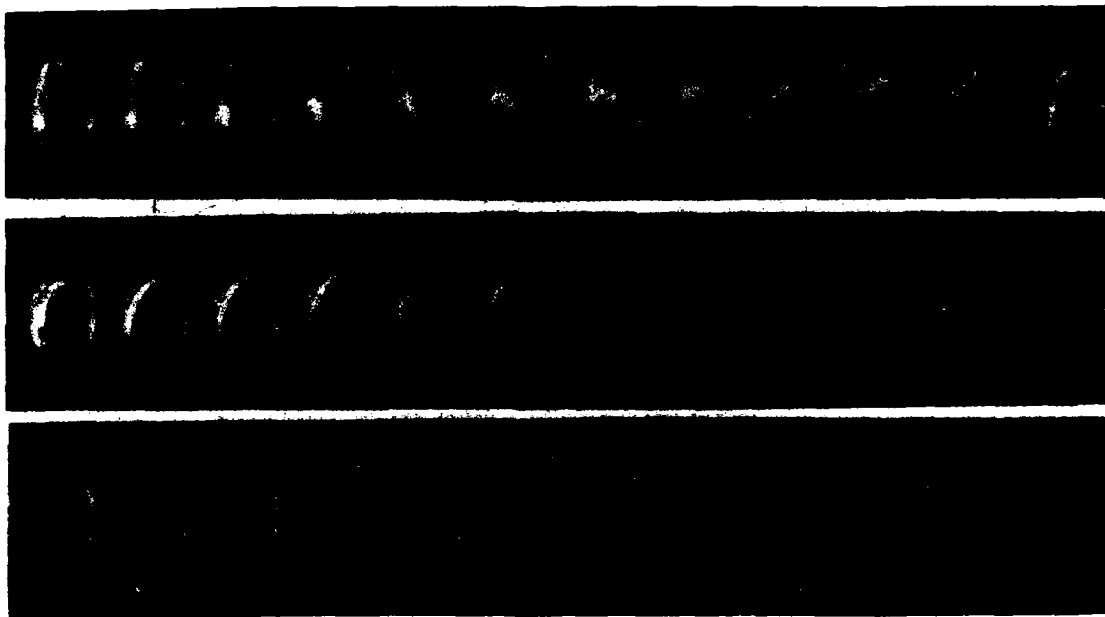


Figure 8k. All-sky montages of the auroral energy input distribution before and during data segment 12.

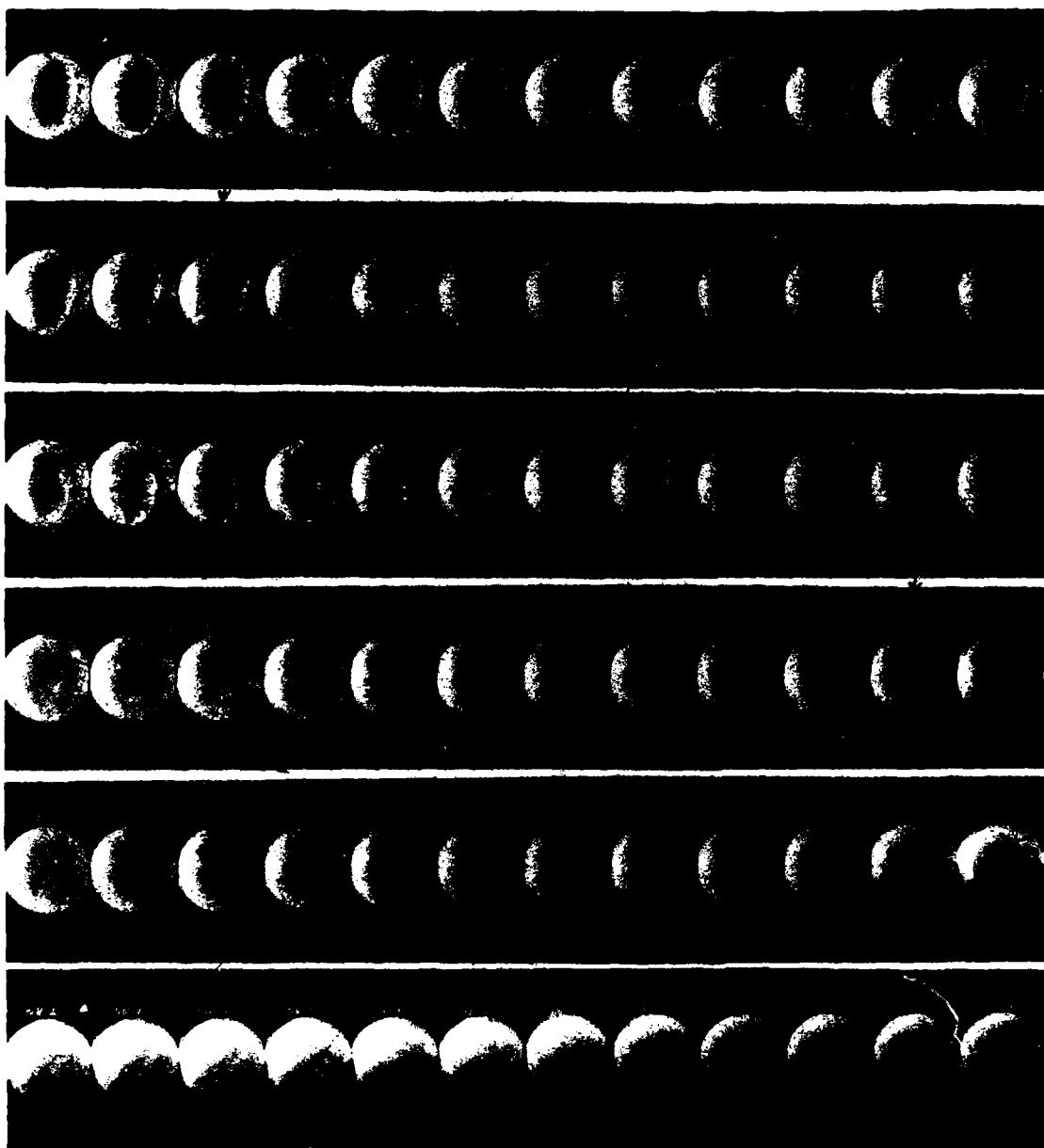


Figure 82. All-sky montages of the auroral energy input distribution before and during data segment 13.

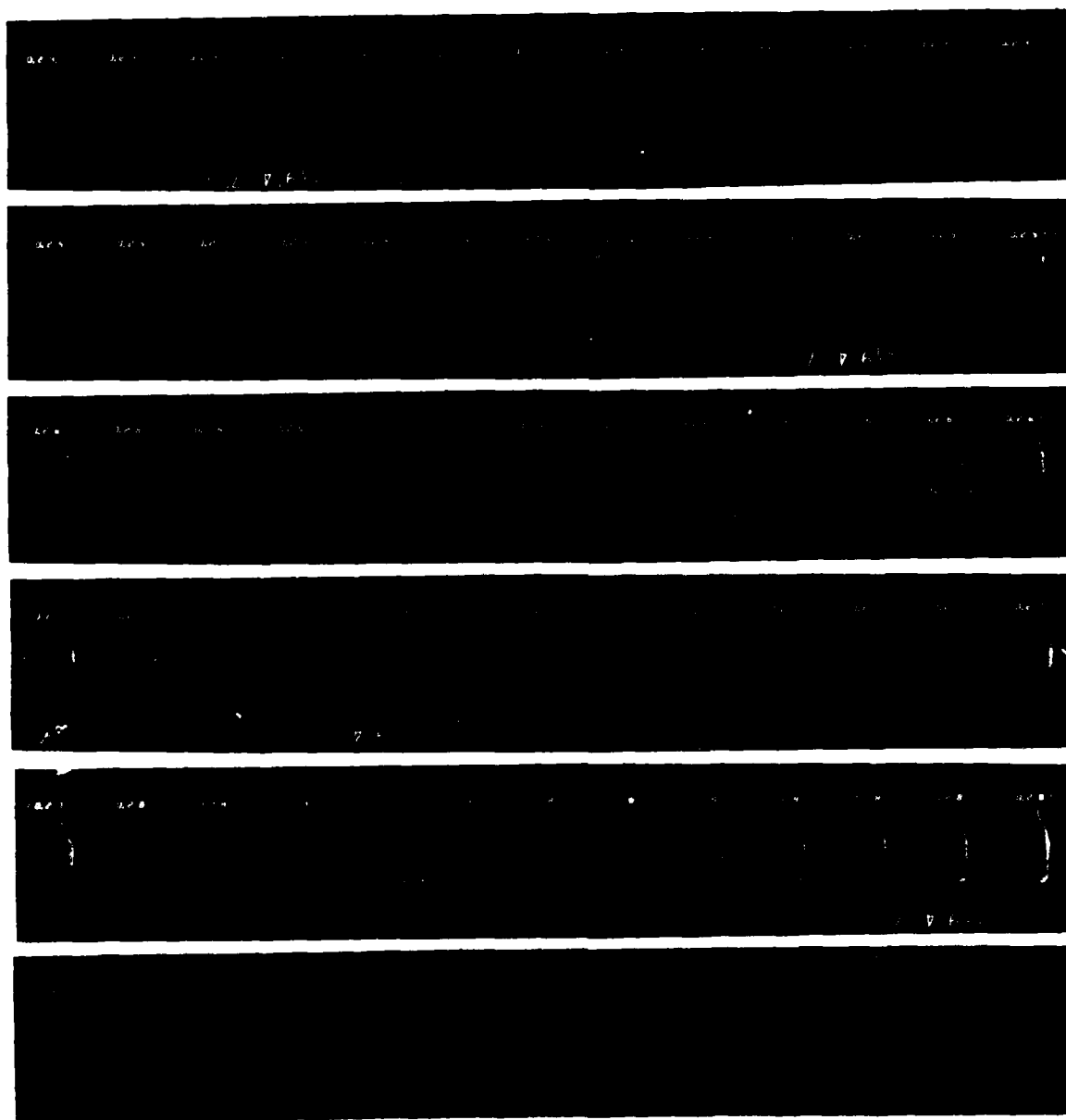


Figure 8m. All-sky montages of the auroral energy input distribution before and during data segment 14.

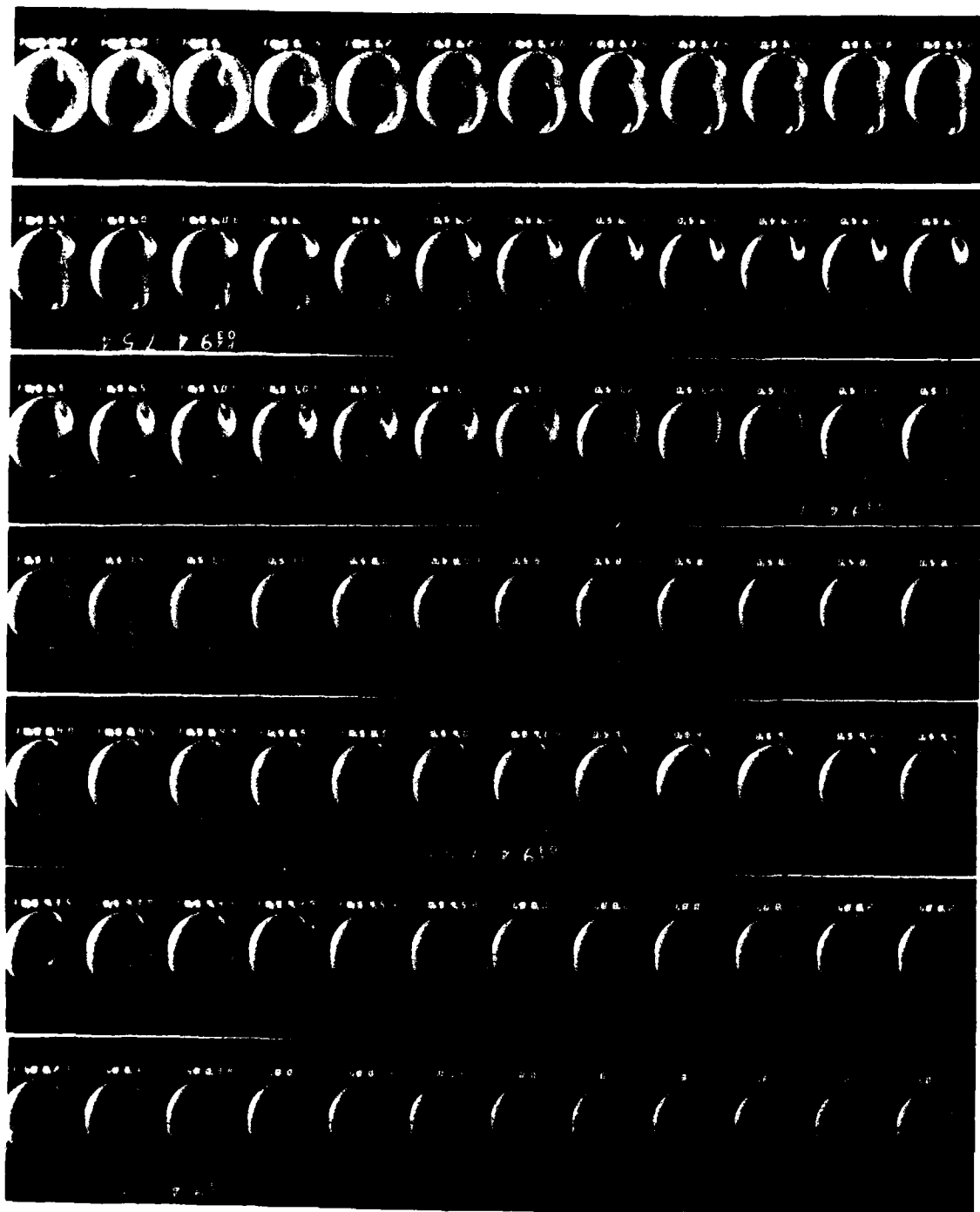


Figure 8n. All-sky montages of the auroral energy input distribution before and during data segment 15 (1 of 3 pages).



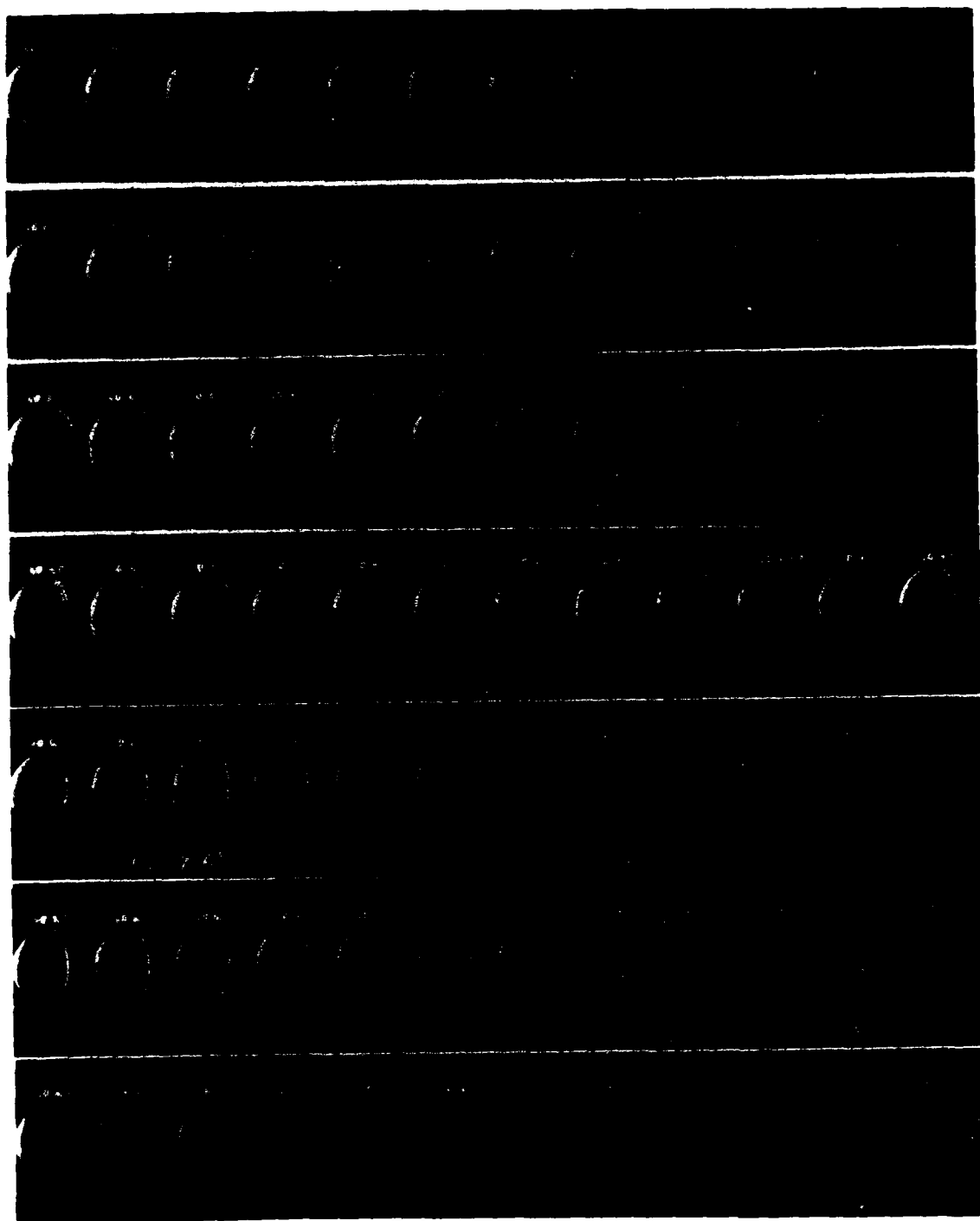


Figure 8n (continued). All-sky montages of the auroral energy input distribution before and during data segment 15 (2 of 3 pages).

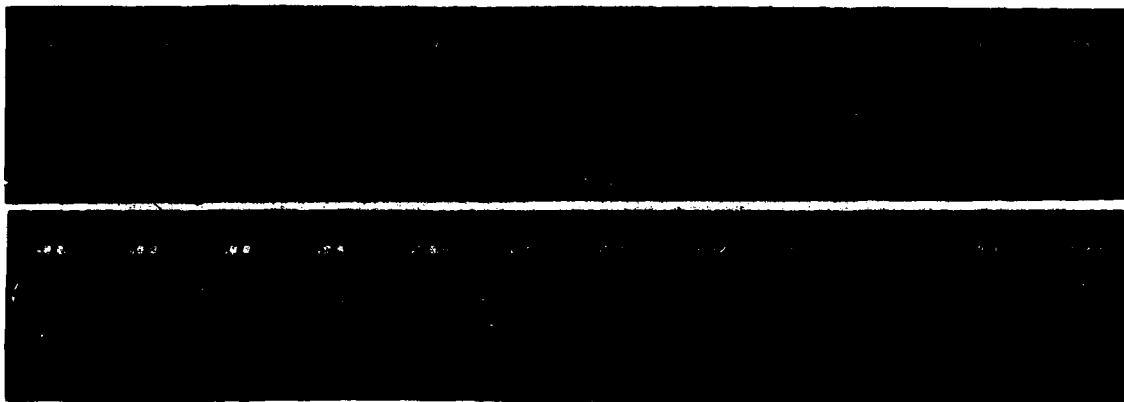


Figure 8n (concluded). All-sky montages of the auroral energy input distribution before and during data segment 15 (3 of 3 pages).

The elevation angle of the center of the solar disk at the aircraft and at the latitude and longitude of the 120-km altitude instrument intercept -- the directly applicable figure -- follows the solar declination (which has been tabulated because it is an input to the program for calculating solar elevation). Symbols D and I indicate decreasing (evening twilight) or increasing (morning twilight) elevation, to indicate whether the region of atmosphere on which the optical measurements are made had been sunlight-"predosed." The column following is the hard earth's shadow height at the  $13^\circ$  zenith angle intercept (as defined in Fig 27 of Ref 1 ). The tangent altitude at which the (1966 U.S. Standard)atmosphere transmits half the incident solar ultraviolet radiation is 34 km at 3400 Å, 45 km at 3050 Å, and 70 km at 2380 Å; the minimum auroral altitude reached by half the photons at these UV wavelengths can be found with adequate accuracy by adding these "screening" heights to the illuminated heights listed in Table 4 .

Column intensity ratios of visible-aurora features at the times in the data segment when energy input rate is a maximum, are listed in the next column. These are followed by the altitudes of peak energy deposition at these more or less characteristic times, calculated from the 6300 Å/4278 Å ratio and 4278 Å intensity. These altitudes refer to the aircraft's zenith in Flights 908 and 909 only, after which the field of view of the wavelength-cycling photometer was directed  $13^\circ$  forward.

The final two columns list the three-hour local (K) and global (Kp) magnetic indexes at the times of the flight segments. Local K's refer to the College, AK sector and thus may not be directly applicable to the 1979 flights, which were  $80^\circ$  in longitude east of College.

The fractional solar illumination of each energy-deposition column, which is listed in Table 5, was determined as follows. We first assigned an "input" altitude profile based on the peak-deposition altitudes, following the procedure in Ref 26. This altitude distribution was taken as remaining fixed for the typically 2-min duration of the SWIR-measurement interval. (For Segments 15a and b, an average peak

Table 5. Fractional illumination of the altitude profile of energy deposition in the 15 data segments. Values refer to the "hard earth" definition of solar illuminated height, as given in Fig 27 of Ref 1.

% SUNLIT -- HARD EARTH DEFINITION

CASE #	% SUNLIT	
1	0	{ NIGHT AURORA
6	0	
9	0	
4	65	
15a	68	
15b	45	
3	53	
14	15	
5	47	
11	100	
7	100	
13	100	
12	100	
8	100	
2	100	

altitude somewhat higher than that listed in Table 5 was used.) We then estimated the fraction of the energy deposition lying above the shadow height from ratio of areas under the profile curve. Six segments are identified as being essentially totally sunlit (3 each from the 1979 and 1980 series), six further are partially illuminated (again 3 from each year), and the remaining three are nighttime aurora. Reference is made to the fact that the entries in Table 5 do not consider outscattering of solar photons by the lower atmosphere; as noted, scattering results in lower fractional illumination by ultraviolet photons.

#### DATA ANALYSIS

The aircraft traverses the projection of the instrument fields at the altitudes where incoming particles deposit energy in about 4 sec, and the integration time needed to achieve adequate SWIR signal/noise is somewhat less. If the time required for aerochemical reactions to excite SWIR radiation is less than or comparable to 4 sec, or under conditions that production and loss rates have reached equilibrium in the atmospheric volume probed, the cross-plot method that we applied to the wide-field data (Ref 1) is a valid means for determining average SWIR-chemiluminous yields. We therefore made cross-plots of the simultaneously measured "input" and "output" radiances, reading the traces at 5-sec intervals in cases where the duration of enhancement was several min and  $\frac{1}{2}$  to 1 sec when it was  $\sim 1$  min (Segment 12, for example). Limited manual smoothing was applied, to minimize bias against short-period fluctuations while ensuring that noise spikes are suppressed. As the contribution to the SWIR signal from OH airglow remains essentially constant over individual data segments, it was not subtracted; this of course does not change the slope of the cross-plots.

Example cross-plots from three data segments representing one day (Segment 12), one night (Segment 1) and one twilight (Segment 3) IBC II+ aurora are in Fig 9. The radiance traces had been filtered in the previous computer merging/calibration of the original samplings, each plotted point being an average of 11 points spaced 0.01 apart. For Segment 12 our sampling interval was 0.4 sec, and for 1 and 3, 1.0 sec.

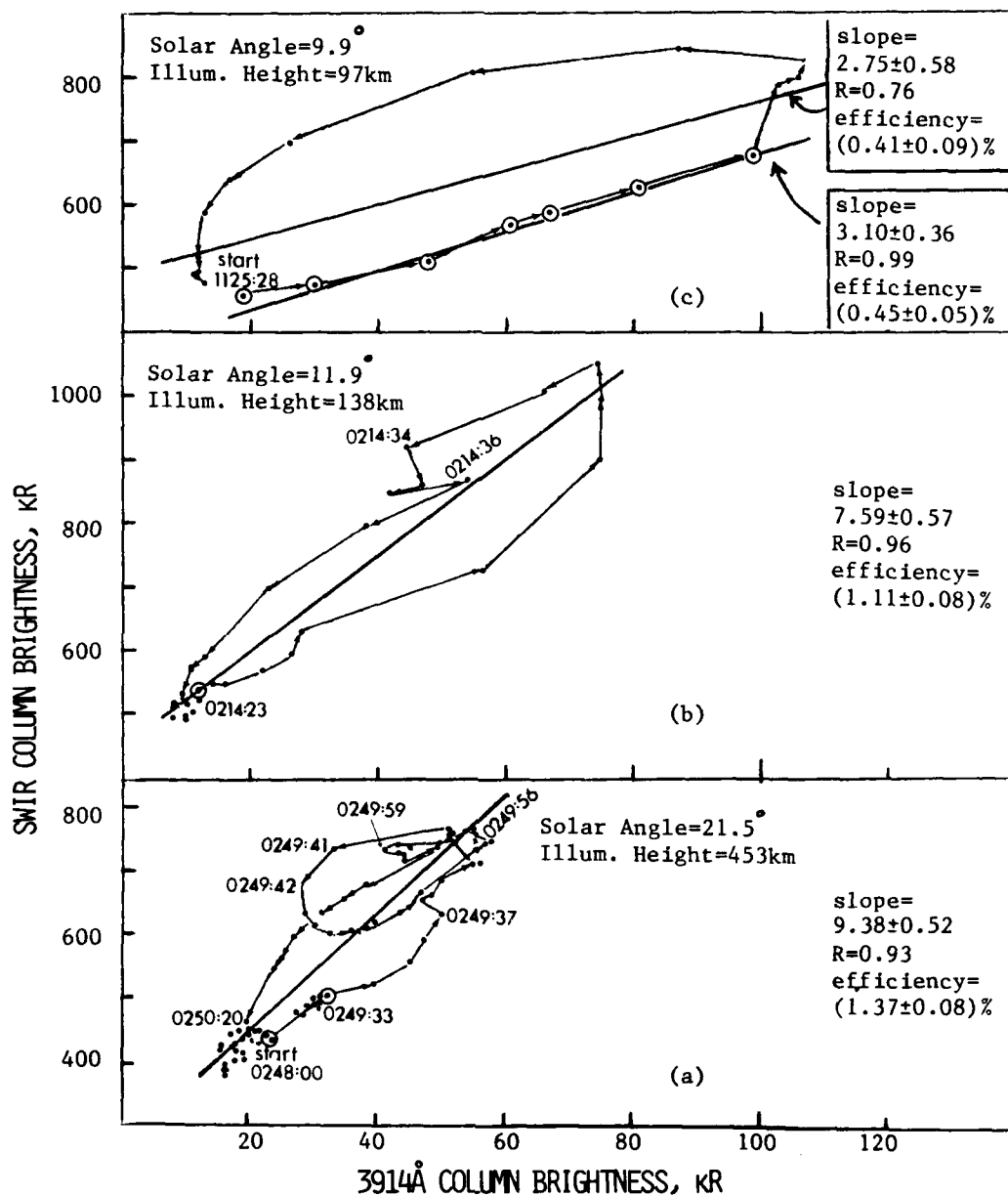


Figure 9. Cross-plots of 2.0 - 3.1  $\mu$ m and 3914 Å-band intensities measured by the narrow-field instruments at three different solar depression angles representing fractional illumination of a) 0% (case 1), b) 53% (case 3), and c) 100% (case 12). The straight lines are uniformly weighted least-squares-fits. Confidence limits refer to 90% statistical certainty of the slopes; R-values are correlation coefficients.

The visible-auroral distributions in all-sky photographs can best be described as a near-uniform arc in Segments 3 and 12, with Segment 1 a non-stationary "breakup."

As reported previously (Ref 1) some of the SWIR enhancements show several-sec longer decay times or offsets of emission peaks from the 3914 Å fluorescence signal (Segment 12 is an extreme example). The "looping" of the cross-plots in Fig 9 is one result of the decorrelation of the two column radiances; for example in segments where the energy input is decreasing the "delayed" instantaneous SWIR radiances lie above the mean regression line, as is particularly evident in Fig 9b and c. This effect appears in both sunlit and nighttime flights, as discussed further below. We have "averaged" the data, also as discussed later, in deriving mean chemiluminous yields.

The straight lines in Fig 9 have been least-squares fitted to the data points, using the procedure and criteria applied to the wide-field instrument data in Ref 21. The R-values represent statistical correlation coefficients, or "goodness of fit" with a straight line, and error given is the 90% confidence limit of the derived line slope. We have again assumed that the uncertainty in the fluorescence intensities in the 3914 Å-band is small compared to that of the SWIR band signal. The assumption of linearity of course does not hold when the fall time of SWIR radiance exceeds that of 3914 Å, as in Fig 9c; note that the seven circled points, which refer to the first 2½ sec of the 8 sec measurement interval when the instrument field first entered a stable arc and the radiances are increasing, do show a high linear correlation when considered separately.

Under the conditions stated above, the slope of the "best fit" straight line can be interpreted as being proportional to the chemiluminous energy efficiency (or yield). In cases such as Fig 9c the fit to all the data points makes a reasonably accurate estimate of the average SWIR yield over the measurement interval since about an equal number of points lie above and below the regression line (the correlation coefficient provides a measure of this accuracy). This assumption is further supported by results of calculations of the ratio of "area" under each SWIR enhancement (in kR-sec) to that under its 3914 Å radiance increase, which show the time-integrated photon emission rate ratios to be in agreement with

the best-fit slopes (within the limits of the precision of the data). This second method for determining yield requires subtraction of the OH-fundamental airglow from the SWIR radiances. This airglow intensity was assessed by interpolation of the background on either side of (before and after) the aurora-associated enhancement. The uncertainties in slope listed on Fig 9 refer only to 90% statistical confidence limits, and do not reflect other potential systematic and erratic sources of error due to calibrations, instrument instability, window frost, and similar factors.

Following the procedure that we applied in Ref 21, and taking 0.42 as the fraction of NO  $\Delta v = 2$  sequence within the radiometer's bandpass (using the COCHISE population model), we determined chemiluminous yields from the slopes of each of the 15 segments' cross-plots. (In three cases the "area" method was used, as identified.) The results, listed in order of increasing solar depression angle, are shown in Table 6 .

The column labeled PhM delay in Table 6 gives a semi-quantitative measure of the delay between SWIR output and energy input, which we determined by visually comparing offsets of emission peaks and lags in decay time between the two data traces. The estimation method was checked by applying it to the 5577 Å (OI  $^1S - ^1D$ ) and 3914 Å photometer signals; the lag of the metastable oxygen emission was less than 1 sec in all cases, which is larger than its expected value of  $\sim \frac{1}{2}$  sec (Ref 13). A mean characteristic filtering time, which refers to both the rise and fall of the SWIR signal and which is derived (by M. Bruce of AFGL) from Fourier transforms of the individual data streams, is given under the heading MB LAG. Note that this time is not the lag derived from cross-correlation of the two data sets, discussed in Appendix I of Ref 21; rather, it is the width of the low-pass temporal filter that "fits" the SWIR output to the input's frequency-space components. The final evaluation of the aircraft data will apply cross-correlation and delay-weighting methods to quantify the induction time of chemiluminescence.

Data quality (based on signal/noise of the SWIR radiance) is given in the next column; the times in parentheses are the lengths of the enhancement segments. Fuselage pointing and altitude of peak energy deposition are then repeated from Table 4 to permit a rapid comparison between yield and lag and these measurements parameters. "Averages" shown for some segments refer to peak emission altitude averaged over the measure-



Table 6. Chemiluminous yields and apparent SWIR delays, with deposition altitude and aircraft heading from Table 4. The data segments are listed in order of increasing solar depression angle.

SOLAR DEP ANGLE (deg)	AVE. EFF., %	DELAY, SEC	MB LAG (SEC)	DATA QUALITY -S/N-	FUSELAGE POINTING	PEAK AURORAL ALT, KM	
Case							AVE *
11) 8.8	1.36±0.13 R=0.97	0	0.2	FAIR-GD (350sec)	W(Ferry)	116	
7 ) 9.3	0.70±0.09 R=0.87	2-3	1.0	GOOD (180)	NW	160	
13) 9.5	0.92±0.13, R=0.92 (0.8 "area")	5	1.0	GOOD (120)	S	119 +/-2	124
12) 10.0	0.57±0.10 ("area")	5	1.0	GOOD ( 8 )	N	109	
8 ) 10.4	1.04±0.10 R=0.92	0-1	1.0	FAIR-GD (240)	S	130 +/-3	144
2 ) 10.7	1.09±0.30 ("area")	1.5-3	0.8	V.GOOD (150)	N	134	
4 ) 11.6	1.36±0.17 R=0.83	2-6?	0.9	GOOD (210)	N	120	
15) 11.5	1st half 1.1±0.04 R=0.89	3	1.2	GOOD (300)	S	120 +/-5	130
12.3	2nd half 1.2±0.40 R=0.53	2?	1.0	GOOD (240)	S	122 +/-2	127
3 ) 11.9	1.11±0.08 R=0.96	1-2	0.8	GOOD ( 45 )	N	120	
14) 12.5	0.51±0.08 R=0.94	1-2	1.2	GOOD (300)	N	110 +/-2	122
5 ) 12.6	1.09±0.08 R=0.97	3-4	0.8	FAIR-GD (120)	S	128	137
1 ) 21.5	1.37±0.08 R=0.93	2-4	1.0	GOOD (140)	NE	120	
6 ) 23	0.80±0.07 R=0.88	0-1	0.7	GOOD (180)	N	120	
9 ) 30.4	1.30±0.21 R=0.94	0-1	1.0	GOOD ( 80 )	N	145	

\* Averaged over entire data segment.

ment period; note that these are higher than the altitudes at maximum enhancement, as the spectral index (or hardness) of the precipitating particles tends to decrease as their total flux decreases.

The efficiencies listed in Table 6 show a statistically significant variability of more than a factor 2 over the 18 month measurement period, among individual flights of the three series, and even within single flights (for example, Segments 14 and 15a-b, Flight 027). A comparably large variation was present in the yields measured by the wide-field instruments in 1975-78 (Ref 1), whose average was found to be about  $\frac{1}{2}\%$ . With the narrow-field instruments the mean energy yield in SWIR-band radiation in particle-irradiated, auroral altitude air is closer to 1%, and in some cases this yield reaches 1.4%.

The "lag" between SWIR radiation output and energy input, as estimated from offsets between emission peaks and delays in the SWIR signal's return to baseline after the excitation has essentially disappeared, also varies, showing values between zero and 6 sec. (The Fourier-components ratio calculation shows filtering time constants that cluster closely around 1 sec.) It is instructive to note that no negative lags are identified by either method.

#### CORRELATION WITH AURORAL AND MEASUREMENT PARAMETERS

To identify probable sources of this variability in both mean yield and lag time of SWIR emission, we cross-plotted results against auroral and measurement parameters (Fig's 10 and 11). The circled numbers in the plots identify the data segments.

Fig 10a shows no apparent correlation of yield with incoming flux, which is not unexpected because the original input-output cross-plots are closely linear. Results from the earlier wide-field instruments support this finding. Figure 10b indicates that SWIR yield is also independent of fractional auroral illumination; i.e., no day-night effect is found. No correlation is found with global magnetic activity index, or altitude of the aircraft (not shown), on which could depend effects of window frosting, atmospheric attenuation and cirrus (or unexpected aspects of instrument performance).

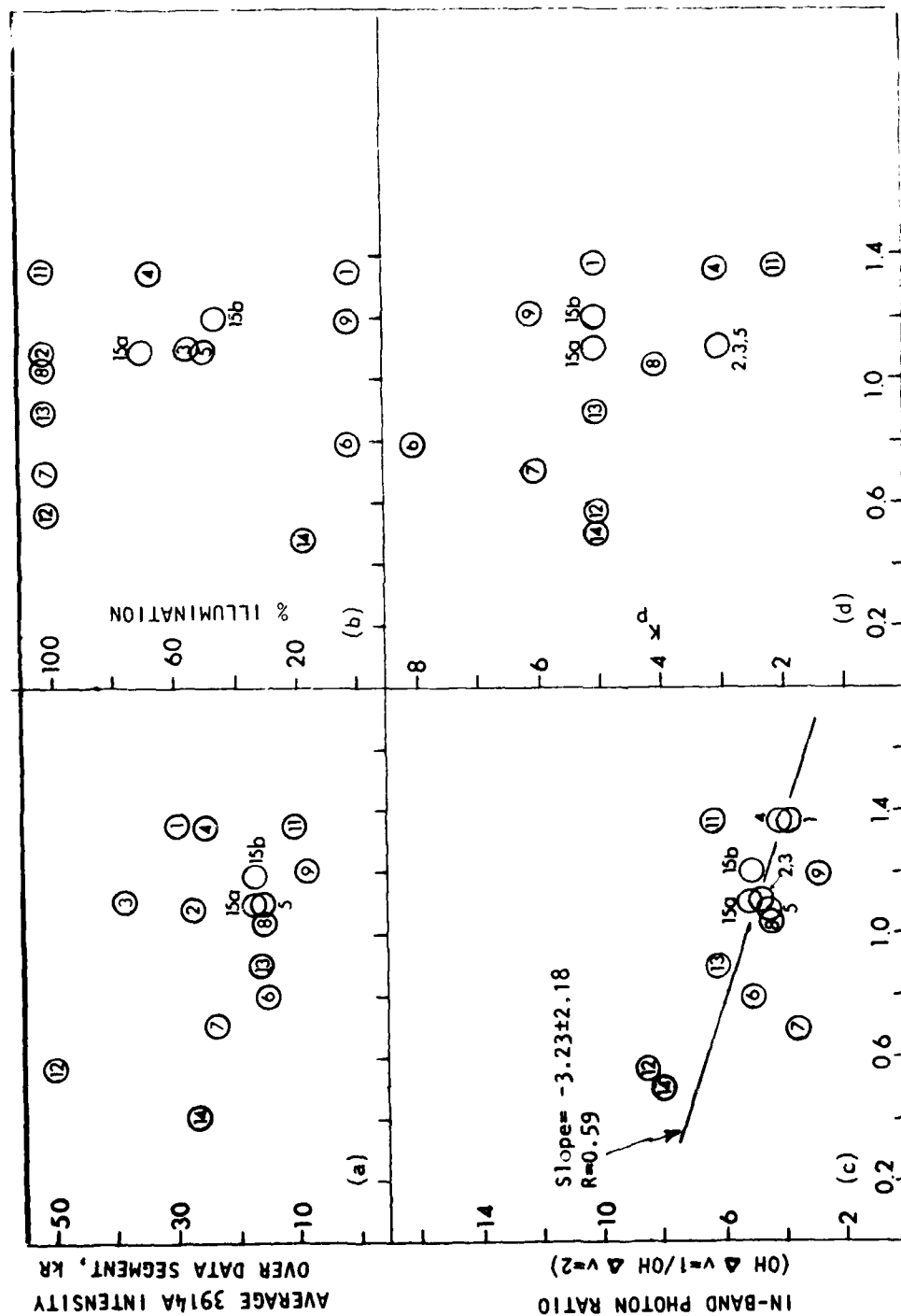


Figure 10a-d. Average NO vibrational overtone yield in data segments cross plotted against  
a) average 3914 A-band intensity, b) fractional solar illumination of the  
aurora, c) hydroxyl fundamental/overtone ratio, d) global magnetic index.  
Characteristics of the 15 data segments are in Table 4.

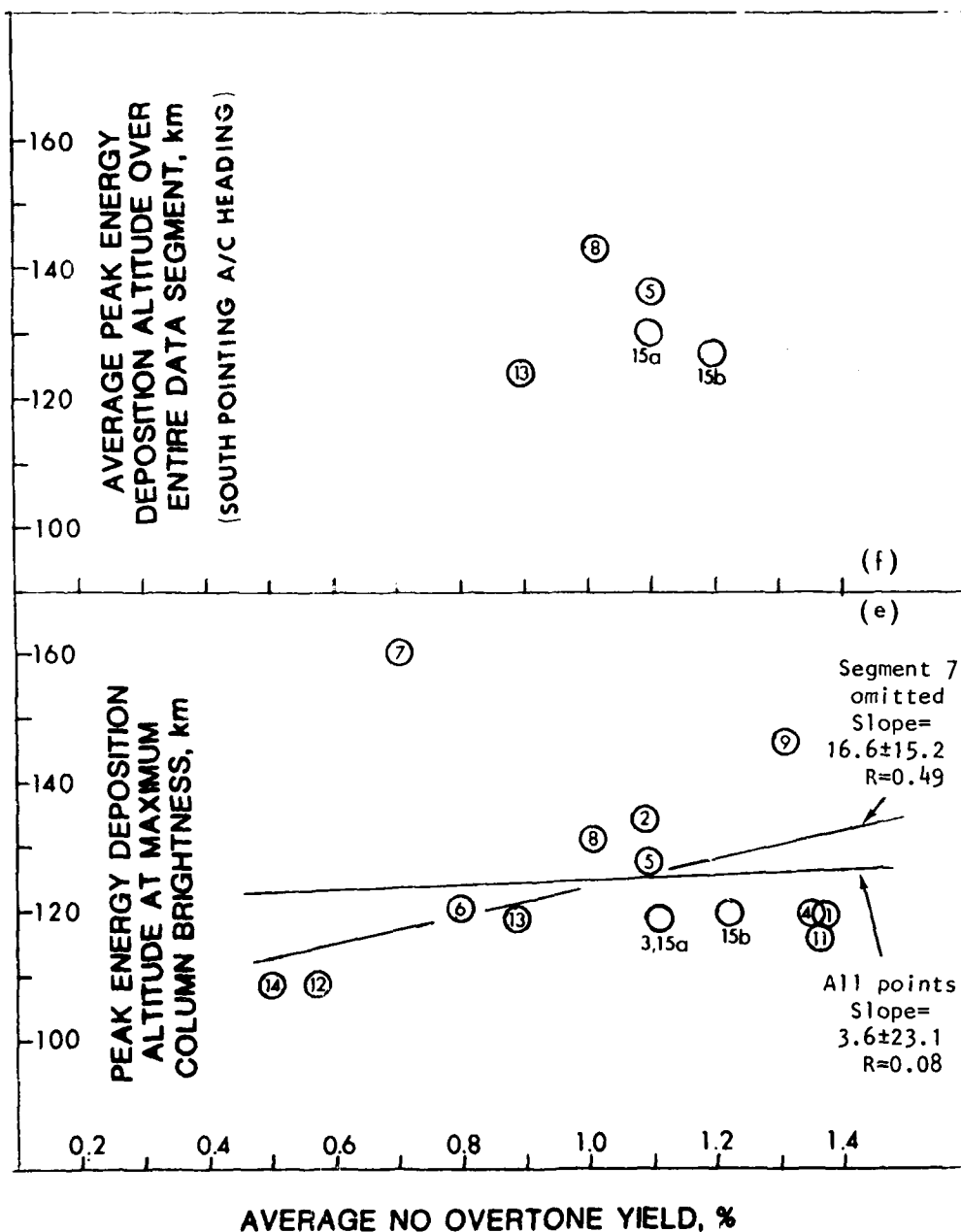


Figure 10e-f. Average NO overtone yield plotted against altitude of energy deposition. (e) All segments, at maximum deposition rate; (f) south-pointing segments, averaged over deposition rates.

Some evidence for a trend with the ratio of intensities in the hydroxyl fundamental and overtone nightglow is in Fig 10c; however the negative slope ( $-3.23 \pm 2.2 \Delta v = 1/\Delta v = 2$  (in photons) per 1% change in absolute SWIR yield) is opposite to what might reasonably be expected. Variable sensitivity of the SWIR radiometer would drive both this hydroxyl-bands ratio and the apparent aurora-associated yield in the same direction; and cirrus clouds above the aircraft increase the apparent ratio (excess thermal radiation being mistaken for airglow) without greatly impacting the yield (increased outscattering of shorter wavelength photons compensating the increased attenuation of SWIR radiation from the aurora). In any case, Fig 10c has too low a correlation coefficient and statistical precision for a compelling argument supporting the anti-correlation (note that the trend line is significantly "weighted" by two data points, from Segments 12 and 14).

Fig 10e may be interpreted as suggesting a correlation between average SWIR yield and the altitude of peak energy deposition by the incoming electrons. The altitudes in Fig 10e refer only to that section of each data segment at which the 3914 Å column brightness (i.e., incoming particle flux) was a maximum. For the five cases in which the aircraft was heading magnetic south (Fig 10f), peak energy deposition altitudes were averaged over the full measurement interval. The slope of the regression line fit to all data points is 3.6, which would be an increase in NO overtone efficiency of about 0.28%/km altitude; the low correlation coefficient, 0.08, indicates a very poor linear fit, and furthermore the 90% confidence limits on the slope are very broad. If Segment 7 is omitted, the slope increases to 16.8 (0.06%/km altitude)  $R = 0.49$ . For both sample sets, the large statistical uncertainty indicates that the slope of the best fit line could result in SWIR efficiency increases as low as  $\pm 0.03\%$ /km of peak energy deposition altitude.

To investigate further this apparent increase in SWIR yield with deposition altitude, "instantaneous" efficiencies and altitudes were

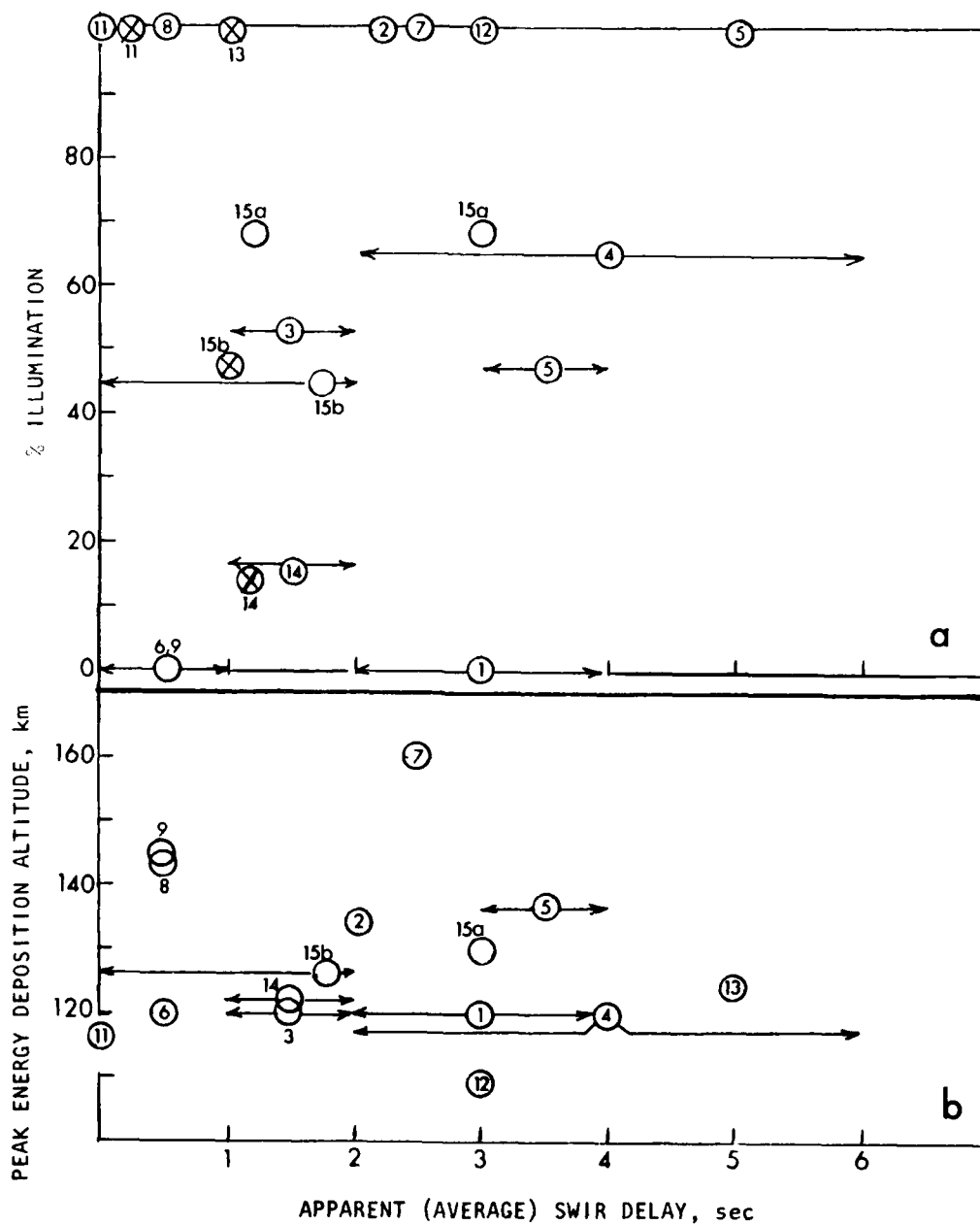


Figure 11. Visually-determined SWIR delay cross-plotted against  
a) fractional auroral illumination and b) peak energy  
deposition altitude. Points marked (x) are from column  
marked MB LAG in Table 6; refer to text for explanation.

Table 7. Correlation of SWIR enhancement delay with auroral and measurement parameters

	-- PhM DELAY--	
	$\leq 2$ sec	$> 2$ sec
<u>SOLAR DEPRESSION</u>		
< 10°	1	3
10° to 12°	2	2
12° to 14°	1	2
> 14°	2	1
<u>IBC CATEGORY OF AURORA</u>		
I + II	3	6
III + IV	3	2
I + II + III	4	7
IV	2	1
<u>A/C POINTING</u>		
N	1	3
S	4	5
<u>SWIR YIELD</u>		
> 1%	5	2
$\leq 1\%$	2	3
<u>PEAK DEPOSITION ALTITUDE</u>		
< 120 km	2	2
120 km	2	3
> 120 km	2	3
<u>AURORAL FORM</u>		
Isolated Arc (IA)	4	4
Other (O)	2	4
IA North Heading	3	2
IA South Heading	1	1
O North	1	3
O South	0	2
<u>OH (<math>\Delta v = 1</math>) RADIANCE</u>		
$\leq 300$ kR	5	3
$> 300$ kR	2	5
<u>Kp</u>		
1 - 4	3	3
5 - 8	4	5

measured at 5 sec intervals for the  $3\frac{1}{2}$  min of Segment 13, during which a temporally-uniform (sunlit) auroral arc was traversed by instrument fields pointing in the direction of the geomagnetic field (Fig 8). This segment represents one type of optimum data: an isolated, stable (within the 6300 Å line equilibrium criterion) arc viewed long the directions of incoming particle precipitation. The results, which generally support those in Fig 10e, suggest an increase in mean NO overtone yield of about 0.15% per km altitude, with its statistical limits 0.33 and 0.06% per km. This finding of a large variation with altitude does not agree with calculations shown in Fig 12 based on a simple model of NO<sup>+</sup> excitation-deexcitation: quenching of NO(v) by O proportional to v, quenching of N<sup>2</sup>D by O with rate coefficient  $5 \times 10^{-13} \text{ cm}^3/\text{sec}$ , [O] profile as measured from DNA/AFGL rocket IR 807.57-1,  $1\frac{1}{2}$  N<sup>2</sup>D/ion pair at all altitudes (the model is based generally on ideas in Ref 25). These simplified calculations indicate that the vertical column integrated NO overtone yields should increase very slowly with peak energy deposition altitude, roughly 0.002% per km over the 100-140 km altitude range.

We have separated the estimated SWIR lags into two groups, "short" ( $\leq 2$  sec) and "long" ( $> 2$  sec), for comparison with some of those auroral and measurement parameters perceived as potentially impacting the data. Table 7 gives numbers of segments falling into the categories

- solar depression angle (sunlit aurora, partially sunlit, dark);
- IBC intensity of the aurora;
- direction in which the radiometer is pointing (parallel to or at  $26^\circ$  to the magnetic field lines);
- SWIR yield;
- altitude of maximum energy deposition;
- type of auroral form, as determined from the all-sky photographs;



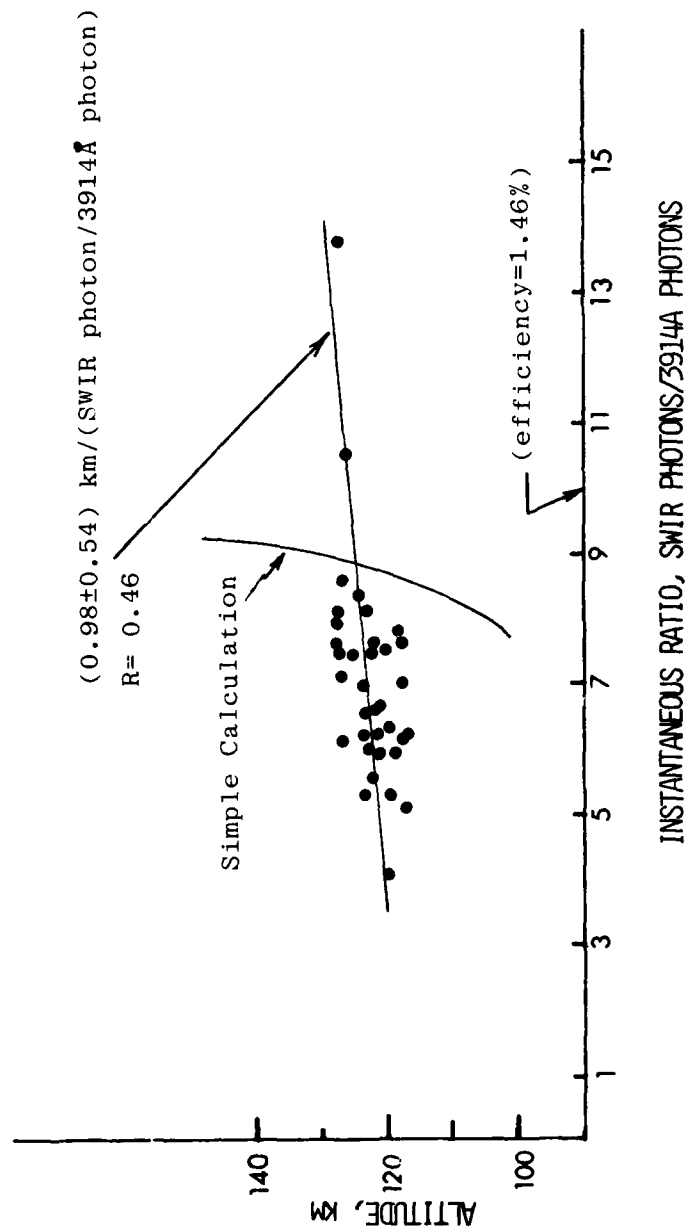


Figure 12. Cross-plot of instantaneous photon ratio against peak altitude of energy depositon in Flight 026 (Segment 13, 1159:30 - 1202:53), compared with results of a simplified calculation of the expected altitude dependence (refer to text).

- form + instrument pointing;
- mission dates;
- zenith radiance in the segment of hydroxyl  
fundamental within the radiometer's wave-  
length sensitivity band; and
- global magnetic activity index Kp.

It is apparent that there is no statistically significant favoring of long or short delays under any of these input-conditions headings, as within the expected statistical fluctuation an equal number of cases is included in each category.

Note in particular the lack of definite correlation of lag with solar depression angle or (more importantly) fractional illumination of aurora. Fig 11, which cross-plots the delays against illumination (and also peak excitation-rate altitude), illustrates this finding: no trend is apparent. Putting the data samples in the quantized format of Table 7, we have

<u>% Sunlit*</u>	<u>-- PhM Delay --</u>	
	<u>≤ 2 sec</u>	<u>&gt; 2 sec</u>
100%	2	4
< 100%, > 0%	3	3
0%	2	1

\* Hard earth shadow height definition; see Table 5.

We may conclude that the data sample is too small to support the hypotheses of a variation in time delay of SWIR radiation (as qualitatively determined) with fractional solar illumination or mean energy deposition altitude. Similarly, the mean yield of SWIR photons in a particle-bombardment event does not correlate with solar illumination, or conversely, a hypothesis of a day-night difference in chemiluminous efficiency is not supported by this set of aircraft-instrument data.

Note that the set of parameters in Table 7 does not address the issue of whether the change in energy input rate within the photometer's field is dominated by the aircraft's motion across temporally-spatially stable particle bombardment or by variability of this bombardment. In stationary auroral forms the SWIR lag would be expected to be lower, as it depends only on transport (diffusion and wind drift) of the intermediate reacting species, as discussed in the Test Plan (Ref 21); This could in fact make the SWIR radiance appear to lead the energy input. The video images of the auroral distribution can be used to answer the question of whether the lag is dominated by chemical or transport effects.

#### SUMMARY AND RECOMMENDATIONS

The set of measurements from subsonic jet aircraft altitude with a sensitive narrow-field radiometer and particle energy input-referencing photometer is a prime source of information on the spatial-temporal correlation between SWIR emission output and ionizing-exciting input into the atmosphere above ~100 km. The auroral 2.8 - 3.1  $\mu\text{m}$  radiances in near-zenith projections measured from AFGL's Flying Optical Laboratory over a period of hours, complement those in earth-limb projections to be measured over a period of minutes from DNA/AFGL's forthcoming ELIAS sounding rocket. Additionally, the only experimental verification that the equilibrium intensity and grow-in decay characteristics of this radiation are the same when the deposition region is sunlit or dark comes from the aircraft measurements.

The principal findings of this evaluation of the "best" segments of the 1979-1980 aircraft data set are that the SWIR radiance follows column energy input to within a few sec (the quantitative temporal/spatial dependence has not yet been extracted from the data), and that the mean energy efficiency of excitation of SWIR emission varies between about 0.6% and 1.3% with no dependence on solar illumination so far detectable. 15 such segments, each representing typically 2 min of measurements on IBC 11 + aurora of various forms, were evaluated systematically. The "equilibrium" chemiluminous SWIR yield shows

statistically-significant variability, with a mean of  $\sim 1\%$  (assuming the auroral radiation enhancements to be the NO overtone, with a spectrum as determined from AFGL laboratory and HIRIS data). This is almost a factor 2 higher than the average determined from aircraft measurements with a coaligned radiometer and photometer having a much wider field. Both sets of data show factor-two variability in yield even among different periods of individual flights in the auroral oval (as well as among flight series), which considering also the lack of correlation with the near-dc zenith sky background from OH vibrational-fundamental radiation, makes it unlikely that this variability is an artifact of the instrument's response or laboratory calibrations.

The data provide some evidence suggesting that SWIR energy efficiencies integrated over the near-vertical measurement column depend on the altitude profile of energy deposition by the precipitating auroral electrons (Fig's 10e and 12). While such an increase with peak disposition altitude might be expected from the increased quenching of  $\text{NO}^+$  by O atoms lower in the atmosphere (refer to the discussion in Ref 1), the trend inferred from the data set and one individual stable arc indicates much more sensitivity to ionization-excitation altitude than is predicted from a simple aerochemical calculation. We recommend 1) that further individual flight data segments be analyzed to check on this important issue, and 2) that runs of more complete computer models of NO excitation and quenching (OPTIR, in particular) be made to improve the assessment of the expected (on the basis of current DNA chemical reaction models) dependence of SWIR yield on the peak (and shape) of the altitude profile of particle energy deposition.

No statistically significant correlation between the SWIR yield and several other auroral and measurements parameters, in particular the fractional solar illumination, is derivable from the segment of data addressed. These parameters do not include the amount of predosing of the sampled region or the temporal-spatial stability of the energy input; as noted (and as further discussed in the Test Plan), the SWIR radiance lag would be lower (and possibly even negative) from aurora

in which an equilibrium between energy input and infrared radiation output is reached. The video camera data contain the necessary information about the time- and space-variation of this input.

The SWIR-emission output is found to lag particle-energy input, with the estimates from visual inspection of the radiance traces showing considerable variation among segments (6 to 0 sec) and no cases of negative delay. We grouped the lag events into two categories,  $> 2$  sec and  $\leq 2$  sec, to investigate correlation with solar depression and fractional illumination, auroral input intensity and peak height, type of auroral input distribution, Kp, and measurement factors such as direction of instrument pointing (parallel to or  $26^\circ$  from the direction of the particle stream) and missions sequence (potentially related to differences in calibration). Cast in this form, the lag data sample addressed do not show statistically-significant dependence on any of these parameters. The effects of predosing and in particular temporal-spatial stability of the particle bombardment (i.e., closeness to "equilibrium"), which would tend to reduce the decorrelation, have not yet been considered; the video camera data contain the necessary input distributions.

Considering that the aircraft-radiometry data represent the sole source of information on the important issue of spatial-temporal correlation of SWIR radiation output with energy input at high (surveillance system-scale) resolution, it is recommended that the complete data set be evaluated and (in particular) that quantitative time delays be derived from the radiance data streams. We recommend also that high altitude air chemistry code runs address specifically the question of grow-in and decay of SWIR radiance in magnetic zenith-oriented columns, to validate the DoD SWIR excitation model against these simulation data from the naturally disturbed atmosphere.

## SECTION 3

### DELAYED VISIBLE EMISSION EXCITED BY PRECEDE

#### INTRODUCTION

We determined the yields of visible radiation after charged-particle energy was deposited at E-region altitudes by DNA/AFGL's "PRECEDE" rocket accelerator (Ref 27 ), by microdensitometric analysis of a photograph of the afterglows. The radiance distribution resulting from a series of 1.0 sec, 0.8 A pulses of  $2\frac{1}{2}$  kV electrons in the previous  $\sim 36$  sec is shown in Figure 13. The persisting self-luminous "puffs" are centered in altitude at the beam-on positions along the vehicle's trajectory (the beam was off for 1.0 sec between pulses). Their horizontal offsets are due to winds, whose velocity perpendicular to the camera's line of sight is as high as 200 m/sec at some of the particle-injection altitudes.

The photograph analyzed was obtained by DNA contractor Technology International Corporation (Bedford, MA) who had responsibility for processing the film and relating its developed density to log relative exposure. Its projection is to the Tiff Optical Site of White Sands Missile Range, which is in the vertical plane of the trajectory at a mean slant range of about 115 km. The frame was exposed for 4 sec and ends during the 73rd accelerator pulse, when the rocket is at 96 km altitude on downleg and moving vertically at just under 0.7 km/sec. Camera focal length was 150 mm and relative aperture f/0.9 in the center of the field of view. Pulses 73 through 61 are reasonably well defined in the reproduction, and the "older," more diffuse glows from still earlier energy input (pulses 60 through 55, 26 to 36 sec before the exposure ends) are resolvable on the original negative.

#### DATA REDUCTION

Peak surface radiances and radiances integrated over the area of



PULSE  
NUMBERS

— 60

— 63

— 65

— 67

— 69

— 71

— 73

Figure 13. Photograph from the Tiff Optical Site, WSMR, of the afterglow resulting from deposition of 1-sec pulsed,  $2\frac{1}{2}$  keV, 0.8 A electrons by PRECEDE. Exposure duration is 4 sec, f/0.9 on EK 2485 film. It begins at 221 sec after launch, when the rocket (bottom of the bright streak containing pulses 71-73) is at 99 km on downleg. The vertical distance between centers of successive resolved "puffs" in the center of the track is about 1 km.

each puff were determined by photographic photometry, the methods being essentially those applied in Section 1. The film was scanned with a  $75\mu\text{m}$ -square microdensitometer slit, which projects to 65 meters at the 115 km mean range of the series of electron ejections. This is about the best spatial resolution allowed by the Eastman Kodak 2485 film's grain noise and the small increase in density of the glow areas over the sky background density (which was 0.26 and thus close to film fog level). The density increment was 0.02 in the initial contour plot made by the two-dimensional scan of the image. We removed stars and smoothed the original film density contours on the basis of our experience with similar calibrated photographs of chemical releases in the upper atmosphere. The existing step tablet calibration was used to assign relative exposures to the contours in each puff.

Figure 14 plots the resulting maximum surface radiances, the minimums between these peaks, and the area-integrated radiances as a function of the time since the atmospheric volume had been initially excited and partially ionized. The data refer to the 4000-6500 Å sensitivity range of the camera. Radiance integrated over puff area, which we measured from the isophote plot using a planimeter, is directly proportional to the total rate of emission at these wavelengths. Note that the maximum brightnesses are comparable to the background due to nightglow (principally, the  $\text{NO}_2^*$  continuum), scattered starlight, zodiacal light, and unresolved weak stars; and that the peaks are of the order of twice the minima (in the regions where puffs overlap). The maximum in peak radiance near 10 sec after the initial disturbance may of course be an effect of the change in energy deposition altitude rather than a result of the grow-in and decay of visible chemiluminescence (the altitude range of the measurements lies at and above the peak in the atmosphere's oxygen atom concentration).

As the density-exposure transfer characteristic of the negative lacked an absolute radiometric reference, a post-calibration was needed for quantitative estimation of the absolute radiances and visible-light



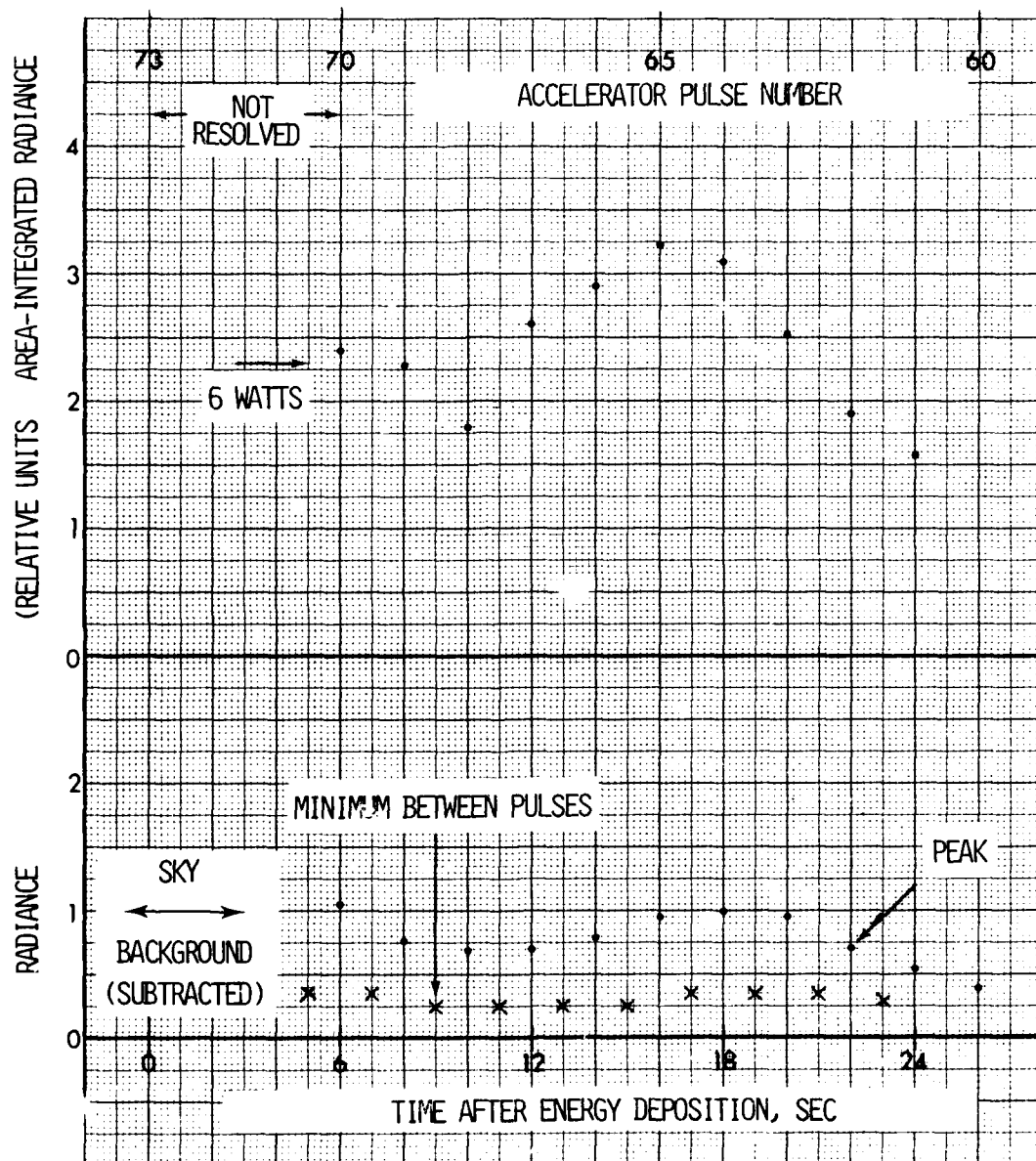


Figure 14. Peak radiance and radiance integrated over area in the PRECED afterglows.

AD-A119 946

PHOTOMETRICS INC WOBURN MA

F/G 4/1

FURTHER EVALUATIONS OF INFRARED SIMULATION DATA.(U)

NOV 81 I L KOFSKY, C A TROWBRIDGE

DNA001-81-C-0003

UNCLASSIFIED

PHM-07-81

DNA-TR-81-81

NL

2 of 2  
4 of 4  
1981

END  
DATE  
FILMED  
11 82  
DTIC

yields from the afterglows. We applied both the nominal mean radiance of the night sky in the film's spectral sensitivity range (Ref 28) and Eastman Kodak data (Ref 29) on its response to derive an absolute exposure at the background density of 0.26. Using the night sky background, an assumed lens transmission of 0.6 (typical for very fast lenses at full aperture), and a  $1\frac{1}{2}$ -stop correction for 2485's reciprocity failure in the 4 sec exposure time (which we had derived from tests in support of earlier chemical release imaging programs), we found that an exposure of  $0.0045 \text{ erg/cm}^2$  would produce this density. The background-producing figure derived from the film manufacturer's data is  $0.0065 \text{ erg/cm}^2$ .

We adopted an absolute-calibration figure of  $0.0055 \text{ erg/cm}^2$  at the sky background, with an estimated error of  $\pm 1\frac{1}{2}$  stops or a factor 2.8. This error is in large part due to the film's low contrast near its threshold (that is, density is increasing very slowly with log exposure). Using this normalization we calculated a total rate of visible light output of 6(-4, +11) watts from accelerator pulse 70 (Figure 14). Note that the persisting yield-rate from each of the energy deposition volumes lies within a factor 2 of this figure. Summing the persisting-radiation power, we find that the total yield in the most aged puffs is of the order of 100 watt sec.

#### DISCUSSION

Total energy input to the atmosphere in each of the accelerator pulses is 2000 watt sec, and the "prompt" impact-excited fluorescence efficiency of air within the camera's wavelength sensitivity range is less than 2% (assuming no neutralization-associated discharge takes place in the rocket's vicinity; none is suggested by the groundbased spectrograph data, Ref 27). The light yield during the pulse proper would thus be under 40 watt sec. It is to say the least surprising that a comparable amount of energy (or more) comes out in delayed visible radiation; recall that no similar afterglow is observed in the aurora, for example.

No metastable species is known to produce such intense and long-persisting emission, and in any case the time dependence of the visible light output is inconsistent with such a simple decay process. The best-known air afterglow mechanism is the reaction of nitric oxide (known to be produced with high efficiency in irradiated air) with oxygen atoms, which results in the familiar yellow-green glow (which is cyclic and consumes odd O). A simple calculation shows, however, that to reach the measured radiant intensities the concentration of NO molecules would have to be at least comparable to the ambient  $[N_2 + O_2]$ , which is energetically not possible. No further known process involving air species alone appears capable of producing this PRECEDE afterglow. It may be associated with effluents from the rocket motor, which were seen to produce a bright chemiluminescent wake along the trajectory (Ref 27); if so, some explanation of why the emission is associated with the ionization-excitation from the electron pulse is needed.

## SECTION 4

### EXCEDE: SPECTRAL ENERGY-DEPOSITION DISTRIBUTIONS

#### INTRODUCTION

The original function of EXCEDE: Spectral's (EX851.44-1, 29 Oct 78; Ref 30) onboard radiometric cameras was to determine energy input rates within the fields of view of the payload's infrared spectrometers and radiometers. The image data, which are reviewed in Section 2 of Ref 22, are indeed directly suitable for this purpose. Their preliminary analysis, however, shows that the spatial distributions of visible radiance differ markedly from predictions of independent particle-transport models (Ref 31) both in individual scenes and in their dependence on the altitude (i.e., ambient atmospheric pressure) at which the 3 kV electrons are injected. This finding is supported by a recent analysis of some of the groundbased camera data (Ref 32), which disagree with the calculations at distances from the rocket beyond the onboard camera's effectively-100 meter range; and by the altitude profiles of air fluorescence measured by a photometer (Ref 33). Electric discharges, which are thought to assist in neutralizing charge-ejection spacecraft, have a different distribution of radiation-exciting secondary electrons than individual fast particles. If the observed peculiarity in energy input pattern is due to a discharge the infrared spectral intensities measured by EXCEDE's instruments would differ from those excited by energetic particles and photons from atmospheric nuclear explosions.

Hence emphasis in evaluation of the film data has been directed to determining volume emission rate distributions, from which glow excitation mechanisms can be inferred. Feature intensity ratios measured by the onboard instruments also play an important part in determining the energy spectrum of the electrons in the "plasma" produced by the ejected beam (into which the instrument point), as is discussed in Ref 22. Characterization of the ionized-excited volume near EXCEDE: Spectral applies not

only in interpreting the measured infrared chemiluminous efficiencies but also in designing spaceborne-accelerator investigations in which the spectroradiometric measurements are made from remote platforms (the mother-daughter concept). The optical data also provide estimates of the free electron concentrations, for planning measurements of the infrared plasma (bound-bound) atomic radiations.

Monochrome film frames from electron-injection altitudes 15-38 km below those in Ref 22 have been reduced. The spatial and altitude distribution data are presented here, with a discussion of their application in inferring energy distributions of the secondary and degraded-primary electrons.

#### BACKGROUND

We review briefly the photographic measurements, particulars of which are in Ref's 22 and 34. EXCEDE: Spectral's 30°-conical electron beam was directed upward along or near the direction of the geomagnetic field, at 60° from the rocket's long axis and toward the fields of view of its array of infrared instruments (see Fig 12 of Ref 22). Two co-aligned 94° x 62°-field cameras, one with color film and the other with monochrome film filtered for sensitivity at wavelengths  $< 4600 \text{ \AA}$ , viewed the beams from a point in or near the meridian plane  $3\frac{1}{2}$  meters south of the accelerator segment that provided most of the useful data. In this projection, the field line onto which the electrons are injected lies inside the camera's image field from "infinity" down to within  $1\frac{1}{2}$  meters from the port from which the electrons emerge. The cameras' viewing perspective provides good lateral spatial resolution to at least 30 meters from the rocket (and useful data to  $\sim 100 \text{ m}$ ), while the first refocusing node of 3 keV electrons in the geomagnetic field over Poker Range (where the rocket was launched) is at 21 meters. No node appears to be above detection threshold in any of the 500-odd data frames (although one may be present in an early frame in which  $< 0.1$  amperes was ejected).

Sequences of 8, 80, and 800 millisecc exposures were made to extend the dynamic range of scene brightness that could be recorded. The

black-and-white film is sensitive to  $N_2^+$  First Negative and  $N_2$  Second Positive band air fluorescence, and insensitive to the persisting 5577 Å OI line. The onboard cameras' high resolution close-in to the rocket -- in particular, in the region into which the infrared instruments point -- is complemented by lower-resolution ( $> 30$  m) photographs of the complete beam energy deposition pattern from groundbased cameras.

The films, which are the first from onboard a charge ejection vehicle, show a field aligned "core" with the magenta halo most probably due to excitation of  $N_2$  triplet state transitions (First and Second Positive bands) by slower, laterally-scattered secondary electrons. Several of the radiance distributions on the monochrome negative have been reduced manually, starting from equi-density contour plots made with a two-dimensionally-scanning microsensitometer (as in Sections 1 and 3). The brightness distributions when 7 amperes was ejected at 97.7 and 84.9 km on downleg are shown in Fig 15 (lens vignetting has been corrected out). Similar plots for 123 km upleg and 113 km downleg, with further clarification of the camera perspective and a plot indicating the horizontal scale, are in Ref 22. These "maps" serve as starting points for tracing radiance along physically-descriptive directions such as the core axis (Fig 16), and for unfolding to generate volume emission rates -- the "fundamental" indicator of plasma conditions present in the images.

#### DATA

As Fig's 15 and 16 show, within a few rocket diameters the glow's surface brightness increases very rapidly toward the accelerator and rocket body. Beyond this range the increase with distance is due principally to the increasing sight path through the (optically-thin) beam, that is, to viewing perspective. (The minimum is also present in Fig's 20 and 22 of Ref 22.) The glow has about twice the initial angular divergence measured in laboratory tests with the electron accelerator operated into  $10^{-4}$  -  $10^{-3}$  torr air pressure, and as noted no effects of refocusing show in the five isophote plots (the one for 116 km upleg, not reproduced here, qualitatively resembles the others).

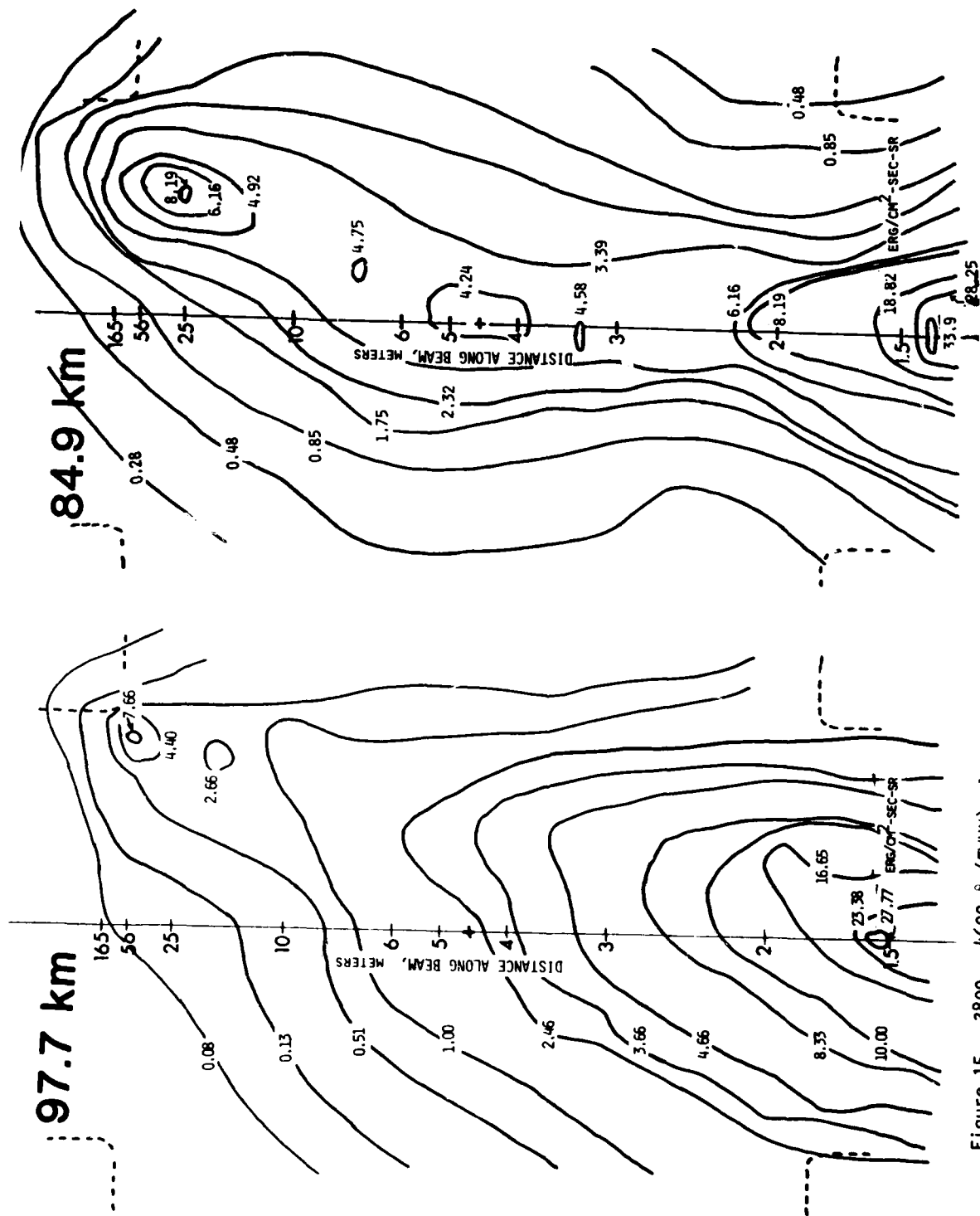


Figure 15. 3800 - 4600 Å (FWHM) glow radiance at two EXCEDE: Spectral downleg altitudes. Beam current is 7 amperes at 3 kV.



The radiance distribution along the beam's field-aligned axis, both in the region close-in -- whose "shape" is strongly at variance with the independent-particle transport model -- and beyond the minimum changes little (and not even monotonically with altitude) over the factor-250 range of ambient air density. While the close-in falloff might be explained by invoking a local discharge, or rocket outgassing (which is known to play a part in discharges, Ref 35), the small (factor < 3) variation with altitude at 10 - 100 meters from the rocket would not appear to be explained by an outgassing-related process.

A narrow range of emission intensities was also measured by an onboard photometer pointed near the minimum-radiance area on the films (Ref 33). This instrument showed much higher signals on upleg than on downleg at the same altitude. The effective  $N_2$ -molecule concentrations, assuming that this increase is due to outgassing (only), are given at top right of Fig 16. Additionally, ground camera data show that the energy deposited at 123 km ejection altitude does not fit an independent-particle model in either the first few hundred meters from the vehicle (where it is too high) or in the  $\frac{1}{2}$  to 3 km region (too low) (Ref 32). This finding indicates a redistribution of the energy of the initial injected beam, beyond that resulting from Coulomb collisions with atoms and molecules of ambient atmosphere. We note that the ground photography (at the one ejection altitude analyzed, 123 km) shows excess emission to ranges well beyond the  $\sim 5$  meter minimum in Fig 16.

#### DISCUSSION

Models of infrared surveillance-systems performance implicitly assume that the particles output from nuclear explosions -- thermal x-rays, debris ions/atoms,  $\beta$  and  $\gamma$ -rays -- act independently of one another in exciting the distant atmosphere (except when the doses are high enough to produce substantial heating). If the distribution of energies of the secondary, tertiary, ..... electrons in the air volume probed by EXCEDE differs from that from nuclear particles, the relative populations of infrared-emitting species (and their precursors) will

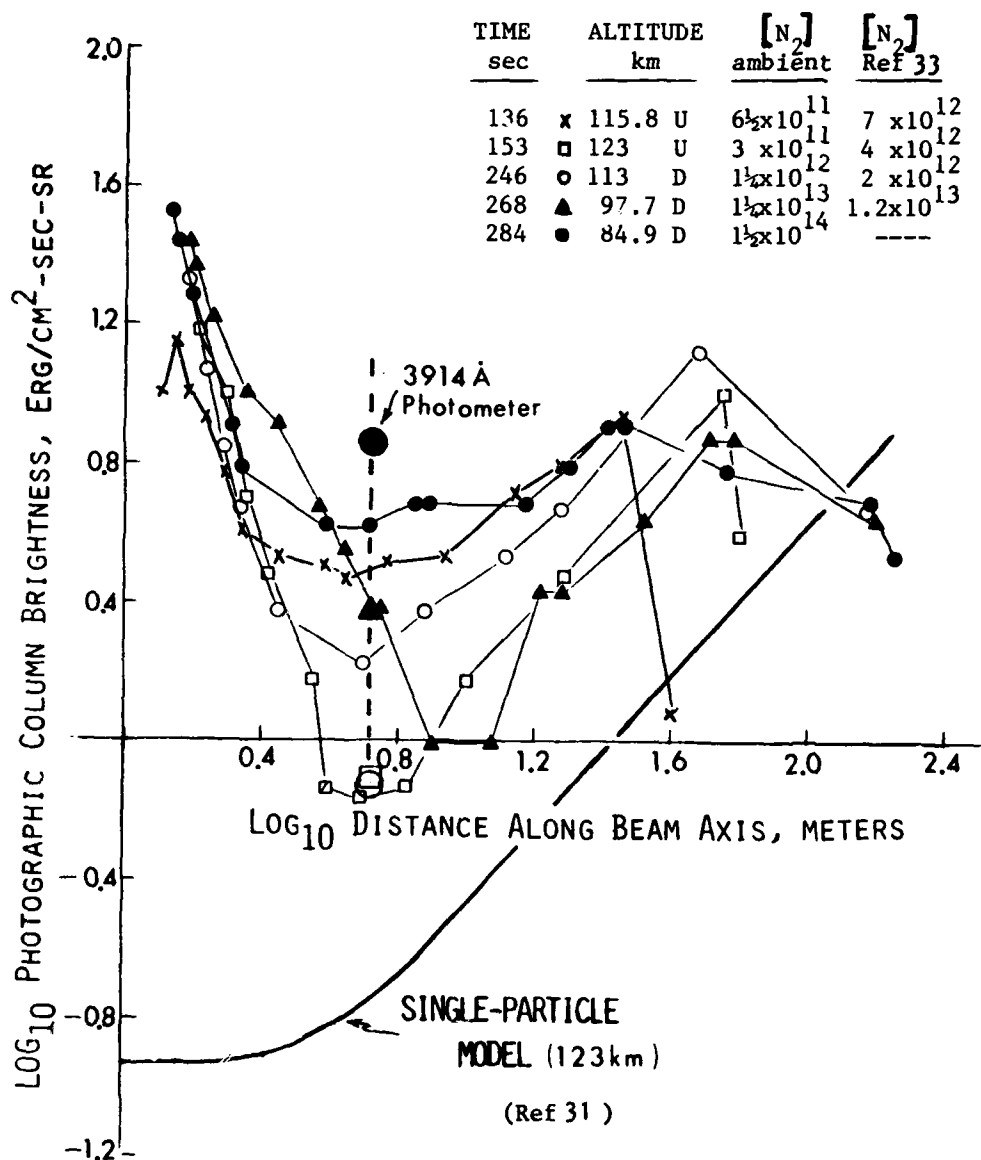


Figure 16. 3800-4600 Å EXCEDE: Spectral radiance along the injected electron beam's axis, projected to the onboard camera. Ambient N<sub>2</sub> density at the five ejection altitudes spans a range of about 250. Also shown are the radiances measured by a 3914 Å-band photometer pointed near the glow minimum.

be different, which would impair the accuracy of EXCEDE's simulation. For example an excess of electrons of kinetic energy near 3 eV would result in enhanced emissions from  $\text{CO}_2$  molecules, both by direct impact excitation and (in particular) increased energy transfer from  $\text{N}_2$  molecules, whose cross-section for vibrational excitation peaks near this electron energy.

This effect of this energy distribution on some of the atmosphere's emissions is shown schematically in Fig 17. After a few ionization mean free paths, an initially-monoenergetic electron beam is accompanied by a comparable number flux of slower secondary electrons and, because of the statistics of collisions, becomes spread in energy. (The energy spectrum shown in the top panel is in effect the DPOSIT distribution, which is input to ROSCOE's model for air fluorescence (Ref 36).) These secondaries vibrationally excite  $\text{N}_2$  and electronically excite  $\text{N}_2$ 's triplet manifold, which -- as pointed out in Ref 22 -- was unexpectedly strong in EXCEDE's spectrums. Additionally, non-homopolar molecules such as  $\text{CO}_2$  (and  $\text{H}_2\text{O}$ , whose infrared radiations were also strong at EXCEDE) have high cross-sections for vibrational excitation by soft electrons. Discharges produce large numbers of secondaries with energies of a few eV (in comparison to impact-ionization by the primary electrons (see Fig 17a), as shown in both laboratory and rocket experiments (Ref 37).

AFGL/OPR is currently evaluating spectroscopic data from EXCEDE: Spectral (Ref 33), to determine their fit to laboratory and auroral-measurement values. (Auroral electrons effectively simulate nuclear-particle excitation, as they have essentially the same secondary electron spectrum.) The ratio of column intensities in  $\text{N}_2$  Second Positive to  $\text{N}_2^+$  First Negative bands is indicated in Fig 18, which shows quantitatively the effect of  $\sim 10$  eV electrons on  $\text{N}_2$  triplet and vibrational-state excitation.

Discharges of two principal types, static (in effect corona, Ref 38) and beam-plasma (Ref 39), have been invoked as the source of the return current needed to neutralize the electron-ejection vehicle and beam. The flux of ambient electrons from the natural ionospheric plasma is only of

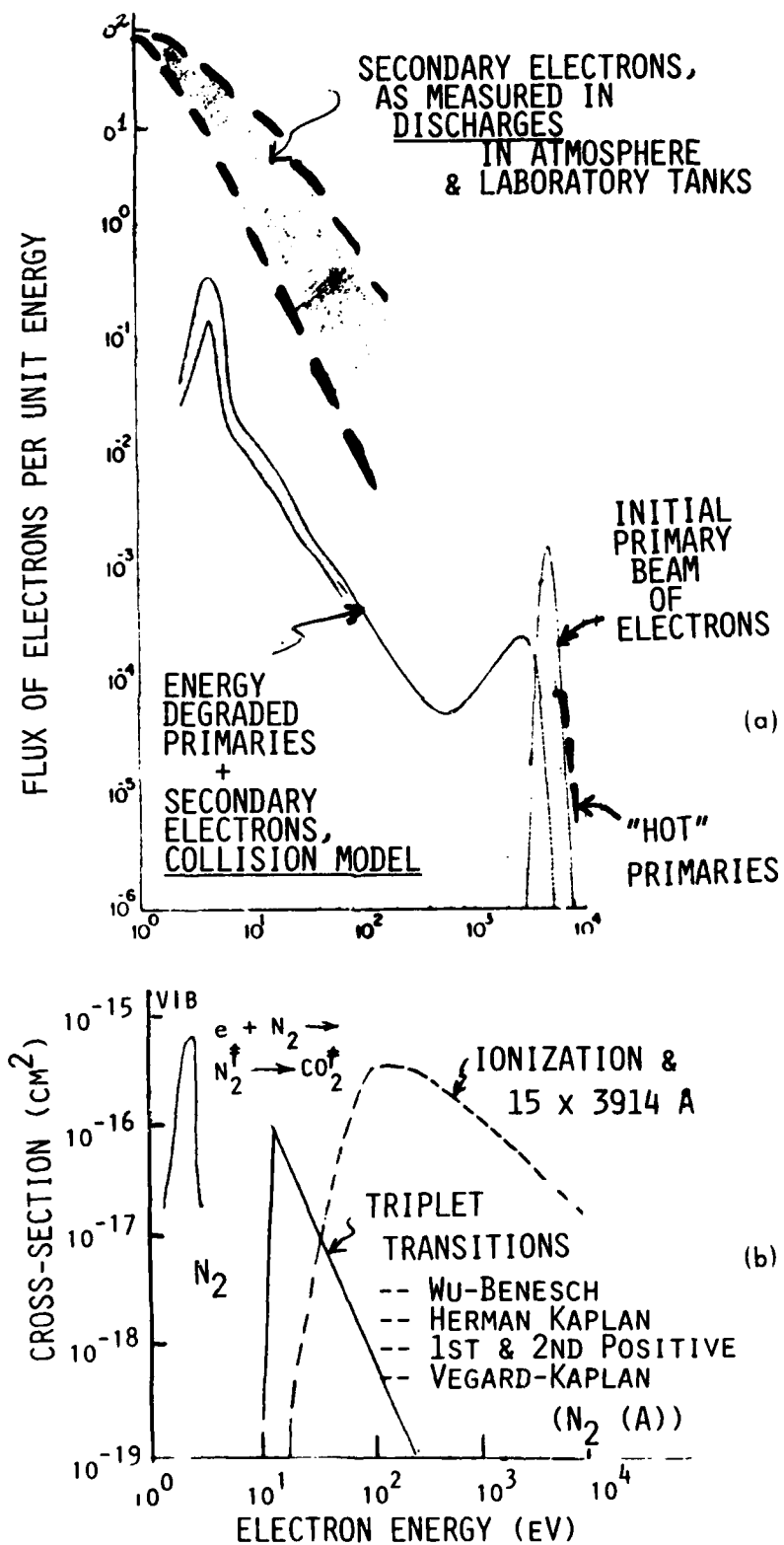


Figure 17. Model secondary electron flux spectra due to independent primary-particle collisions and to discharges (a), and cross-sections for impact excitation of N<sub>2</sub> by 1-10<sup>4</sup> eV electrons (b).

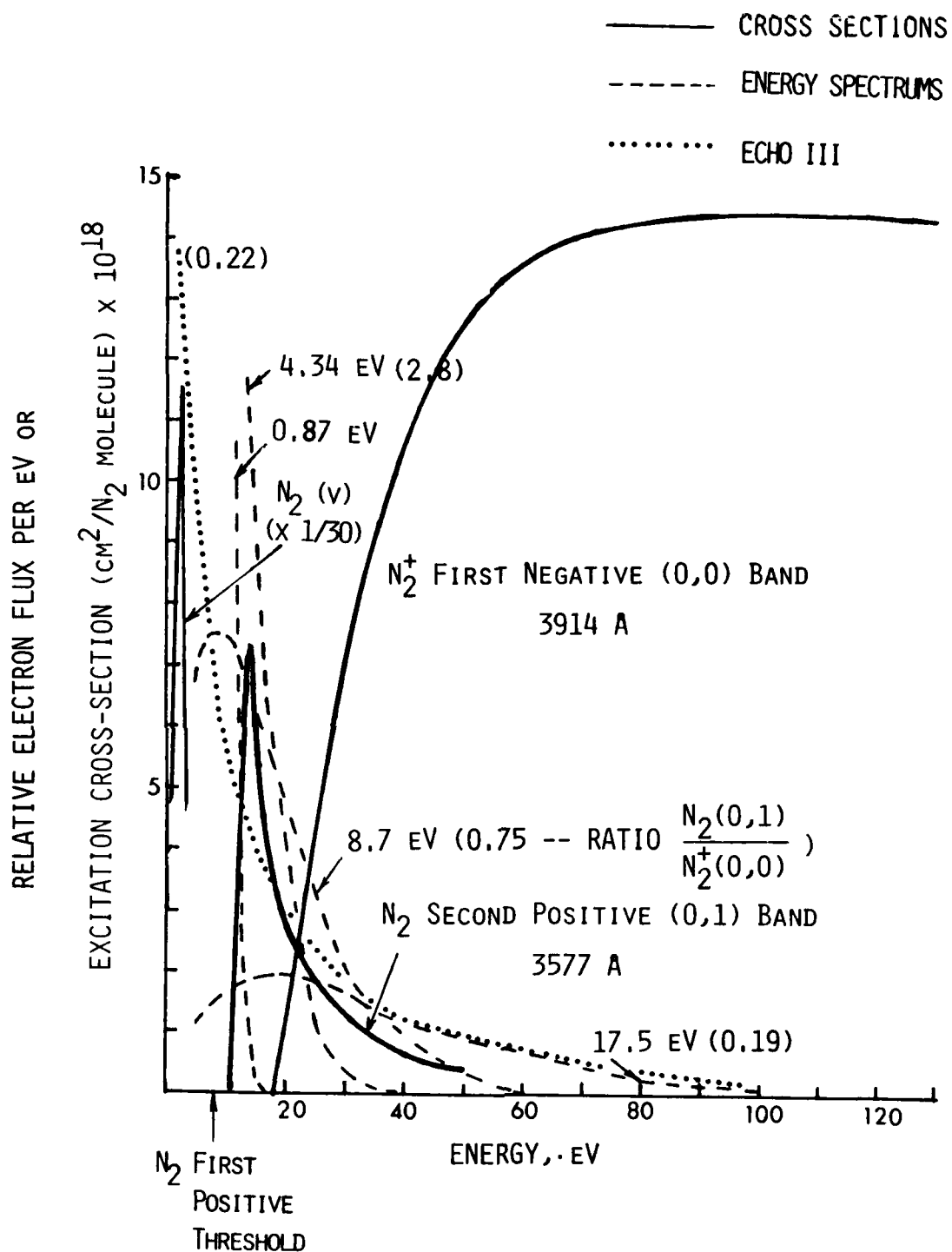


Figure 18. Excitation cross-sections and energy spectra of thermal electrons at temperature 0.87 - 17.5 eV. The spectrum measured on charge-ejection rocket Echo III (Ref 37) fits no unique temperature. Ratios of emission intensity in the features indicated are in parentheses.

the order of 1 milliamp per  $\text{m}^2$  of vehicle surface (Ref 39), and the departing electron beam is not believed to produce enough new free electrons nearby to maintain its potential at the observed (Ref 38) 10's of volts. Some observables of these discharges are listed in Table 8. The static discharge is driven by the space plasma-shielded vehicle potential, which produces a return current of  $\sim 100$  eV electrons (which is near the maximum of the excitation cross-section) that create still further secondaries near the vehicle. Beam-plasma interactions result in an RF discharge, in which can exist electric fields that broaden the energy distribution of the initial beam electrons themselves (as indicated in Fig 17a) and so, among other effects, destroy the refocusing.

It should be noted that simple Coulomb self-repulsion of the 7 ampere ejected beam could also be causing its broadening and apparent failure to refocus, as its expected "equilibrium" radius in a partially-ionized medium can be several meters (Ref 39). This space-charge effect could smear out the node so that its radiance contrast falls below detectability in the photographic projections.

The spatial distribution of volume rate of excitation can be derived by unfolding radiance distributions such as are shown in Fig 15, as the glow appears to a good approximation cylindrically symmetric. The ionization-dissociation rate is proportional to the rate of excitation of 3914 Å and 4278 Å  $\text{N}_2^+$  First Negative band radiation, which is the principal component of the photographic signal (the  $\text{N}_2$  Second Positive bands' contribution can be estimated from the spectrum data). Summing of these volume emission rates thus determines the total energy input rate within the fields of individual onboard instruments.

These excitation-ionization rates also serve in estimating free electron densities, which are needed to assess the intensities of plasma emissions. At equilibrium between creation and chemical loss of electrons, and for electron densities  $n_e$  in the expected range (where two-body reactions dominate),  $Q = \alpha n_e^2$ , where  $\alpha$  is the recombination coefficient. Dissociative recombination with molecular ions is the dominant neutraliza-

Table 8. Characteristics of "corona" discharge and Beam Plasma discharge

	<u>Corona</u>	<u>BPD</u>
<u>Basic Concept</u>	DC avalanche of ambient electrons driven by electrostatic field from vehicle	Instability in ambient plasma driven by beam's charge, RF fields grow to accelerate electrons above the ionization threshold of atmospheric molecules/atoms
Current/Voltage at ~140 km altitude	~1 mA, 3 kV	~80 mA, 3 kV threshold
Threshold	Continuous process	Sharp but with some structure near onset
Effect on initial beam radiance distribution	Virtually none if the return current is isotropic; within a few rocket radii if the current flows in the path ionized by the ejected beam	Pitch angle scattering results in lateral broadening, intensified backward beam component, focusing node destruction; factor-10 increase in total fluorescence yield within ~200 meters; longitudinal distribution warped by heating of beam
Optical flicker	Not observed, may be present	At ion cyclotron frequency ~20 Hz
RF emission	No	At and above plasma frequency, complex spectrum
Secondary electrons	It is expected that some differences in the energy distribution can be identified in the theory. BPD probably results in a broader angular distribution at each energy, and should show "suprathermal tails" of ~100 eV electrons, which behave much like primaries.	

tion reaction, when the density of molecular ions is  $> 10^{-5}$  that of atomic ions, as would be expected under EXCEDE: Spectral's conditions. (This is the reverse of using free electron densities measured by the Chatanika incoherent-scatter radar for determining energy input rates in the auroral ionosphere, which also requires knowledge of  $\alpha$ ; see Ref 40.) We note that estimates of  $n_e$  in discharges produced by electron injection vary from less than  $10^8$  to more than  $10^9$  per  $\text{cm}^3$ .

The spatial distributions of volume emission rate that result from the neutralization-assisting processes would have the following general properties.

Corona: varying relatively slowly with distance from the rocket (Ref 38), and not confined to the initial beam volume.

Beam-plasma discharge: lateral broadening due to pitch angle scattering of the ejected electrons, and an axial distribution altered by heating of the beam (that is, it is spread to both higher and lower energies); confined to the (expanded) beam volume. We note that beam-plasma discharge is not expected to occur at the air pressures below  $\sim 95$  km altitude; and that the film data so far do not indicate any sharp transitions in the radiance pattern.

Outgassing: confined to the region partially ionized by the outgoing beam; depends on the distribution in space of the outgassed molecules, which can be calculated.

As noted, identification of the neutralization mechanism would provide an indication of the effect of secondary electrons on EXCEDE: Spectral's infrared data. The primary effect of outgassing is to change the apparent altitude profiles of the infrared yields; while the emission spectrum may be changed by the introduction of new chemical species ( $\text{H}_2\text{O}$  in particular), outgassed molecules do not change the flux of secondary electrons relative to the primary beam.



## SECTION 5

### RADIANCE STRUCTURE OF THE LOWER THERMOSPHERE

#### BACKGROUND

Air Force Geophysics Laboratory recently made a six-month satellite survey of the spectral intensity of 1100 - 2900 Å ultraviolet radiation from the earth's atmosphere, with high-resolution spectrometers and a wavelength-cycling narrow-field photometer on a polar-orbiting vehicle (Ref 41). The spacecraft, DoD S3-4, was near sun-synchronous at an inclination of about 96.5° and crossed the equator at 1030 and 2230 LT. The radiance-measuring instruments (of experiment CRL-726) viewed directly toward the nadir from altitudes between 160 and 260 km.

When the thermosphere is sunlit, almost all of its vacuum UV emission (wavelength  $\lesssim$  1800 Å) is fluorescence of  $N_2$  and O excited by photoelectrons ejected from air molecules and atoms by extreme UV solar photons (wavelength  $\lesssim$  600 Å). Absorption by the atmosphere's  $O_2$  molecules in their Schumann-Runge continuum prevents most VUV photons that originate below approximately 110 km (the exact number depends on the wavelength) from reaching satellite altitudes. Variations in the mixing ratios  $[N_2]/[O_2]/[O]$  would vary the radiances of the  $N_2$  and O dayglow features, through the change in both the concentrations of target (emitting) species and the energy spectrum of the secondary electrons, and also because of the change in attenuation of upward-directed VUV photons. It is safe to assume that the incident EUV flux's variation has only small frequency components at the spatial scales of surveillance-systems interest (a few km, which considering the satellite's orbital velocity of 8 km/sec translates to  $\sim 1$  Hz in the solar irradiance). Thus fluctuations in the VUV column intensities measured from S3-4 would provide a measure of the atmospheric-species structure at altitudes from which this radiation is emitted.

Spatial structure of typical scale size 30 km near 150 km altitude has been observed at high latitudes by satellite-borne probes (Ref's 42, 43). The variations in the concentration of argon atoms and in mixing ratios are associated with geomagnetic storms. These in situ measurements suggest a similar inhomogeneity of infrared-active molecular species such as  $\text{CO}_2$ , which would lead to irregularities in the sky background presented to IR surveillance sensors when the upper atmosphere absorbs energetic radiations from nuclear explosions; this "clutter" mimics radiating targets and otherwise degrades system performance.

The VUV radiance distribution remotely sensed from S3-4 provides an opportunity to investigate further this variability of species concentrations in the lower thermosphere, particularly at high spatial frequencies ( $\geq 1$  cycle/km, the photometer's footprint being  $< 1$  km). Hence we have made a preliminary analysis of the photometer data from one flight segment, to determine if the nadir radiance distribution differs from that expected and, if so, to assess the effort required to quantify the spatial inhomogeneity.

#### DATA BASE

S3-4's photometer isolated  $\sim 150$  Å FWHM wavelength bands centered near 1216, 1340, 1550, and 1750 Å, with full field of view 5.9, 1.65, 0.46, or 0.12 degrees circular (details are in Ref 41). An examination of published (in Ref 41) daytime data traces at those altitudes where the radiance signals are virtually uncontaminated by aurora indicated that the 1550 Å data have the largest short-period ( $\sim 10$  sec, 80 km satellite traverse) fluctuations. This finding would be expected because the photometer channel measures principally the optically-thin  $\text{N}_2$   $a^1\pi_g - X^1\Sigma_g^+$  Lyman-Birge-Hopfield bands (largely in the  $\Delta v = -1$  to  $-4$  sequences), which are emitted from altitudes 135 to 180 km FWHM (Ref 44). Smooth-appearing data traces are shown from the 1340 Å channel (which responds principally to the optically-thick OI Å resonance triplet), the 1216 Å channel (mostly optically-thick Lyman- $\alpha$  along with some OI resonance

radiation), and in the 1750 Å channel (whose signal is dominated by Rayleigh scatter from altitudes well below 100 km).

We therefore selected for this first analysis a segment of the daytime radiance from this photometer, whose half-maximum response is at 1485 - 1650 Å and tenth - maximum at 1470 - 1740 Å. Its field of view had been set at 1.65° during the segment chosen. The data from the complete satellite revolution (445, 13 Apr 78), compressed and processed to nadir radiance (and hand-smoothed), are in Figure 7 of Ref 41. Figure 19 is a plot of the number of counts in 1/100 of the 0.0100-sec sampling intervals, in the period when the solar zenith angle is less than 100° (so that the thermosphere is sunlit). The full set of data points for this period was provided to PhotoMetrics by AFGL as a numerical listing and on magnetic tape in a format suitable for processing by AFGL's CDC-6600 computer.

Figure 19 gives in addition to universal time the local (solar) time and solar zenith angle at the VUV instrument's latitude-longitude, which are listed along with its altitude. We narrowed the initial investigation down to a sunlit region at high latitude but well south of the auroral oval. Specifically, we chose the ~23,000 VUV radiance data points accumulated between 0428:01 and 0431:52.9, when the satellite was moving southward between 77½° and 62°N latitude (over north central Siberia). During these four minutes the instrument's altitude decreases from 171½ to 166 km, that is, it is moving downward through the L-B-H band-emitting altitudes. As its latitude decreases the sun's elevation angle -- which determines the EUV flux incident on the atmosphere -- increases, from 21° to 36°. The mean VUV radiance is seen to increase by a factor 1.63 during the data segment, while the component of solar irradiance normal to the horizontal increases by a factor 1.64 ( $= \sin 36^\circ / \sin 21^\circ$ ). Hence we may conclude that the increase in EUV flux has a much greater effect on the atmosphere's radiance than the decrease in absorption of this energy in the column defined by the nadir-pointing instrument's field. The ~5 sec-averaged radiance increases about 13% per min and the "footprint" of the photometer's field of view at the

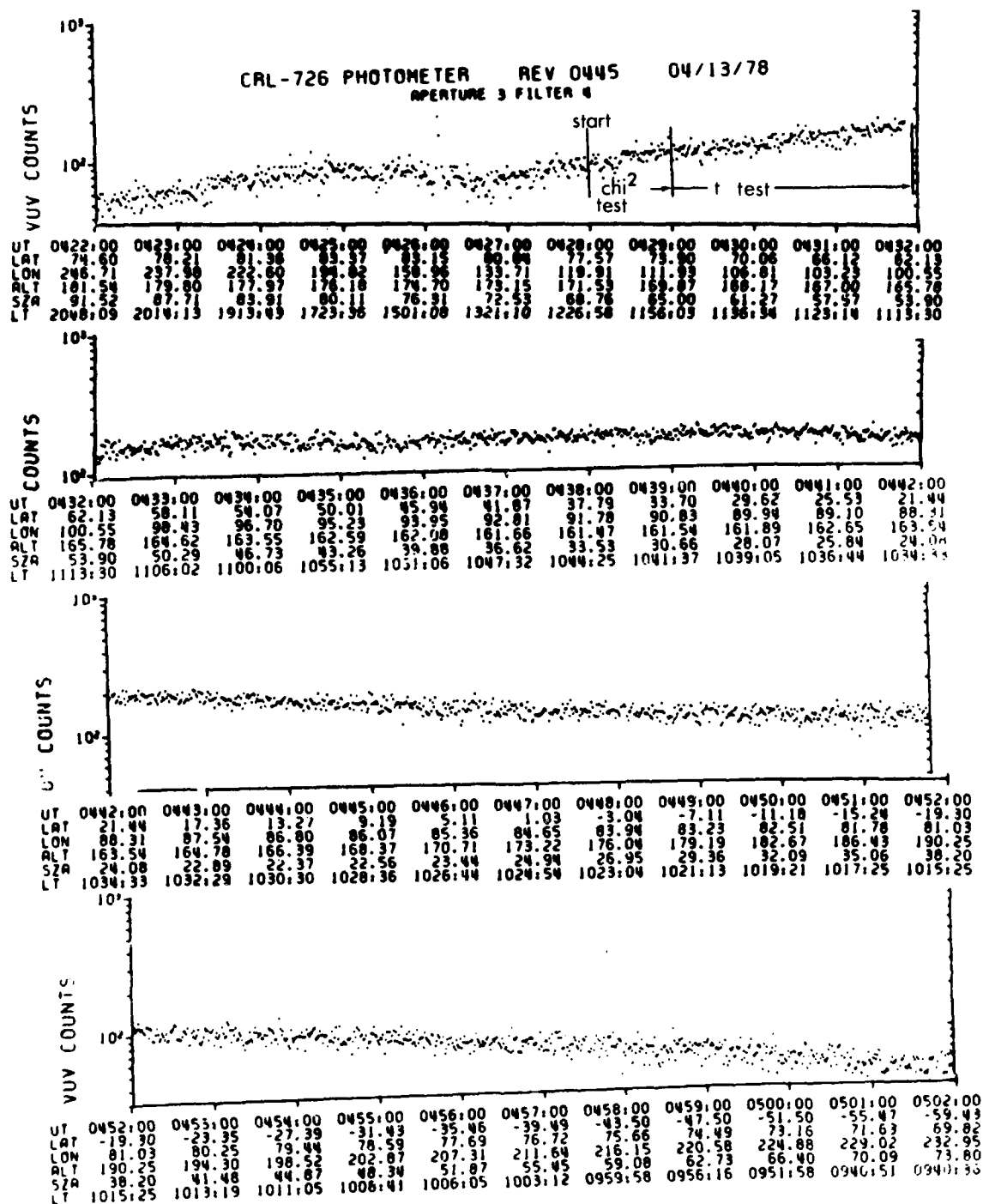


Figure 19. Number of 1550 Å photometer counts per 0.01 sec sampling interval in the daytime section of Revolution 445, Satellite S3-4. The data segments considered are indicated at upper right.

altitude of peak emission, 150 km, decreases from 620 to 460 meters over the data period; the spacecraft's 8 km/sec orbital velocity moves this field horizontally one projection diameter in 0.08 to 0.06 sec.

Plots in Ref 45 of the  $Q = 3$  auroral oval indicate that the segment of satellite track is  $> 1000$  km south of the oval;  $K_p (\approx Q)$  was only 2+ at the time of measurement (Ref 46). In fact, the northern oval, being centered near  $280^\circ$  longitude,  $77^\circ$  latitude, rarely expands below  $77\frac{1}{2}^\circ$ N at the satellite's  $110^\circ$  longitude. The absence of auroral contamination of the VUV radiance is further qualitatively indicated by lack of obvious spikes in the trace. The magnetic activity index  $A_p$  for 11, 12, and 13 Apr 78 was 64, 29, and 24 (Ref 46); the most magnetically disturbed day of the month was two days before the 13 April data period.

#### DATA ANALYSIS

In the absence of geophysical or instrumental perturbations, the number of counts of random independent events in sampling intervals of fixed duration will be Poisson-distributed. Since the average number of 1550 Å-band photons registered each 1/100 sec is as high as 100, the Poisson distribution can be extremely closely approximated by a normal (Gaussian) whose variance is equal to the mean (see, for example Ref 47). That is, the probability density at  $N$  counts would be  $(2\pi)^{-\frac{1}{2}} \exp -(N-\bar{N})^2/2\bar{N}$ , where  $\bar{N}$  is the mean or expectation number (about 100, as noted).

Instrument instabilities -- in photometric response, or as jitter in the length of the sampling interval -- were found by the experiment group to have a negligible effect on the seconds-scale variations in count rate. Dark current averages less than 1/100 count per sampling interval, and its noise in any case adds in quadrature to that due to the natural fluctuation in rate of arrival of VUV photons.

The geophysical effects on the atmosphere's VUV radiance include the long period change due to the increasing elevation angle of the sun, evident in Figure 19; variations due to variable EUV output from the sun, which as noted are small at the time scales of interest; and the afore-

mentioned inhomogeneity of species concentrations limits. Periodicities in the radiance data stream, which would appear as peaks in its power spectrum, would help identify the source(s) of the atmospheric perturbation. For example, spatial structure might be found to have characteristic wavelengths comparable to those of traveling ionospheric disturbances. Considering that the magnitude (or even existence) of fluctuations beyond those expected from pure photoelectron counting statistics is not established, however, we judged it more cost-effective to first apply simple statistical tests (rather than Fourier-transform methods) to the data set.

We applied (from the large number of available tests of the statistics of data sets) Student's t-test to determine whether the mean and variance are equal within statistically-allowed limits and the chi-square test to determine how well the daytime VUV data fit the aforementioned normal distribution. It was necessary to filter out the effect of the slow trend in the signal, which in fact turned out to reduce the reliability of the analysis.

#### Student's t-test

This well-known procedure tests a hypothesis about the mean of a sample of data. We hypothesize first that the photoelectron counts are Poisson distributed, that is, that their mean is equal to the variance. The parameter  $t$  is defined as

$$\frac{(\text{mean of sample}) - (\text{"true" mean})}{(\text{standard deviation of sample})/(\text{number of data points } n)^{1/2}}.$$

The probability that  $t$  is less than  $p$ , or percentile of the  $t$  distribution for the number of degrees of freedom (which is to an excellent approximation  $n$ ), is  $2p - 1$ . That is, when  $t < p$  we are confident at the  $2p - 1$  level that the population (true) mean lies within (standard deviation)  $\times (t/\sqrt{n})$  of the sample mean. If the standard deviation of the VUV radiances lies between these confidence limits we accept the hypothesis that they are Poisson distributed, which is to say, that the photons are arriving at the satellite as independent quantum events from a uniformly-emitting atmosphere.

As the low-frequency trend in the data has the effect of increasing the variation, we attempted to remove the trend by filtering. We calculated running means of length  $\ell$  consecutive samples -- low pass filtering --, which when subtracted from each individual data point -- high-pass filtering -- makes the new mean very close to zero (detrending). Table 9 shows results of application of these filters with  $\ell$  up to 300 on segments of the data stream.

Without detrending ( $\ell = 1$ ) the variances for sample lengths greater than 500 data points (5 sec of satellite data) become unrealistically high, and with  $\ell = 20$  (1/5-sec integration) they remain considerably larger than the means. Application of the t-test with 95% and 99.9% confidence limits (Table 10) shows the variance to be just outside the expected range when the complete 2300-point data set is high-pass-filtered with  $\ell = 50$ ; it also outside the range in two of the three subsets with  $\ell = 20$ . This means that the hypothesis of a Poisson-distributed set of VUV radiance data is rejected at these levels of confidence.

#### Chi-square Test

This test (Ref 48) assesses the "goodness of fit" of experimental data to a preselected statistical distribution. In light of the failure of the assumption of a Poisson distribution, we adopted the hypothesis that the radiance readings are Gaussian (normally) distributed. To minimize the effect of the long-period trend, we divided the data set into 3.2 sec intervals, during which the mean count rate changes by  $< 1\%$ ; and we treated the first 20 such contiguous intervals after 0428:01. The procedure involves finding the mean and standard deviation of each data subset, placing the readings into  $K$  bins of uniform count-number width, and then calculating  $\chi^2 = \sum_{i=1}^K (f_o - f_e)^2 / f_e$ , where  $f_o$  is the observed occurrence of the number of counts and  $f_e$  the expectation occurrence or frequency (in terms of a normal distribution having the computed mean and standard deviation). We applied standard procedures for lumping together the sparse number of data points that lie several standard deviations from the mean, which improves the statistics.

Table 9. High and low-pass filtering of the S3-4 VUV data\*.

Number of Sample Points	Filter Length $\lambda$	Mean, $\bar{N}$	Variance of Sample
-- High Pass --			
23295	1	116.01**	424.24
23295	6	-0.0010	100.23
23295	10	-0.0008	107.60
23295	50	-0.00014	117.23
23295	100	-0.0011	118.42
23295	300	-0.0007	118.48
120	1	87.09**	79.14
250	1	86.7**	83.56
500	1	86.94**	88.79
500	20	-0.0161	79.61
1150	1	88.28**	94.23
1150	20	-0.0377	87.18
2300	1	89.56**	95.71
2300	20	-0.0062	85.67
-- Low Pass --			
500	20	83.39	301.86
1150	20	86.75	140.54
2300	20	88.73	77.01
23295	20	115.91	321.32

\* Starting at 042801, Revolution 445

\*\* Mean number of counts in sample



Table 10. Results of t-test of the S3-4 VUV data\*.

<u>Number of Sample Points</u>	<u>Filter Length <math>\ell</math></u>	<u>Mean <math>\bar{N}</math></u>	<u>Variance</u>	<u>95% Confidence Limits</u>	<u>99.9% Confidence Limits</u>
500	20	83.39	79.61	$\pm 0.782$	$\pm 1.313$
1150	20	86.75	87.18	$\pm 0.539$	$\pm 0.906$
2300	20	88.73	85.67	$\pm 0.378$	$\pm 0.635$
23295	50	115.91	117.23	$\pm 0.139$	$\pm 0.233$

	<u>95% Confidence Limits on Mean</u>	<u>Variance Within Limits?</u>	<u>99.9% Confidence Limits on Mean</u>	<u>Variance Within Limits ?</u>
500	82.6 - 84.17	No	82.07 - 84.7	No
1150	86.21 - 87.28	Yes	85.84 - 87.65	Yes
2300	88.35 - 89.10	No	88.09 - 89.36	No
23295	115.77 - 116.04	No	115.67 - 116.14	No

\*High pass filtered; starting 042801, revolution 445

The number of "degrees of freedom" for the test is taken as  $K-2$  because the two parameters mean and standard deviation are taken from the data sample.  $\chi^2$  is tabulated (in Ref's 47 and 48, for example) as a function of the number of degrees of freedom and the statistical significance level. If the  $\chi^2$  calculated from the experiment data set is less than the tabulated value, the hypothesis is acceptable at the significance level selected.

We adopted for computational convenience a bin size of 4 photoelectron counts (for example, 96 to 99 in the 0.01 sec interval) after preliminary calculations indicated that the result was not critically dependent on this figure. The resulting means, variances (square of standard deviation), and the chi-squares for the 99.5% significance level are shown in Table 11. It is found that 19 of the 20 data subsets (all except the 10th) are in agreement with the hypothesis of a normal distribution at this significance level. This finding provides a very strong indication that the VUV radiance data in this 64 sec measurement interval are normally distributed.

The variances, however, are somewhat larger than expected from pure photon-arrival statistics, which suggests that some further random process is taking place. 13 of the 20 variances are greater than their corresponding means and the mean of the variances (Av 1-20 entry in Table 11) is  $4\frac{1}{2}\%$  greater than the mean of the means. This finding implies that a phenomenon other than photon noise could be impacting the radiance data. Its rms magnitude would be about 30% of the  $\sim 10\%$  ( $100^{-\frac{1}{2}}$ ) relative photon noise fluctuation (as  $1.045 = (1 + 0.3^2)^{\frac{1}{2}}$ ), or 3% of the mean signal amplitude.

#### SUMMARY

As noted, the statistical tests applied to CRL-726's VUV data are intended to determine whether fluctuations in the nadir radiance measured from the S3-4 satellite over and above quantum (photon, or more strictly speaking photoelectron) noise are present. A strongly positive result

Table 11. Chi-square Test of VUV Data\*

Data Section	K	Mean Counts	Variance	$\chi^2$		
1	8	86.8	83.1	16.44		
2	10	88.1	104.0	10.44		
3	9	89.2	92.6	18.70		
4	9	89.6	99.2	9.98		
5	9	89.3	82.8	21.64		
6	9	90.9	93.5	17.44		
7	9	92.0	84.3	17.05		
8	10	93.3	111.8	14.68		
9	10	92.7	104.5	14.34		
10	10	93.9	112.6	28.12		
11	9	94.0	96.3	14.23		
12	10	96.0	91.9	22.26		
13	9	97.5	89.4	21.91		
14	10	101.1	109.5	20.63		
15	10	101.6	112.6	11.84		
16	10	103.6	96.8	15.87		
17	11	106.6	125.5	16.87		
18	9	106.6	103.2	15.21		
19	10	104.8	108.5	16.78		
20	9	101.9	107.5	11.82		
Av 1-10		90.58	96.84			
Av 11-20		101.37	104.11			
Av 1-20		95.98	100.48			

Tabulated

$\chi^2$

for 99.5%

K	$\chi^2$
8	22.0
9	23.6
10	25.2
11	26.8

\* Starts at 042801, S3-4 Rev 445, 1550 Å photometer.  
320 samples, 4 counts per bin.

would indicate a search for periodicities that might be explainable as geophysical effects on the mixing ratios of species that emit (and absorb) Lyman-Birge-Hopfield band ultraviolet excited by sunlight between about 135 and 170 km (the satellite's) altitude.

In the absence of such lower-thermospheric perturbations the numbers of counts would be expected to be Poisson-distributed. Student's t-test shows that the count-rate data sample selected, when their long-term trend is removed by high pass filtering, do not fit this distribution. The Chi-square test shows the 0.01 sec radiance samples in individual 3.2 sec,  $\sim 25$  km-longitude segments to be normally distributed, but with means somewhat higher than expected. This suggests again that short-period ( $< 25$  km) atmosphere processes are affecting the VUV column emission. As noted above, periodicities in this variation can be assessed by applying autocorrelation - Fourier transform methods to the data stream. We judge that it would also be useful to investigate the statistics of the fluctuations when the magnetic disturbance index  $K_p$  is higher than in the data set assessed here (2+), as the high-latitude density variations are associated with magnetic activity (Ref 42).

We point out again that a finding of fluctuations in the 1485 - 1650 Å FWHM vertical-column radiance of the sunlit atmosphere means that infrared emission when the  $\sim 135 - 180$  km altitude region is uniformly dosed by nuclear radiations will be by and large similarly structured. For example the infrared volume emission rates from NO (largely from O atom interchange reactions) and  $O_3$  (thermal and chemiluminescent emission, and scattering of earthshine) would follow the concentration of O atoms; and the  $CO_2$  concentration is expected to be coupled to that of the heavier minor species. (Conversely, weak clutter in the sky's L-B-H radiance signal would mean high signal/background noise in surveillance systems operating in this (broad) band of VUV wavelengths.)

## REFERENCES

1. I.L. Kofsky and D.P. Villanucci, Further Assessment of Infrared Data from Aircraft and Rocket Probes, DNA 5127F (30 Nov 79).
2. Proceedings of the (11-13 Nov 1979) Workshop/Symposium on the Preliminary Evaluation of the Ionospheric Disturbances Associated with the HEAO-C Launch, with Applications to the SPS Environmental Assessment, Department of Energy, Unpublished.
3. P.A. Bernhardt, Plasma Fluid Instabilities in Ionospheric Holes, submitted to J. Geophys. Res. (1981).
4. R.B. Sluder, W.S. Andrus, I.L. Kofsky, and D.P. Villanucci, Aircraft Program for Target, Background, and Sky Radiance Measurements, AFGL-TR-78-0123 (18 May 78).
5. H.G. Horak, D.J. Simons, and J.H. Wolcott, EOS 59, 334 (1978).
6. M. Mendillo and J.M. Forbes, J. Geophys. Res. 83, 151 (1979).
7. D.N. Anderson and P.A. Bernhardt, J. Geophys. Res. 83, 4777 (1978).
8. P.A. Bernhardt, J. Geophys. Res. 84, 793 (1979).
9. J. Zinn and C.D. Sutherland, Atlas-Centaur/HEAO-C Launch, Ionospheric Effects, Computer Model Predictions, in Ref 2.
10. D. Golomb and M.A. MacLeod, J. Geophys. Res. 71, 2299 (1966).
11. J.M. Forbes and M. Mendillo, J. Atm. Terr. Phys. 38, 1299 (1976).
12. R.W. Schunk, Planet. Space Sci. 26, 605 (1978).
13. J.A. Chamberlain, Physics of the Aurora and Airglow, Academic Press, New York, 1961, p486 ff.
14. A.E. Hedin et al., J. Geophys. Res. 84, 1 (1979).
15. P.A. Bernhardt, J. Geophys. Res. 84, 4341 (1979).
16. W.R. Wadt, P.J. Hay, and D.C. Cartwright, LANL Internal Memorandum T-12(2-77)44, Feb 1977.
17. M. Mendillo and J. Baumgardner, private communication (1981).

# REFERENCES (continued)

18. R.H. Garstang in *The Airglow and Aurorae* (ed E. Armstrong and A. Dalgarno) Pergamon, New York, 1956, p324.
19. P.B. Hays, D.W. Rusch, R.G. Roble, and J.C.G. Walker, *Rev's Geophys. Space Phys.* 16, 225 (1978).
20. H.R. Luxenberg and R.L. Kuehn, *Display Systems Engineering*, McGraw-Hill, New York, 1968.
21. I.L. Kofsky, D.P. Villanucci, and W.S. Andrus, *Assessment of Rocket-borne and Airborne Infrared Data*, DNA 4731F (30 Nov 78).
22. I.L. Kofsky, D.P. Villanucci and R.B. Sluder, *Evaluation of Infrared Simulation Data*, DNA 5521F ( 26 Nov 80).
23. I.L. Kofsky, D.P. Villanucci, and R.B. Sluder, *Data Reduction and Auroral Characterizations for ICECAP III*, HAES Report No. 59, DNA 4220F (31 Jan 77).
24. R.B. Sluder, W.S. Andrus, and I.L. Kofsky, *Aircraft Program for Target, Background, and Sky Radiance Measurements*, AFGL-TR-79-0139 (15 Jun 79).
25. D.H. Archer, *Requirements for Improved Infrared Prediction Capability*, HAES Report No. 78, DNA 4585F (30 Apr 78).
26. M.H. Rees and D. Luckey, *J. Geophys. Res.* 71, 5181 (1974).
27. R.R. O'Neil, F. Bien, D. Burt, J. A. Sandock, and A.T. Stair, Jr., *J. Geophys. Res.* 83, 3273 (1978).
28. C.W. Allen, *Astrophysical Quantities*, Athlone Press, New York, 1955.
29. Eastman Kodak technical data.
30. R.R. O'Neil, A.T. Stair, Jr., E.T. P. Lee, D. Burt, and G. Frodsham, *EXCEDE: Spectral: An Artificial Auroral Experiment*, Paper AIAA-81-0422, AIAA 19th Aerospace Sciences Meeting, 12-15 Jan 81.
31. D.H. Archer, *EXCEDE Energy Deposition: Theory and Experiment Compared*, DNA 5525F (30 Nov 80).
32. D.H. Archer, *DNA Data Review Meeting*, 13-17 Jul 81.
33. R.R. O'Neil, private communication (1981).

# REFERENCES (concluded)

34. I.L. Kofsky, R. B. Sluder, and D.P. Villanucci, Onboard Radiometric Photography of EXCEDE: Spectral's Ejected-Electron Beam, NATO Advanced Research Institute, Geilo, Norway, 21-26 Apr 81 (in press).
35. G. Israelson and J.R. Winckler, J. Geophys. Res. 84, 1442 (1979).
36. T.L. Stephens and A.L. Klein, Electron Energy Deposition in the Atmosphere (Vol 1), GE-TMP-7 (May 1975).
37. J.R. Winckler, Rev's Geophys. Space Phys. 18, 659 (1980).
38. R.E. Leadon, A.J. Woods, E.P. Wenaas, and H.H. Klein, An Analytical Investigation of Emitting Probes in an Ionized Plasma, Jaycor Report J200-80-250A/2172 (12 Apr 81).
39. L.M. Linson and K. Papadopoulos, Review of the Status of Theory and Experiment for Injection of Energetic Electron Beams in Space, LAPS 65, Science Applications, Inc. (1980).
40. V.B. Wickwar, M.J. Baron, and R.D. Sears, J. Geophys. Res. 80, 4364 (1975).
41. R.E. Huffman, F.J. LeBlanc, J.C. Larrabee, and D.R. Paulsen, J. Geophys. Res. 85, 2201 (1980).
42. C.R. Philbrick, G.P. McIsaac, and G.A. Faucher, COSPAR Space Research XVII (ed. Rycroft and Stickland), Pergamon, New York, 1977.
43. C.R. Philbrick, COSPAR Space Research XVI (ed. M.J. Rycroft), Akademie-Verlag, Berlin, 1976.
44. R.R. Meier, D.J. Strickland, P.D. Feldman, and E.P. Gentieu, J. Geophys. Res. 80, 2177 (1980).
45. S.-I. Akasofu, Polar and Magnetospheric Substorms, Springer, New York, 1968, p8.
46. J.V. Lincoln, J. Geophys. Res. 83, 3906 (1978).
47. H.W. Alexander, Elements of Mathematical Statistics, Wiley, New York, 1961.
48. M.R. Spiegel, Theory and Problems of Statistics, McGraw-Hill, New York, 1961.

# DISTRIBUTION LIST

## DEPARTMENT OF DEFENSE

Defense Nuclear Agency  
2 cy ATTN: RAAE  
4 cy ATTN: TITL

Defense Technical Information Center  
12 cy ATTN: DD

Field Command  
Defense Nuclear Agency  
ATTN: FCPR, J. McDaniel

Field Command  
Defense Nuclear Agency  
Livermore Branch  
ATTN: FC-1

Interservice Nuclear Weapons School  
ATTN: TTV

Under Secretary of Defense for Rsch & Engrg  
ATTN: Strategic & Space Sys (OS)

## DEPARTMENT OF THE ARMY

BMD Advanced Technology Center  
ATTN: ATC-T, M. Capps  
ATTN: ATC-O, W. Davies

Harry Diamond Laboratories  
ATTN: DELHD-NW-P (20240)  
ATTN: DELHD-TA-L (81100)

U.S. Army Ballistic Research Labs  
ATTN: DRDAR-BLB, M. Kregel  
ATTN: DRDAR-TSB-S  
ATTN: DRDAR-BLT, J. Vanderhoff  
ATTN: DRDAR-BLP, J. Heimerl

U.S. Army Foreign Science & Tech Ctr  
ATTN: DRXST-SD-3

U.S. Army Nuclear & Chemical Agency  
ATTN: Library

U.S. Army Research Office  
ATTN: R. Mace

U.S. Army TRADOC Sys Analysis Actvy  
ATTN: ATAA-PL

U.S. Army White Sands Missile Range  
ATTN: STEWS-TE-AN, R. Hays  
ATTN: STEWS-TE-AN, J. Meason  
ATTN: STEWS-TE-AN, A. De La Paz

USAMICOM  
ATTN: Redstone Scientific Info Ctr

## DEPARTMENT OF THE NAVY

Naval Electronic Systems Command  
ATTN: PME 117-20  
ATTN: Code 501A  
ATTN: Elex 03

## DEPARTMENT OF THE NAVY (Continued)

Naval Intelligence Support Ctr  
ATTN: Document Control

Naval Ocean Systems Center  
ATTN: Code 532, R. Pappert  
ATTN: Code 5321, I. Rothmuller  
ATTN: Code 4471  
ATTN: Code 5322, H. Hughes

Naval Postgraduate School  
ATTN: Code 1424, Library

Naval Research Laboratory  
ATTN: Code 7550, J. Davis  
ATTN: Code 2627  
ATTN: Code 6700, T. Coffey  
ATTN: Code 1434, E. Brancato  
ATTN: Code 6780, S. Ossakow  
ATTN: Code 4700.1, W. Ali  
ATTN: Code 6750, K. Hain  
ATTN: Code 7120, R. Kinzer  
ATTN: Code 4139, D. McNutt  
ATTN: Code 4780, D. Strobel  
ATTN: Code 4187  
ATTN: Code 7101, P. Mange  
ATTN: Code 7175H, D. Horan  
ATTN: Code 6780, J. Fedder  
ATTN: Code 2000, J. Brown  
ATTN: Code 4128.2, J. Johnson

Naval Surface Weapons Center  
ATTN: Code F31  
ATTN: Code F46, D. Hudson  
ATTN: L. Rudlin  
ATTN: Code R41, D. Land

Nuclear Weapons Tng Group Pacific  
ATTN: Nuclear Warfare Department

Office of Naval Research  
ATTN: Code 414, G. Joiner  
ATTN: Code 412, B. Junker

## DEPARTMENT OF THE AIR FORCE

Air Force Geophysics Laboratory  
ATTN: OPR, R. Murphy  
ATTN: PHG, F. Innes  
ATTN: LKB, J. Paulson  
ATTN: SULL  
ATTN: OPR  
ATTN: LKD, C. Philbrick  
ATTN: LKB, K. Champion  
ATTN: LKB, T. Keneshea  
ATTN: LKB, W. Swider, Jr  
ATTN: LKD, R. Narcisi  
ATTN: CA, A. Stair  
ATTN: LKO, R. Van Tassel  
ATTN: LKO, R. Huffman  
ATTN: OP, J. Garing  
ATTN: OPR, R. O'Neill  
ATTN: F. Delgreco  
ATTN: OPR, H. Gardiner  
ATTN: OPR, J. Kennealy  
ATTN: OPR, T. Connolly



DEPARTMENT OF THE AIR FORCE (Continued)

Air Force Technical Applications Ctr

ATTN: STINFO Office/TF

ATTN: TD

ATTN: TF, L. Seiler

Air Force Weapons Laboratory

ATTN: SUL

Foreign Technology Division

ATTN: WE

ATTN: NIIS Library

Rome Air Development Center

ATTN: OCS, V. Coyne

ATTN: OCSA, J. Simons

USAFETAC/CB

ATTN: CBTL STOP 825

OTHER GOVERNMENT AGENCIES

Central Intelligence Agency

ATTN: OSWR/NED

Department of Commerce

National Oceanic & Atmospheric Admin

Environmental Research Laboratories

ATTN: D. Albritton

ATTN: E. Ferguson

ATTN: W. Spjeldvik

ATTN: F. Fehsenfeld

Department of Transportation

Transportation Rsch System Center

ATTN: F. Marmo

NASA

ATTN: Code 625, J. Heppner

ATTN: Code 625, M. Sugiura

ATTN: Technical Library

ATTN: S. Bauer

ATTN: J. Vette

ATTN: A. Aikin

NASA

ATTN: W. Roberts

NASA

ATTN: E. Schmerling

ATTN: R. Schiffer

ATTN: N. Roman

NASA

ATTN: Code JM6, Technical Library

NASA

ATTN: G. Poppoff

ATTN: W. Starr

ATTN: N-245-3, R. Whitten

National Science Foundation

ATTN: Div of Atmos Sci

ATTN: R. Sinclair

OTHER

University of Minnesota

ATTN: J. Winkler

DEPARTMENT OF ENERGY CONTRACTORS

EG&G, Inc

Los Alamos Division

ATTN: D. Wright

ATTN: P. Lucero

ATTN: J. Colvin

Lawrence Livermore National Lab

ATTN: L-71, J. Chang

Los Alamos National Laboratory

ATTN: MS 560, W. Hughes

ATTN: MS 668, J. Malik

ATTN: MS 668, H. Hoerlin

ATTN: MS 212, W. Barfield

ATTN: MS 670, J. Hopkins

ATTN: MS 664, J. Zinn

Sandia National Lab

ATTN: Org 1250, W. Brown

ATTN: Org 4241, T. Wright

DEPARTMENT OF DEFENSE CONTRACTORS

Aero-Chem Research Labs, Inc

ATTN: A. Fontijn

Aerodyne Research, Inc

ATTN: Librarian, B. Duston

ATTN: M. Faist

ATTN: M. Camac

Aerospace Corp

ATTN: R. Cohen

ATTN: H. Mayer

ATTN: Library

ATTN: M. Whitson

AVCO Everett Research Labs, Inc

ATTN: C. Von Rosenberg, Jr

Berkeley Research Associates, Inc

ATTN: J. Workman

Boston College

ATTN: Dept of Chemistry, D. McFadden

ATTN: Chairman Dept of Physics

ATTN: Science Library, F. McElroy

California Institute of Technology

ATTN: S. Trajmar

ATTN: V. Anicich

Chem Data Research

ATTN: K. Schofield

Cornell University

ATTN: M. Kelly

University of Denver

ATTN: Security Officer for B. Van Zyl

ATTN: Sec Officer for D. Murcay

Epsilon Labs, Inc

ATTN: C. Accardo

ESL, Inc

ATTN: W. Bell

DEPARTMENT OF DEFENSE CONTRACTORS (Continued)

General Electric Co  
ATTN: P. Zavitsanos  
ATTN: Technical Information Center  
ATTN: M. Linevsky

General Electric Co  
ATTN: J. Schroeder

General Research Corp  
ATTN: J. Ise, Jr

General Research Corp  
ATTN: T. Zakrzewski

Horizons Technology, Inc  
ATTN: R. Kruger

HSS, Inc  
ATTN: M. Shuler  
ATTN: D. Hansen

Information Science, Inc  
ATTN: W. Dudziak

Institute for Defense Analyses  
ATTN: E. Bauer  
ATTN: H. Wolfhard

Ion Physics Corp  
ATTN: C. Hauer

Johns Hopkins University  
ATTN: J. Kaufman

Kaman Sciences Corp  
ATTN: W. Rich  
ATTN: D. Foxwell

Kaman Sciences Corp  
ATTN: T. Stephens

Kaman Tempo  
ATTN: DASIAC  
ATTN: B. Gambill  
ATTN: J. Thompson  
ATTN: W. Knapp

KMS Fusion, Inc  
ATTN: Library

Lockheed Missiles & Space Co, Inc  
ATTN: D. Divis

Lockheed Missiles & Space Co, Inc  
ATTN: R. Gunton  
ATTN: T. James  
ATTN: B. McCormac  
ATTN: M. Walt  
ATTN: J. Reagan  
ATTN: J. Evans  
ATTN: J. Kumer  
ATTN: R. Sears

University of Lowell  
ATTN: G. Best

University of Maryland  
ATTN: Chemistry Dept, J. Vanderslice

DEPARTMENT OF DEFENSE CONTRACTORS (Continued)

University of Massachusetts  
ATTN: H. Sakai

University of Minnesota  
ATTN: M. Hirsch

Mission Research Corp  
ATTN: D. Archer  
ATTN: R. Hendrick  
ATTN: M. Scheibe  
ATTN: R. Kilb  
ATTN: D. Sappenfield  
ATTN: M. Messier  
ATTN: W. White

National Academy of Sciences  
ATTN: J. Sievers  
ATTN: National Materials Advisory Board

Nichols Research Corp, Inc  
ATTN: N. Byrn

Pacific-Sierra Research Corp  
ATTN: H. Brode, Chairman SAGE  
ATTN: E. Field, Jr

Pennsylvania State University  
ATTN: L. Hale  
ATTN: J. Nisbet

Photometrics, Inc  
4 cy ATTN: I. Kofsky  
4 cy ATTN: D. Villanucci  
4 cy ATTN: M. Chamberlain  
4 cy ATTN: C. Trowbridge

Physical Science Lab  
ATTN: W. Berning

Physical Sciences, Inc  
ATTN: K. Wray  
ATTN: R. Taylor  
ATTN: G. Caledonia

University of the Commonwealth, Pittsburgh  
ATTN: M. Biondi  
ATTN: F. Kaufman  
ATTN: W. Fite

Quantum Systems, Inc  
ATTN: S. Ormonde

R & D Associates  
ATTN: F. Gilmore  
ATTN: B. Gabbard  
ATTN: R. Lelevier  
ATTN: R. Turco  
ATTN: P. Haas  
ATTN: H. Ory

R & D Associates  
ATTN: B. Yoon  
ATTN: J. Rosengren

Science Applications, Inc  
ATTN: D. Hamlin

Science Applications, Inc  
ATTN: N. Byrn

DEPARTMENT OF DEFENSE CONTRACTORS (Continued)

Radiation Research Associates, Inc  
ATTN: N. Schaeffer

Science Applications, Inc  
ATTN: R. Johnston

Sechrist, Professor Chalmers F.  
ATTN: S. Bowhill  
ATTN: C. Sechrist

Spectral Sciences, Inc  
ATTN: F. Bein

SRI International  
ATTN: R. Leadabrand  
ATTN: R. Hake, Jr.

SRI International  
ATTN: C. Hulbert

Sylvania Systems Group  
ATTN: J. Concordia

Strategic Systems Div  
ATTN: I. Kohlberg

Technology International Corp  
ATTN: W. Boquist

University of Texas System  
ATTN: J. Browne

TRW Electronics & Defense Sector  
ATTN: Technical Information Center  
ATTN: J. Frichtenicht

DEPARTMENT OF DEFENSE CONTRACTORS (Continued)

Utah State University  
ATTN: Sec Control Ofc for K. Baker,  
Dir Atmos & Space Sci  
ATTN: Sec Control Ofc for D. Burt  
ATTN: Sec Control Ofc for A. Steed

University of Virginia  
ATTN: R. Ritter  
ATTN: H. Kelly  
ATTN: R. McKnight

Visidyne, Inc  
ATTN: C. Humphrey  
ATTN: T. Degges  
ATTN: H. Smith  
ATTN: J. Carpenter  
ATTN: O. Manley

Wayne State University  
ATTN: P. Rol  
ATTN: R. Kummier

Westinghouse Electric Corp  
ATTN: P. Chantry

William Marsh Rice University  
ATTN: R. Stebbings

William Marsh Rice University  
ATTN: Industrial Sec Super, J. Chamberlain

ATE  
MED  
8